Variability of a Summer Block in Medium-Range and Subseasonal Ensemble Forecasts and Investigation of Surface Impacts and Relevant Dynamical Features

Zur Erlangung des akademischen Grades eines
DOKTORS DER NATURWISSENSCHAFTEN
von der Fakultät für Physik des
Karlsruher Instituts für Technologie (KIT)

genehmigte

DISSERTATION

von

M.Sc. Lisa-Ann Quandt
aus Villingen-Schwenningen

Tag der mündlichen Prüfung:	19. Mai 2017
Referent:	Prof. Dr. Sarah C. Jones
Korreferent:	Prof. Dr. Olivia Martius

“Experience is one thing you can’t get for nothing.”

Oscar Wilde

Abstract

In summer 2010, an enormous high pressure system evolved over the European-Russian sector. It blocked the zonal flow for two months and created favorable conditions for two disastrous high impact weather events. The Russian population was afflicted with anomalously high surface temperatures and forest fires which led to a massive air pollution. Pakistan was inundated by deluge of water from stratiform rainfall and heavy precipitation events. The mentioned responsible high pressure system belongs to a group of large-scale flow patterns which are known as atmospheric blockings. They are persistent, self-sustaining, and quasi-stationary. They decelerate the large-scale basic flow and split the jet stream into two branches. Their genesis and lysis, as well as their neighboring troughs upstream and downstream (being the block's flanks) are characterized by low predictability. Because of their relation to high impact weather, there is a special need in improving blocking predictability and the understanding of the relevant physical processes.

In previous studies, blocking was investigated in detail, including the case in summer 2010. There were studies about forecast variability, about dynamics, impacts, or from a climatological point of view. However, these aspects were mostly investigated separately. In addition, several questions are still unanswered, for example addressing a commonly accepted definition, blocking maintenance as well as the onset/decay of blockings, also in respect of whose predictability.
In this study, two forecast ranges are considered and are compared against each other to show characteristics and benefits from both approaches for blocking prediction. For the medium range (with lead times of 10 days), a set of scenarios for the synoptic evolution during the onset, mature stage, and decay of the block are extracted from THORPEX Interactive Grand Global Ensemble multi-model ensemble forecasts. These scenarios represent the key features of the forecast variability of the block and of the resulting surface impacts. Two heat indices and a fire index are computed to highlight the forecast variability in societal impacts. The study is a proof of concept, showing how information about surface impacts can be derived from available operational ensemble forecasts in an effective manner, and pointing to possible difficulties in this approach. Comparing the forecast for the heat wave's impact on large spatial domains, and on a near-grid point scale, identifies challenges forecasters may face when predicting the development of a heat wave. Moreover, with the help of a correlation method, the dynamical processes are identified which were responsible for the forecast variability of the block during all three stages of the life-cycle. For the subseasonal range (with lead times of 45 days), development scenarios from Subseasonal-to-Seasonal multi-model ensemble reforecasts are extracted and compared. Only the

onset and the decay phase of the block are considered for the investigation of blocking predictability in the subseasonal range.

Although the block's onset was highly predictable, the increase in temperature and the extension of the heat-affected area differed between the scenarios. During the mature stage of the block, the variability of its western flank had a considerable influence on the precipitation and surface heat distribution. Since the blocking remained after the analyzed decay in two of three scenarios, the predictability of the decay was low in this forecast. The heat wave ended independently from the block's decay, as the surface temperature and the impact indices decreased in all scenarios. In scenarios without the decay of the block, the block was shifted so that the surface temperature anomaly and the geopotential height anomaly were not in phase anymore. In scenarios with the decay of the block, the upper-level controlling anomaly was missing to sustain the heat wave. For all phases of the block, its forecast variability was related to the performance of diabatic forcing over the North Atlantic. There were also other relevant dynamical processes (like the interaction with transient eddies) whose importance differed for the three phases of the block's life-cycle.

For the subseasonal range, the onset of the block was predictable. However, it was difficult to predict the exact date and position. The variability of the forecasts, which contained the decay phase of the block, was not related to the block's decay itself, although there were remarkable differences in the representation of the shape and position of the blocking pattern. In all scenarios, the lysis of the block was forecast too early.

Kurzfassung

Im Sommer 2010 entwickelte sich über Europa und Russland ein gigantisches Hochdrucksystem. Es blockierte die zonale Strömung für zwei Monate und schuf günstige Bedingungen für zwei katastrophale Wettereignisse mit hohem Schadenspotential. Die russische Bevölkerung war von anormal hohen Oberflächentemperaturen und Waldbränden, welche zu einer massiven Luftverschmutzung führten, betroffen. Pakistan wurde von Wassermassen aus stratiformen Regenfällen und Starkniederschlägen überschwemmt. Das genannte verantwortliche Hochdrucksystem gehört zu der Gruppe der großskaligen Strömungsmuster, die als atmosphärische Blocks bekannt sind. Sie sind persistent, selbsterhaltend und quasi-stationär. Sie bremsen die großräumige Strömung aus und spalten den Strahlstrom in zwei Äste auf. Ihre Bildung und Auflösung sowie ihre benachbarten Tröge stromauf und -ab (welche die Flanken des Blocks sind) sind durch geringe Vorhersagbarkeit gekennzeichnet. Wegen ihrer Verbindung zu Wettereignissen mit hohem Schadenspotential gibt es einen besonderen Bedarf daran, die Vorhersagbarkeit von blockierenden Wetterlagen und das Verständnis der relevanten physikalischen Prozesse zu verbessern.

In vorangegangenen Studien wurden Blocks, wie auch der Fall im Sommer 2010, tiefgehend untersucht. Es gab Studien über Vorhersagevariabilität, über Dynamik, Einfluss oder aus einer klimatologischen Perspektive. Jedoch wurden diese Aspekte in den meisten Fällen getrennt voneinander untersucht. Außerdem gibt es viele unbeantwortete Fragen über eine allgemein gültige Definition, die Aufrechterhaltung und den Beginn/Zerfall von Blocks, auch in Zusammenhang mit deren Vorhersagbarkeit.
In dieser Studie werden zwei Vorhersagezeiträume betrachtet und verglichen, um zu zeigen, welche Vorteile beide Betrachtungen für die Vorhersage von Blocks bringen. Für die Mittelfrist (mit einer Vorhersagelänge von 10 Tagen) werden Szenarien von „THORPEX Interactive Grand Global Ensemble"-Multimodell-Ensemblevorhersagen extrahiert, welche die synoptische Entwicklung während der Entstehungsphase, des Reifestadiums und des Zerfalls des Blocks zeigen. Diese Szenarien repräsentieren die Hauptmerkmale der Vorhersagevariabilität des Blocks und der sich ergebenen Einflüsse auf die Oberfläche. Zwei Hitzeindizes und ein Feuerindex werden berechnet, um die Vorhersagevariabilität in Auswirkungen, die von gesellschaftlichem Interesse sind, hervorzuheben. Die Studie ist ein Machbarkeitsnachweis, in dem gezeigt wird, wie Informationen über bodennahe Wetterbedingungen von verfügbaren operationellen Ensemblevorhersagen effektiv gewonnen werden können. Dabei wird auch auf mögliche Schwierigkeiten bei diesem Vorgehen hingewiesen. Der Vergleich von Vorhersagen des Einflusses der Hitzewelle für große Gebiete und Gebiete nahe der Gitterpunktskala zeigt Herausforderun-

gen auf, mit denen Meteorologen bei der Vorhersagen von Hitzewellen konfrontiert werden. Des Weiteren werden in dieser Arbeit mit Hilfe einer Korrelationsmethode dynamische Prozesse identifiziert, die für die Vorhersagevariabilität des Blocks während der drei Entwicklungsphasen verantwortlich waren. Für den sub-saisonalen Vorhersagezeitraum (mit einer Vorhersagelänge von 45 Tagen) werden Entwicklungsszenarien von „Subseasonal-to-Seasonal"-Multimodell-Ensemblevorhersagen extrahiert und verglichen. Es werden nur die Entstehungsphase und Zerfallsphase des Blocks betrachtet.

Obwohl die Bildung des Block durch hohe Vorhersagbarkeit gekennzeichnet war, waren der Temperaturanstieg und die Ausdehnung des Gebiets, welches von der Hitze betroffen war, in den Szenarien unterschiedlich. Während des Reifestadiums des Blocks hatte die Variabilität seiner Westflanke einen beachtlichen Einfluss auf die Niederschlags- und Hitzeverteilung. Da der Block in zwei von drei Szenarien nach dem analysierten Zerfall bestehen blieb, war die Vorhersagbarkeit des Zerfalls in dieser Vorhersage gering. Die Hitzewelle endete unabhängig von dem Zerfall des Blocks, da die Oberflächentemperaturen und die Werte der Indizes, welche die Hitzewirkung beschreiben, in allen Szenarien zurückging. In Szenarien ohne den Zerfall des Blocks verlagerte sich der Block, sodass die Oberflächentemperaturenanomalie und die Anomalie in der geopotentiellen Höhe nicht mehr in Phase waren. In Szenarien mit Zerfall des Blocks fehlte die kontrollierende Höhenanomalie, um die Hitzewelle aufrechtzuerhalten. Die Vorhersagevariabilität hing für alle Phasen des Blocks von der Darstellung des diabatischen Antriebs über dem Nordatlantik ab. Es gab auch andere relevante dynamische Prozesse (wie die Wechselwirkung mit transienten Wirbeln), die für die drei Phasen des Blocks unterschiedlich wichtig waren.
Für den sub-saisonalen Vorhersagezeitraum war die Entstehung des Blocks vorhersagbar, jedoch mit Schwierigkeiten in der Vorhersage des exakten Datums und der exakten Position. Die Variabilität der Vorhersagen, welche den Zerfall des Blocks beinhalteten, war nicht auf den Zerfall des Block selbst zurückzuführen, auch wenn es beachtliche Unterschiede in der Darstellung der Form und Position des Blocks gab. In allen Szenarien wurden die Auflösung des Blocks zu früh vorhergesagt.

Contents

1. Introduction

The major heat wave in Europe in summer 2003 claimed 50.000 fatalities (Black et al., 2004; Fink et al., 2004). The flooding in Great Britain in winter 2013/2014 caused economic losses of US$1.5 billion, more than 100.000 houses and flats were without electricity (Slingo et al., 2014; Thorne, 2014). The cold spell in Europe in winter 2010/2011 caused economic losses of US$6.1 billion (Cattiaux et al., 2010). All these disasters due to high impact weather had one thing in common: They were caused by atmospheric blocking. Blocking is a large-scale flow pattern that decelerates mid-latitude eddies, as well as the background flow, and forces them to follow a more meridional direction (e.g. Rex, 1950; Arakawa, 1952; Sumner, 1954). Atmospheric blocking is persistent and self-sustaining (e.g. Egger, 1978; Liu, 1994). Moreover, blocking is associated with low predictability during its onset and decay. That is because the onset of a blocking anticyclone is associated with a transition from a zonal to a meridional flow pattern (vice versa for the decay), which is challenging for numerical weather prediction (Tibaldi and Molteni, 1990; Frederiksen et al., 2004). Predictability is also low along the troughs upstream and downstream of blocking ridges (e.g. Tibaldi and Molteni, 1990; Matsueda, 2009). These troughs (hereafter, referred to as flanks) have a special role as they are the transition zones from the quasi-stationary persistent core of the block to the environmental flow. Because of its linkage to high impact weather events, there is a special interest in the predictability of blocking, in the physical processes which are relevant for the blocking evolution and in those which limit forecast quality.

An impressive example of atmospheric blocking was the spatially extended high pressure system over Russia in summer 2010 that blocked the zonal flow from mid-June to mid-August (Trenberth and Fasullo, 2012). Favorable large-scale sea surface temperatures and local soil moisture conditions supported the formation of the block (Hong et al., 2011; Lau and Kim, 2012; Schneidereit et al., 2012; Trenberth and Fasullo, 2012). Two high impact weather events were associated with this blocking system: a heat wave in Russia and floods in Pakistan. In Russia, 55.000 people died from the consequences of the heat wave. It was the worst drought since 1972 and caused an economic loss of about US$15 billion (Barriopedro et al., 2011; Grumm, 2011). In Pakistan, 20 million people were affected by the flooding, with 3000 fatalities (Hong et al., 2011). The predictability of the flooding event in Pakistan and the associated forecast variability of the upper-level controlling trough (being the eastern flank of the block) are not part of this study as these are discussed in Webster et al. (2011). Matsueda (2011) investigated the predictability of this blocking. Overall, the blocking was associated with high predictability, but drops in predictability occurred in the period from the end of July to mid-August. During this period, the forecasts of the block's

western flank were described as critical, especially at the end of July. His studies further revealed that the reduced predictability of the blocking high's decay influenced the reliability of forecasts for temperature extremes at the surface. The 2010 Russian heat wave block has not yet been investigated in the extended range.

Up to now, predictability, surface impacts and dynamics of certain weather systems like blocking were mostly investigated separately. The present work combines these issues. The 2010 Russian heat wave block is investigated concerning forecast variability, impact on surface conditions and relevant dynamical processes in the medium and in the subseasonal range. For the medium range, we show how differences in the representation of the blocking ridge may impact forecasts of surface conditions, like 2 m temperature and humidity. We further examine the dynamical mechanisms and features which were linked to the block's forecast uncertainty. The following research questions are addressed. Does low predictability of the blocking transfer to a low predictability of the associated high impact weather? What are the main development scenarios of the block in the forecast? Can the scenarios be linked to specific impacts or a lack thereof? Which are the dynamical features and processes which were responsible for the forecast variability of the block? For the subseasonal range, a time frame for which forecasts have only become available recently, we investigate how the blocking system is represented in a new set of ensemble forecasts. Furthermore, we seek to identify a potential limit of predictability for blocking on these time scales. In addition, we want to find out if the same methods can be used for investigating forecast variability in the medium range and the subseasonal range.

For the medium range, we focus on the three major developmental stages of the block's life-cycle: the onset phase, the mature stage, and the decay phase. We cluster medium-range multi-model ensemble forecast members at the time of high variability (defined here as a large spread between the forecast members within the ensemble) of the block. We investigate the impact of this variability on the intensity of the heat wave and in the precipitation distribution over Europe, where heavy rain events were reported (e.g. in Austria on 2 August 2010). In addition, we investigate the relevant dynamical processes which were responsible for the forecast uncertainty with the help of a correlation analysis. For the subseasonal range, we confine ourselves to the onset and the decay phase of the block. This investigation should rather give a first impression of blocking predictability for lead times over 15 days. We cluster 45-day forecasts, but did not further study the impact and the dynamics of the block as we did for the medium range.

This thesis is structured as follows. In the second chapter, background information is given on predictability, ensemble forecasting, and medium-range and subseasonal forecasts. Then, atmospheric blocking is discussed, regarding its definition, identification, climatology, relevant dynamical mechanisms, its linkage to high impact weather and finally, its predictability. Afterwards, some information

about heat waves and especially the 2010 Russian heat wave is presented. The third chapter introduces the data and methods which were used for the investigations of the medium range and presents the results with respect to predictability, impact and dynamics of the block. The fourth chapter describes the investigations of the subseasonal range, considering the data, methods and results regarding forecast variability. A comparison and discussion of both approaches in presented in Chapter 5. The conclusions and an outlook are given in the last chapter.[1]

[1] Chapter 3 has been published in Quandt et al. (2017) (except section 3.3.5 as well as the subsections "Dynamical Processes Responsible for the Forecast Variability" in section 3.4).

2. Background

We investigated the forecast variability of the 2010 Russian heat wave block. Forecast variability is introduced in terms of predictability and ensemble forecasting. In addition, the different forecast ranges are described which were considered in this study. Then, different aspects of atmospheric blocking are discussed to show the relevance of blockings for weather and weather prediction. In a last section, we focus on heat waves, to bridge the gap between blocking and high impact weather.

2.1. Predictability

Much progress has been made since the first ideas on numerical weather prediction of Bjerknes in 1904 (e.g. Lynch, 2008). Nowadays, weather services and prediction centers over the whole globe use supercomputers to calculate weather forecasts which are based on different forecast models. There are a lot of reasons (e.g. parametrization), why perfect weather forecasts do not exist. The subject that deals with the ability to make weather predictions and to understand predictable as well as unpredictable processes is called predictability. In the following, we present the origin and a definition of predictability and discuss the medium and the subseasonal range, which are considered in this study. In the last subsection, some aspects of ensemble forecasting are presented, since we used ensembles for our investigations.

2.1.1. Definition and Origin

The atmosphere is a nonlinear, dynamical system, in which many spatial and temporal scales interact (see e.g. Leutbecher and Palmer, 2008). The atmosphere is a chaotic system. A famous metaphor for chaos theory is the butterfly effect (Lorenz, 1963; Palmer, 2000). This concept is often visualized by the statement "the stroke of the wing of a butterfly may cause a tornado at the other end of the world". In less flowery words this means that even slight disturbances in the atmospheric state can have an enormous impact on the atmospheric system itself. Regarding predictability, this means that the inability to capture the whole effect of these disturbances may lead to enormous errors after a finite forecast length (Kalnay, 2003). An error on small scales is transferred from one scale to the next larger scale, until the largest scale is reached (Lorenz, 1969, 1963; Palmer, 2000). These disturbances are associated with initial condition and model errors, as well as with instabilities of the flow itself (Lorenz, 1963; Kalnay, 2003).
Initial conditions differ from the true state of the atmosphere, as a consequence of insufficient observa-

tions of the physical variables that characterize the weather and errors in populating the observations into the model (Lorenz, 1965; Stensrud et al., 1999). Lorenz (1982) described the development of small errors in the initial conditions for a perfect model (meaning that initial condition errors are the only source of errors) with the following equation:

$$\frac{d\varepsilon}{dt} = a\varepsilon(1-\varepsilon) \quad [2.1]$$

where ε is the root mean square average forecast and a is the growth rate. Thus, small errors grow exponentially with a, until a finite amplitude is reached, at which the growth rate is lowered (Kalnay, 2003). The equation has the following solution:

$$\varepsilon(t) = \frac{\varepsilon_0 e^{at}}{1+\varepsilon_0(e^{at}-1)} \quad [2.2]$$

with ε_0 as initial disturbance. In addition to the initial error, there are also model errors due to inaccurate boundary conditions, poorly represented external surface forcing, numerical approximations, or parametrization of physical processes like convection (Warner, 2010). Errors can also be divided into systematic and stochastic errors (Hamill et al., 2000). The former are reproducible if the model is run many times over similar cases. This is also known as model bias. The latter are not reproducible, like the initial condition error. However, the initial error and the model error cannot really be regarded separately, since the model uncertainty is partly responsible for the initial condition uncertainty (Leutbecher and Palmer, 2008).

As a consequence of those errors and the chaotic nature of the atmosphere, weather has a limited predictability. The limit of predictability can be defined as the lead time, at which the observed state is as different to the forecast state as to the climatological state (DelSole, 2004; Warner, 2010). Thus, a system is unpredictable if the forecast distribution is equal to the climatological one. However, this is only true for lead times shorter than those of the climatological range. Another definition of the limit of predictability takes two forecasts into account, since it asks how long it takes until two forecasts with only slightly different initial conditions behave like randomly chosen atmospheric states (Warner, 2010). Lorenz postulated that there is a theoretical limit of predictability even for a perfect model without initial condition errors (Lorenz, 1963, 1965, 1969). Since the atmosphere is not a deterministic system, he concluded that the future state is not uniquely determined by the past and present state (Lorenz, 1965). He further mentioned that the finite predictability is linked to non-periodic oscillations, while periodic oscillations have an infinite predictable range (Lorenz, 1969). In a study of Lorenz from 1982, he concluded that the theoretical limit of predictability (referring to a perfect model and perfectly known initial conditions) is 14 days, while the practical limit is reduced to 10 days. A limit of predictability means that the forecast errors are so large that the ability for weather prediction is lost (Kalnay, 2003).

Predictability depends on the predicted variables, the model resolution and the scale (Hamill et al., 2000). For example, the geopotential is generally more predictable than cloud cover. And a higher resolution can increase predictability. Regarding the different scales, on the near grid scale, errors grow faster than on the synoptic scale (Lorenz, 1969; Murphy, 1988; Leutbecher and Palmer, 2008). Since the weather

Tab. 2.1.: Temporal and spatial scales of atmospheric motions (following Kraus, 2004). The macroscale is sometimes divided into the planetary and synoptic scale.

Scale	Temporal Scale	Spatial Scale	Example
Macroscale	days or longer	$>$ 2000 km	planetary waves
Mesoscale	minutes to days	2-2000 km	thunderstorms
Microscale	seconds to minutes	$<$ 2 km	tornadoes

systems of different scales can be assigned to different wavenumbers, it is fair to say that predictability is a function of wavenumber.

To increase predictability and hence decreasing forecast uncertainty, the atmospheric model must be improved (Zhu, 2005). For example, the correct representation of solar forcing and the corresponding correct transition to sensible heat can increase predictability (Warner, 2010).

2.1.2. Medium Range to Subseasonal Range

In weather prediction, forecasts of different ranges exist, since weather phenomena appear on different temporal and spatial scales (Table 2.1, Kraus, 2004). The shortest range is called nowcasting (from minutes to several hours). This is followed by the short range, in which the weather of the next 3 days is predicted, the medium range (from 3 to 10 days), the extended range (from 10 to 30 days), and the long range (from 30 days up to two years). In the following, more details are provided about the medium range and the subseasonal range (also known as extended range).

A 10-day range considers the development of individual baroclinic disturbances and their associated weather (Palmer, 2000). Thus, the medium-range forecasts deal with weather phenomena like fronts, clouds or precipitation. Due to improvements in data assimilation, the model and the observing systems, the medium-range forecast skill has significantly increased in the last decades (Simmons and Hollingsworth, 2002; Rodwell and Doblas-Reyes, 2006). For example in the year 2000, a 7-day forecast was as good as a 5-day forecast in 1980 (Simmons and Hollingsworth, 2002).

The subseasonal to seasonal range has been described as a “desert of predictability“ (Vitart et al., 2016). It ranges between the medium range and the climatological range. The subseasonal range contains quite difficult lead times, since the memory of the initial conditions is already lost and the impact of the ocean is not strongly pronounced. In the seasonal range, the interaction between the ocean and the atmosphere plays an important role, since they are close to a coupled equilibrium (Palmer, 2000). The subseasonal range captures systems or oscillations whose duration is longer than the medium range. Examples are heat waves, atmospheric blocking events or a persistent zonal flow pattern (Vitart et al., 2014). With increasing lead time, the forecast skill decreases. However, Vitart et al. (2014) showed that for monthly

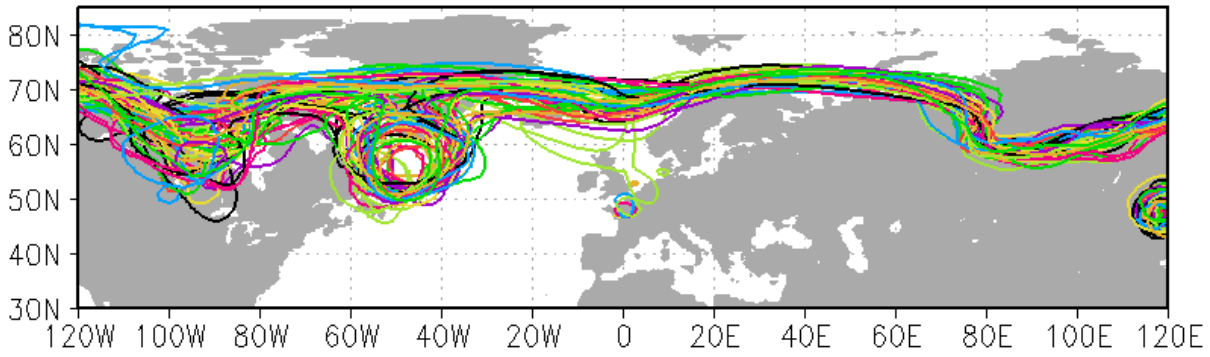

Fig. 2.1.: Example of an ensemble forecast of 500 hPa geopotential height isolines (5600 gpm). Each color is an individual member of the ensemble forecast. The spread between the isolines indicates forecast variability.

real-time ensemble forecasts of the 2 m temperature, even after 30 days, the skill is low, but still higher than climatology. Thus, systems in a 30-day range are not unpredictable. One reason for this level of predictability are important improvements in some parametrization schemes (e.g. for radiation or convection) between 2006 and 2008 (Vitart et al., 2014). Other examples of potential sources for predictability are the Madden-Julian Oscillation (MJO), the El Niño-Southern Oscillation (ENSO), soil moisture, snow cover, sea ice, teleconnections as well as interactions between the troposphere and the stratosphere.

2.1.3. Ensemble Forecasting

As discussed in section 2.1.1, there is a limit of predictability due to model errors and initial condition errors. The latter type of errors forms the basis for ensemble forecasting, in which variable initial conditions (being basically the probability density function of the initial state) are considered. In addition to the initial errors, ensemble forecasting addresses also the stochastic model errors. An ensemble forecast contains not only one forecast, but a number of individual forecasts (Figure 2.1). The idea is to encompass the true state of the atmosphere, since the set of initial conditions can be seen as an estimate for the probability density function of the true initial state (Stensrud et al., 1999). In Europe and the United States, ensemble forecasts have been used operationally since 1992 (Hamill et al., 2000).
There are three main goals of ensemble forecasting. The first one is the improvement of the forecast by ensemble averaging. The idea is that in the ensemble mean (being an unweighted mean of all ensemble members) only the predictable flow components remain, since the unpredictable parts are smoothed out (Kalnay, 2003; Leutbecher and Palmer, 2008). However, important features, like those which are connected to high impact weather, could vanish due to averaging. The second goal is to estimate the probability of future weather events (Stensrud et al., 1999; Kalnay, 2003). The third goal is to have an indicator for the reliability of a forecast. The forecast uncertainty can be estimated by the ensemble

spread (Murphy, 1988; Stensrud et al., 1999; Kalnay, 2003; Zhu, 2005).
The common ways to generate ensemble forecasts are listed below (Palmer, 2000; Kalnay, 2003; Leutbecher and Palmer, 2008; Warner, 2010):

1. The initial conditions are perturbed and added to the control forecast (being the best estimate of the true initial state of the atmosphere). This perturbation is done randomly or depending on the dynamics of the underlying flow.

2. Deterministic forecasts from different models are combined to one multi-model ensemble.

3. A model is run multiple times with different parametrization schemes.

4. The representation of physical processes in a model are perturbed in a stochastic manner (to simulate model errors).

Two examples of the first method (with perturbations depending on the dynamical background flow) are *bred vectors* and *singular vectors* (Kalnay, 2003; Magnusson et al., 2008; Warner, 2010; Diaconescu and Laprise, 2012). The former method, which is also known as *breeding*, is used by NCEP. The initial perturbations are set randomly and then, the perturbed as well as the control initial conditions are integrated. The difference between the control forecast and the perturbed forecast is calculated at fixed time intervals. The difference has to be scaled down to have the same amplitude as the the initial perturbation. Thereafter, the difference is added to the new model state. Singular vectors are an orthogonal set of perturbations with the largest linear growth for a given time period and relative to a specified metric. To create an ensemble, linear combinations of them are added to the control analysis. The ECMWF used a combination of singular vectors and the ensemble transform Kalman filter. The latter is also used by UKMO, which additionally uses the so-called stochastic kinetic energy backscatter scheme (Bowler and Mylne, 2009).
Two key questions arise when using the output of ensemble forecasts: How can ensemble forecasts be interpreted? What is a good or bad ensemble forecast? In a first approximation, a small ensemble spread indicates higher predictability and a large spread lower predictability, since a large spread is associated with an ensemble mean which does not show a realistic scenario. Actually, there are more things to consider, to score the quality of an ensemble forecast. This is illustrated in figure 2.2, from Kalnay (2003). The spread of the ensemble has to be large enough to capture the true state of the atmosphere and to capture the ”natural“ variability of the chaotic atmosphere. If the spread between the ensemble members is small, but the true atmospheric state lies outside the ensemble forecast, then it is a bad ensemble forecast. Thus, there are three demands on ensemble forecasts. The ensemble spread should be small if the predictability is high, but large enough so that the true state of the atmosphere lies within the ensemble and large enough that the actual predictability of the situation is reflected.
The skill of ensemble forecasts can be validated quantitatively with different methods (Hamill et al., 2000). The Brier skill score is one of several probabilistic skill measures. Other methods for ensemble

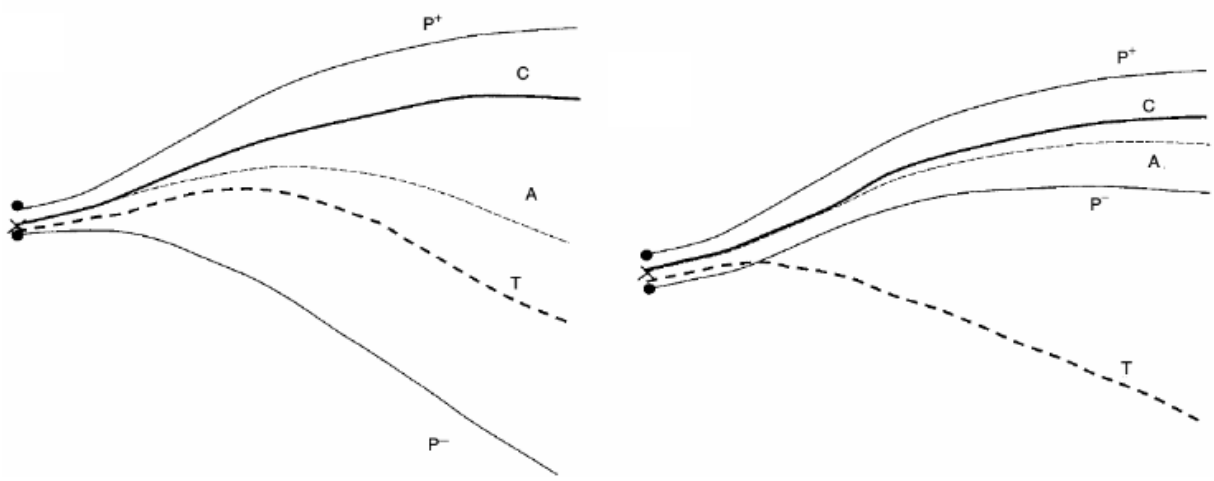

Fig. 2.2.: (left) Schematic of the components of a typical ensemble: (1) the control forecast (labeled C) which starts from the analysis (denoted by a cross), which is the best estimate of the true initial state of the atmosphere; (2) two perturbed ensemble forecasts (labeled P+ and P-) with initial perturbations added and subtracted from the control; (3) the ensemble average denoted A; and (4) the "true" evolution of the atmosphere labeled T. This is a "good" ensemble since the "truth" appears as a plausible member of the ensemble. Note that because of nonlinear saturation, the error of the ensemble member initially further away from the truth (in this case P+) tends to grow more slowly than the error of the member initially closer to the truth. This results in a nonlinear filtering of the errors: the average of the ensemble members tends to be closer to the truth than the control forecast. (right) Schematic of a "bad" ensemble in which the forecast errors are dominated by system errors (such as model deficiencies). In this case, the ensemble is not useful for forecasting, but it helps to identify the fact that forecast errors are probably due to the presence of systematic errors, rather than to the chaotic growth of errors in the initial conditions. Figure and caption are taken from Kalnay (2003). ©Eugenia Kalnay 2003, published by Cambridge University Press.

validation are reliability diagrams, rank histograms or the Relative Operating Characteristic (known as ROC).

The costs for running ensemble forecasts are high. To reduce these costs, ensemble forecasts are generally conducted with a lower resolution than the deterministic forecast. For global EPS, the spatial resolution varies from 18 to 70 km. However, the optimal usage of computer resources remains a problem, since the ensemble size should be large enough to provide reliable probability forecasts for extreme but rare events, and since the model should be sufficiently complex to simulate high impact weather events (Palmer, 2000).

2.2. Atmospheric Blocking

Atmospheric blocks are large-scale persistent systems, which lead to a transition from a zonal to a meridional flow pattern, and are challenging for weather prediction. Since blocking may create favorable conditions for high impact weather events, improvements in understanding the dynamical processes and improvements in blocking prediction are desired. In the following, details about blocking are given. In the first subsection, we give a definition for blocks and describe their characteristics. Then, some identification methods are presented. In the third subsection, diverse climatologies of blockings are shown. This is followed by a detailed discussions of the relevant dynamics. Then, the predictability of blocks is discussed. In the last subsection, we present the link to high impact weather.

2.2.1. Definition and Characteristics

There is no commonly accepted definition of atmospheric blocking. Several theories and approaches exist on how to define such a system. It was firstly described in 1950 by Rex as a jet splitting high pressure system. Some criteria were determined for the definition of a block (Rex, 1950; Arakawa, 1952):

1. The jet stream has to be split.
2. Both jet branches have to transport considerable amounts of mass.
3. The double-jet system has to be wider than 45° of longitude.
4. The system has to be persistent.

Due to the jet splitting, the flow turns from zonal to meridional (Arakawa, 1952; White and Clark, 1975), and incoming eddies have to follow this new path. Alongside this more synoptic description of a block, there are also definitions which belong to wave theory. Charney and DeVore (1979) described blockings as waves with large amplitude and near linear resonance, which interact with topography and asymmetric thermal forcing. Another wave theory arises from Egger (1978). There, blocking is described as the result of the nonlinear interaction of a forced wave and a free slowly propagating wave. In a potential vorticity (PV) perspective, blocking is a negative anomaly (Hoskins and Sardeshmukh, 1987; Crum and Stevens, 1988), whereas the higher tropopause over the block results from warm air advection from the south (for more details, see section 2.2.4). There are several other theories (for example the modon theory, in which blocks are described as isolated local disturbances (McWilliams, 1980)), which are not considered in this work.

Blocking systems can be characterized as follows. Their intensity and their spatial extension are correlated (Croci-Maspoli et al., 2007a). With wave lengths between 6000 and 7000 km (White and Clark, 1975), the spatial extension of a block varies form 0.4 to 1.3 x 10^6 km^2. The duration of a blocking

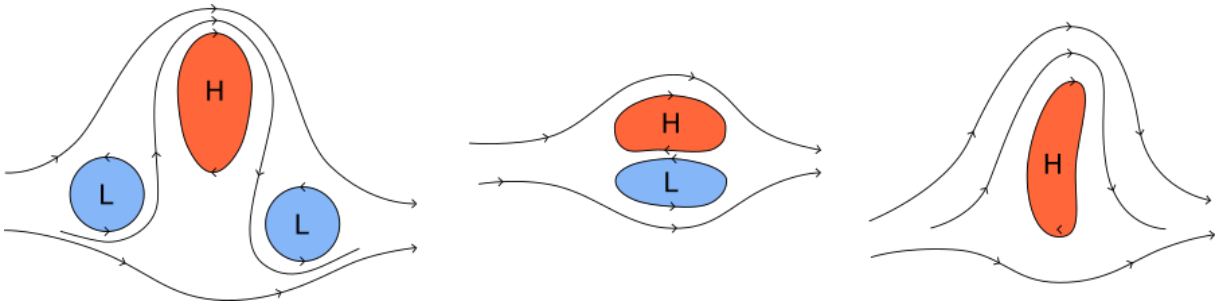

Fig. 2.3.: Scheme of the three common blocking types. From left to right: Omega block, high over low, amplified ridge.

system varies from days to months. The length of time how long a block has to exist to be referred to as block is, however, not consistent in the literature. In some studies, stationary high pressure anomalies are called blocks already after 5 days (e.g. Arakawa, 1952), whereas in other studies, the temporal limit is set to 10 days (e.g. Egger, 1978). Although, blocks are quasi-stationary, they do move. On average, a block moves northeastward, then westward and finally, northwestward. In individual cases, the block's movement depends on its genesis region and the season (Croci-Maspoli et al., 2007a).

Blocks appear in different configurations; there are three common types (Fig. 2.3). The first type is called an *omega block*, whereby a large high pressure system is flanked by low pressure systems upstream and downstream. The second common type is characterized by an anticyclone which is located to the north of a cyclone. This dipole was first described by Rex (1950), therefore it is also known as a *Rex block*. Another name for this configuration is *high over low pattern*. The third blocking type is a strongly amplified ridge. This configuration does not have a specific name.

The life-cycle of a blocking system can be divided into three phases (Croci-Maspoli et al., 2007a): the onset phase, the mature stage and the decay phase. During the onset phase, the block grows and intensifies rapidly. After a few days, its intensity decreases a little and remains at this level. During the mature stage, the block reaches its peak intensity. Fluctuations in intensity without changes in spatial extension are possible. The decay of a block is a short-lived process, in which the block's intensity decreases. Shortly living blocks (under 10 days) do not have an extended mature stage (Croci-Maspoli et al., 2007a). They decay directly after reaching their peak intensity.

2.2.2. Identification

There is no uniquely accepted blocking identification method, rather, several different blocking indices exist. Some indices detect the anticyclonic flow anomaly, while others search for the reversal of the mean flow (Table 2.2, Barnes et al., 2012). There are also blocking indices, which combine both aspects.

In 1990, Tibaldi and Molteni presented a 1D blocking index, which detects overturning structures in the

Tab. 2.2.: Overview over common blocking indices.

Source	Dimension	Variable	Identification of
Tibaldi and Molteni (1990)	1D or 2D	500 hPa geopotential height	overturning
Scaife et al. (2010)	2D	500 hPa zonal wind	overturning
Pelly and Hoskins (2003b)	1D or 2D	2 PVU potential temperature	overturning
Schwierz et al. (2004)	3D	vertically integrated PV	anomaly

500 hPa geopotential height (see also section 3.3.3). This index was an upgrade of an index which was developed by Lejenäs and Økland (1983). An advantage of the index of Tibaldi and Molteni (1990) is that a widely available variable is used to investigate atmospheric blocking. In the following years, different versions of this index were developed. For example, Masato et al. (2013) used a 2D version, which allows the meridional extension of the block to be investigated. Another modification of the index of Tibaldi and Molteni (1990) is that of Scaife et al. (2010). They used the zonal wind at 500 hPa, instead of the geopotential height.

The blocking index of Pelly and Hoskins (2003b) uses the potential temperature at 2 PVU (standing for 2 PV units) as a field on which blocking should be identified (see also section 3.3.3). As in the method of Tibaldi and Molteni (1990), the overturning of contours (here potential temperature at 2 PVU) is used as indicator for blocking. The index is 1D, as it is calculated along the so-called central blocking latitude (CBL). The CBL describes the latitude at which the 300 hPa transient kinetic energy is maximum. In a 2D version, the index can be also used as RWB detection (Woollings et al., 2008).

In the approach of Schwierz et al. (2004), blocking is identified as a persistent negative PV anomaly or feature of low PV. To calculate the PV anomaly, a climatological mean of the vertically integrated (from 500 hPa to 150 hPa) PV is subtracted from the vertically integrated instantaneous PV. Additionally, a tracking algorithm is used to identify the temporal coherence of a PV anomaly. The advantages of this index are that it considers the 3D state of the atmosphere and that it provides additional information on the blocking system (e.g. its amplitude).

The idea of Barnes et al. (2012) was to use the common blocking indices (among others, the index of Tibaldi and Molteni (1990)) and to determine additional criteria. They define an instantaneously blocked latitude and look if it is by the side of other instantaneously blocked latitudes. If that is the case, one large block is defined. The algorithm also considers the movement of the block. Thus it proves for a certain longitude if the existing block has moved or if a new system has evolved. Barnes et al. (2012) found that with these additional criteria, blocking climatologies with similar characteristics can be produced with the different blocking indices.

2.2.3. Climatology

The existing blocking climatologies show differences. These differences have various explanations. One aspect is the lack of consensus on which blocking index should be used. A second is whether additional criteria (for example for the duration of the block) are considered. Moreover, there are climatologies which refer only to a specific region or season and others that include the whole northern hemisphere for all seasons.

The climatology of Croci-Maspoli et al. (2007a) for the northern hemisphere is based on ERA-40 reanalysis data from 1957 to 2002. With the help of the blocking index of Schwierz et al. (2004), they found two peak blocking frequencies over the North Atlantic and over the North Pacific, in agreement with other studies. However, in contrast to other studies, they found a third maximum over Asia. Blockings evolve preferentially over the ocean basins as well as between 40°N and 50°N, but there is no conspicuous place where blocks decay, however, they tend to decay at high latitudes (Croci-Maspoli et al., 2007a). Further findings of Croci-Maspoli et al. (2007a) are that blocks are stronger in winter than in summer and that summer blocks are less frequent, in comparison to blocks which occur in the other seasons.

As described in section 2.2.2, Barnes et al. (2012) presented a methodology for the comparison of blocking climatologies. They applied their method for a period from 1958 to 2000 and used ERA-40 reanalysis data. They found that Atlantic blocks evolve over the whole year with a peak blocking frequency between mid winter and summer. Another result was that there are fewer blocks over the Pacific compared to the Atlantic ocean. However, when only considering the summer season, more blocking events are observed over the Pacific basin. In autumn, the lowest blocking frequency is found. They also found that peak blocking frequencies are located at 135°W, as well as over the European-Atlantic sector.

Tyrlis and Hoskins (2015) also used the ERA-40 dataset, but identified blocks with the index of Pelly and Hoskins (2003b). They mentioned two regions where blocks are most prevalent. The first one spans from the eastern Atlantic to central Asia, also including Europe. The second region is in the central eastern North Pacific. The peak in frequency is in Scandinavia with 24 % of blocked days. In comparison, in the North Pacific, only 7 % of the days are blocked.

D'Andrea et al. (1998) made simulations of northern hemisphere blocking using 15 different general circulation models. They identified blocking with the index of Tibaldi and Molteni (1990). For the period from 1979 to 1988, they investigated and compared the Euro-Atlantic and the Pacific blocking sector. Euro-Atlantic blocks as well as Pacific blocks occur most frequently in spring, whereas Pacific blocks have another peak in the wintertime. Although they attained similar results compared to studies based on reanalysis data, they also found that all 15 atmospheric general circulation models underestimate the blocking frequency.

In times of global warming and Arctic amplification, the question arises if there is also a climatological trend for atmospheric blocks. Will the zonal flow be more or less blocked in the future? Croci-Maspoli et al. (2007a) did not find a common trend for blocking frequency for the whole northern hemisphere.

Other studies refer only to a smaller area. Buehler et al. (2011) used the blocking index of Tibaldi and Molteni (1990) for their investigations and found that there is a statistically significant decrease in the number of North Atlantic winter blocks over the ERA-40 period (from 1975 to 2000). Mori et al. (2014) investigated the frequency of Eurasian blocks in reanalysis, as well as with the help of simulations. They found that blocking over Eurasia will be more frequent in the future due to sea-ice decline. They concluded that this will favor advection of cold air to Eurasia and hence severe winters.
To sum it up, on the annual average, blocking occurs most frequently over the North Atlantic and over the North Pacific. Other studies also showed a peak blocking frequency in Scandinavia. These differences between the climatologies are attributed to the use of different blocking indices. Regarding the seasons, blocks are less frequent in summer. Moreover, recent studies could identify a common future blocking trend for specific regions, but not for the whole northern hemisphere.

2.2.4. Dynamics

In this subsection, the dynamics which are relevant for atmospheric blockings are presented. First, we introduce PV thinking as basis for following considerations. Then, Rossby wave breaking is shown to be a key process for blocking. Rossby wave breaking is linked to different life-cycles of surface weather systems, whose impact on blocks is discussed in the transient eddy feedback section. Additionally, blocking is also influenced by diabatic forcing, which is discussed thereafter. At the end, the impacts of orography and precursor blocks are shown to present a complete picture of blocking dynamics. With the exception of orography, all dynamical processes presented in the following are considered in our investigations of the 2010 Russian heat wave block in the medium-range forecasts.

PV Thinking

Along with quasi-geostrophic theory and energetics, PV thinking represents another view to describe and understand atmospheric dynamics. The isentropic potential vorticity was introduced by Ertel (1942). It is defined as follows:

$$PV = \frac{1}{\rho}\vec{\eta} \cdot \nabla\theta \qquad [2.3]$$

where ρ is the density, $\vec{\eta}$ is the absolute vorticity and θ the potential temperature. PV thinking has the following advantages (Hoskins et al., 1985):

1. Without diabatic forcing or friction, the PV of an air parcel is conserved.

2. The PV combines the wind and the mass field. Thus, it is a dynamical as well as a thermodynamical quantity.

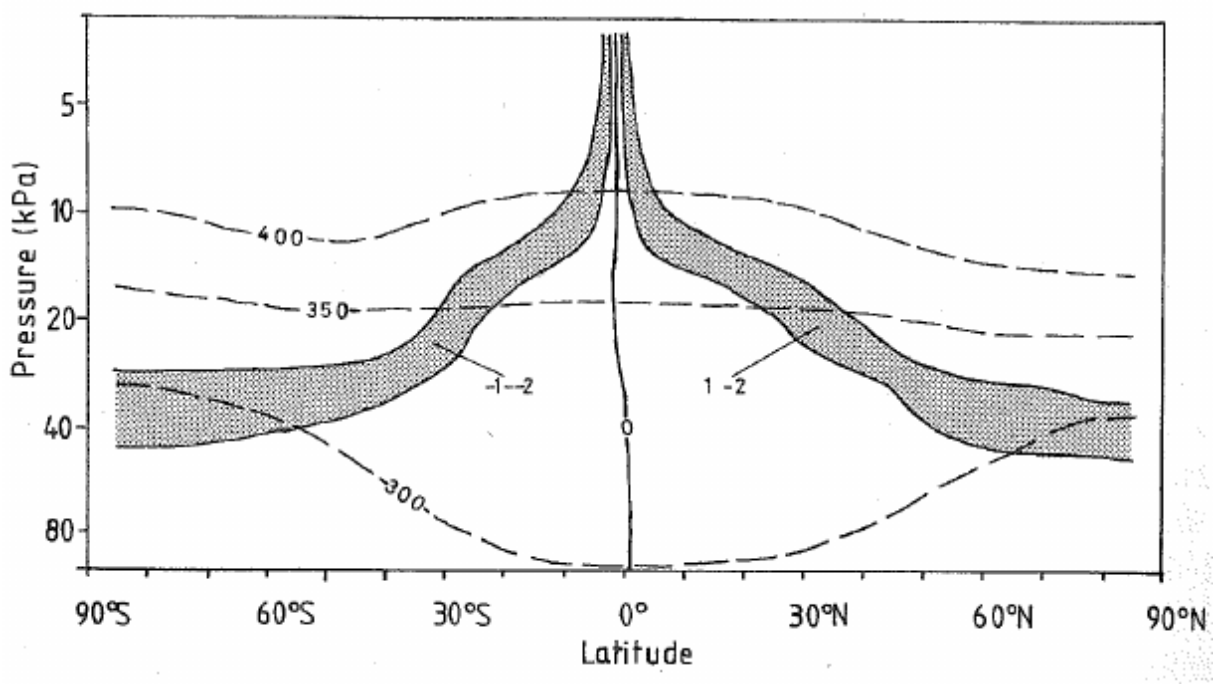

Fig. 2.4.: Schematic cross section of potential temperature (dashed lines) and Ertel potential vorticity (solid lines). The shading indicates regions where $1 < |\mathrm{PV}| < 2$ PVU, which roughly delineate the midlatitude tropopause. Figure and caption adopted form James (1995). ©Cambridge University Press 1994.

3. The PV distribution controls many large-scale dynamical processes (for example the propagation of Rossby waves).

4. The invertibility principle: The knowledge of the PV distribution, boundary conditions, a reference state, and an appropriate balance condition are sufficient to determine the wind and the mass field.

High values of PV are found in the stratosphere, because of high stability ($\nabla\theta$ is large). The tropospheric air typically has lower PV, since it is less stable ($\nabla\theta$ is small). On an isentropic surface, high PV air is found in the north, low PV air in the south, since the troposphere is higher at the equator (Figure 2.4). In the troposphere, high PV values occur within cyclonic eddies, while an anticyclonic system is characterized by high PV air. As already mentioned in section 2.1.1, blocking anticyclones are characterized by low PV. Hence, the onset and maintenance of a block is triggered by the advection of low PV air. A description of blocks in a PV perspective can be found in the study of Crum and Stevens (1988).

Rossby Wave Breaking

Rossby wave breaking is a key process for atmospheric blocking (Masato et al., 2012). Many other studies address the interaction between the North Atlantic Oscillation (NAO), jet displacement, Rossby wave breaking (RWB) and blocking (e.g. Riviere and Orlanski, 2007; Strong and Magnusdottir, 2008). The NAO and the RWB mechanism are introduced below. Additionally, the interaction between these flow

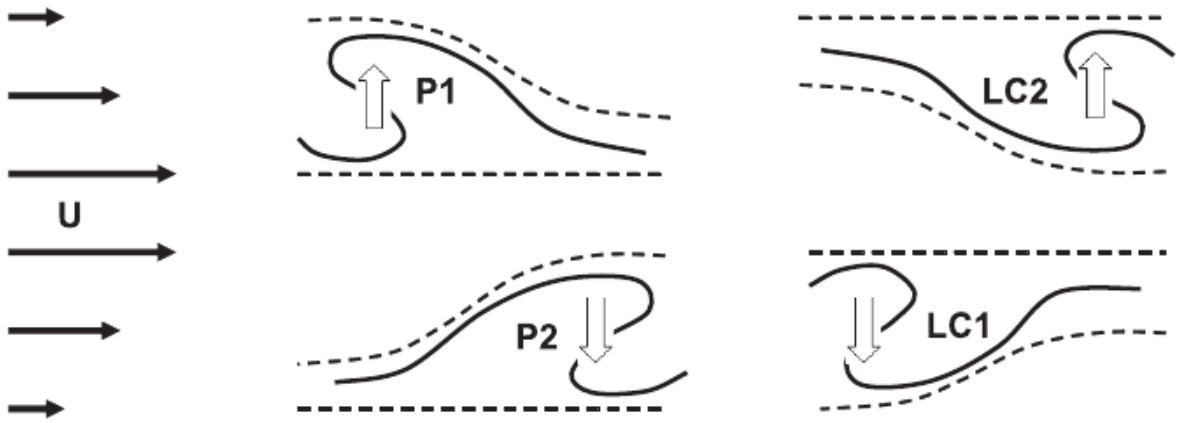

Fig. 2.5.: Idealized pictures of asymmetric RWB events in a horizontal plane indicated by potential vorticity (black lines): cyclonically sheared waves breaking predominantly in poleward (P1) or equatorward (LC2) direction, and anticyclonically sheared waves breaking predominantly in poleward (P2) or equatorward (LC1) direction; black arrows: westerly jet with horizontal shear; dashed lines: geopotential of a basic flow; and white arrows: meridional eddy fluxes down the gradient of the westerly jet. Figure and caption adopted form Gabriel and Peters (2008).

features is discussed.

If a Rossby wave breaks, this leads to the decay of the wave and hinders its further eastward propagation. RWB is characterized by an irreversible PV contour overturning (McIntyre and Palmer, 1983). Rossby waves can break in different directions (cyclonic or anticyclonic). The direction depends on the shear of the flow (Thorncroft et al., 1993; Gabriel and Peters, 2008; Weijenborg et al., 2012). Additionally, the breaking is partitioned depending on whether dominant breaking happens to a trough (equatorward RWB) or a ridge (poleward RWB). Four types of RWB have been defined (Figure 2.5, Thorncroft et al., 1993; Gabriel and Peters, 2008): LC1 (equatorward and anticyclonic), LC2 (equatorward and cyclonic), P1 (poleward and cyclonic), and P2 (poleward and anticyclonic). LC1 and P2 are favored by diffluent flow conditions, while LC2 and P1 preferentially occur in a confluent flow. In the following, we only differentiate between cyclonic (CWB) and anticyclonic wave breaking (AWB).

On subseasonal time scales, RWB is linked to the phase of the NAO. The NAO is defined as a subseasonal oscillation which describes the distribution of low and high pressure over the North Atlantic. The positive phase of the NAO is defined as a low over high pattern (Benedict et al., 2004). Thus, a cold low pressure system is located to the north of a warm high pressure system. Moreover, the jet is shifted to the north (Riviere and Orlanski, 2007). In the negative NAO phase, there is a high over low pattern, hence, an anticyclone is located north of a cyclone (Benedict et al., 2004). Here, the jet is displaced southward (Riviere and Orlanski, 2007). The phase of the NAO can be inverted by the appearance of cyclones at the US East Coast (Riviere and Orlanski, 2007). As the RWB direction is dependent on the shear and the NAO is connected to a meridional jet displacement, the RWB direction depends on the NAO phase. The positive NAO phase is correlated to AWB (shifting the jet northward) over the North Atlantic and the

negative phase to CWB (shifting the jet southward) (Benedict et al., 2004; Riviere and Orlanski, 2007; Croci-Maspoli et al., 2007b; Woollings et al., 2008). Additionally, Strong and Magnusdottir (2008) found that the connection between the NAO and the RWB direction depends on the latitude at which the RWB event occurs. The relation mentioned above is valid for 50°N, while it is the other way round for regions farther south (20°N) or north (70°N). Atmospheric blocking and the NAO are connected due to their linkage to RWB, but additionally, in two other ways. First, the negative NAO phase (high over low) can already be interpreted as blocking pattern. Second, if the NAO is in its negative phase, the blocking frequency is higher than during its positive phase (Benedict et al., 2004; Croci-Maspoli et al., 2007b; Woollings et al., 2008).

Transient Eddy Feedback

Transient eddies (TE) are fast-moving and short-lived synoptic-scale cyclones and anticyclones. They can be illustrated as the difference between the instantaneous value and a long-time mean of a certain flow variable (for example geopotential height; Chen and Juang, 1992). TE are continually produced within the storm track and influence the transport of momentum, moisture and heat (e.g. Luo et al., 2001). Their effect on the vorticity field can be seen in the approximate time-mean vorticity equation for the upper troposphere (Lau, 1979):

$$\overline{\vec{v}} \cdot \nabla \overline{\eta} - \overline{\eta} \nabla \cdot \overline{\vec{v}} - \nabla \cdot \overline{\vec{v}' \eta'} \approx 0 \qquad [2.4]$$

where $\vec{v}$ is the horizontal wind and η the vertical component of the absolute vorticity. The overbar indicates a time-mean, the prime the deviation from the mean. The first term is the advection term, which describes the spatial vorticity transport. The second term is the divergence term, showing the influence of upper level convergence and divergence of the wind on the vorticity field. The third one is the eddy term, presenting the divergence of the eddy vorticity flux. During a blocking event, the TE are forced to flow along the split jet and interact with the blocking system. In the following, this process is discussed in detail.

The study of Berggren et al. (1949) first introduced the transient eddy feedback on blocks. Figure 2.6 illustrates how a trough propagates toward a blocking ridge and is absorbed. Figure 2.6 a shows a flow configuration dominated by two ridges, with the western ridge being less amplified. Then in Figure 2.6 b, the eastern ridge is turning over, while the trough between the two ridges deepens. In Figure 2.6 c, a cut-off cyclone remained and the ridges merged. In Figure 2.6 d to f, the series of events is repeated. Again, a ridge propagates from the west into the block and the trough in between the ridges becomes a cut-off.

One of the most famous studies of the TE feedback on blocking activity was done by Shutts (1983), although there were even earlier studies (e.g. Berggren et al., 1949; Mahlman, 1979). Shutts conducted numerical experiments with barotropic models to investigate the feedback of eddies on blocks. He formulated the *eddy straining hypothesis*, which considers an energy transfer as well as the (potential) vorticity

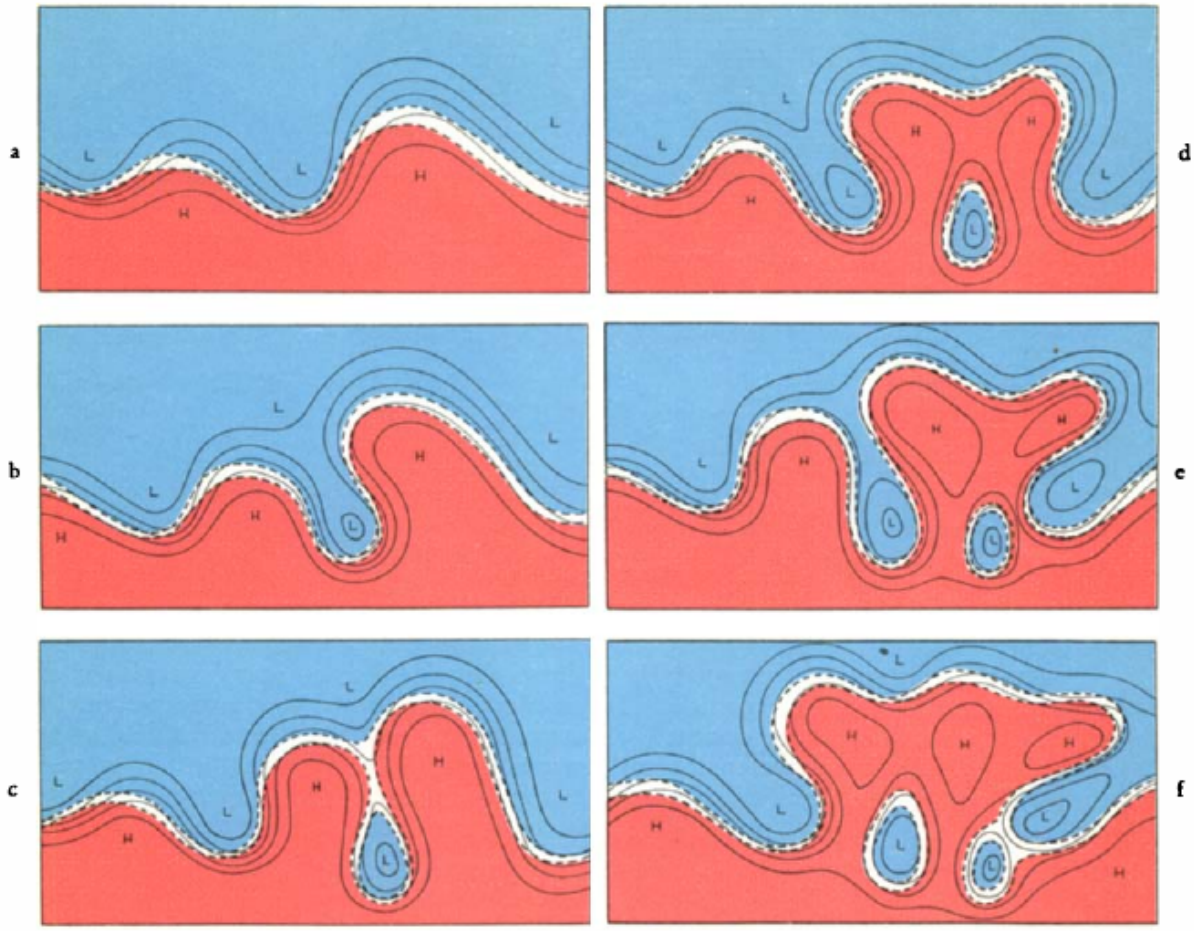

Fig. 2.6.: Idealized sketches of the development of unstable waves at the 500 mb level, in association with the establishment of a blocking anticyclone in high latitudes. Cold air in blue, warm air in red. Solid lines are stream lines and dashed lines the frontal boundaries. Figure and caption adopted form Berggren et al. (1949).

budget. The energy transfer is based on the idea that the split jet around a block represents a deformation field. In such a deformation field, the incoming small-scale eddies are split and compressed, leading to an energy transfer to the blocking flow (Figure 2.7). Furthermore, there is a transfer of momentum (corresponding to a net energy transfer) from the eddies to the block that is connected with a tilting of the TEs as they propagate along the jet branches (Kuo, 1953). Initially circular eddies in the northern branch have a north-west/south-east tilt, while in the southern jet branch, the eddies have a north-east/south-west tilt. The second part of the eddy straining theory deals with the PV budget. The blocking anticyclone is regarded as area of low PV air. The transfer of vorticity by TEs leads to an anticyclonic forcing to the north and a cyclonic forcing to the south of a region upstream of the blocking system, so that the mean vorticity budget is balanced.

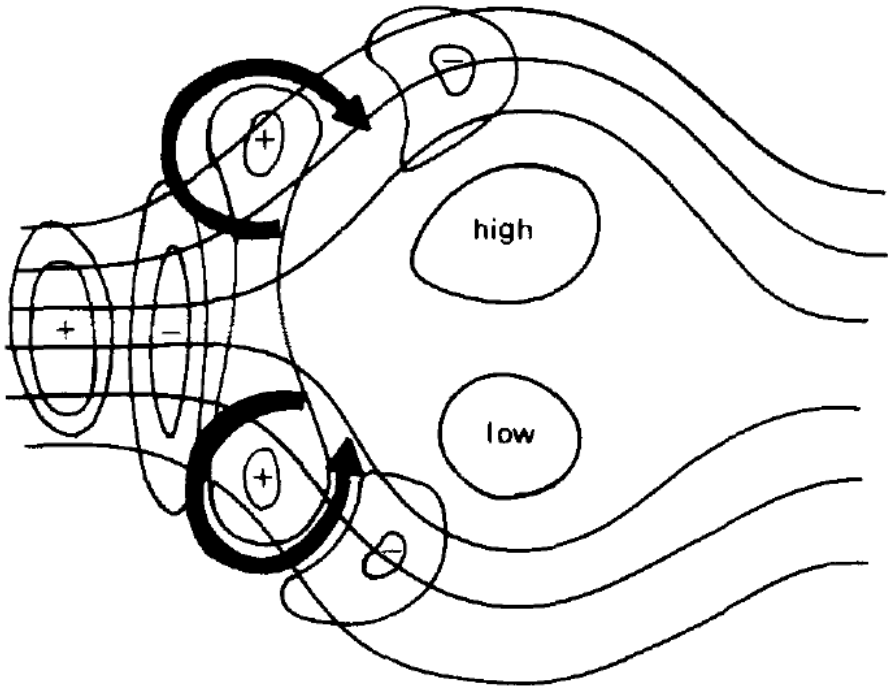

Fig. 2.7.: Schematic picture of the production and subsequent deformation of eddies propagating into a split jet stream together with their associated vorticity forcing pattern. The arrows symbolize the curvature vorticity. Figure and first sentence of the caption adopted from Shutts (1983). ©Quarterly Journal of Royal Meteorological Society. Adapted with permission from John Wiley & Sons, Inc.

The eddy forcing is clearly represented in the paper of Mullen (1987), where the transient eddy fluxes D are described by the following sum:

$$D = D^{heat} + D^{vort} \quad [2.5]$$

with:

$$D^{heat} = f\frac{\partial}{\partial p}\left(\frac{\nabla\cdot\overline{\vec{V}'\theta'}}{\tilde{S}}\right) \quad [2.6]$$

$$D^{vort} = -\nabla\cdot\overline{\vec{V}'\zeta'} \quad [2.7]$$

where p is the pressure, θ the potential temperature, $\tilde{S}$ the hemisphere mean of $-\frac{\partial\bar{\theta}}{\partial p}$ and ζ the relative vorticity. D^{heat} represents local changes of the divergence of the eddy potential temperature flux with pressure. D^{vort} is the divergence of the eddy vorticity flux.

The eddy straining mechanism is barotropic, while baroclinicity is necessary for the evolution of TE (Shutts, 1983; Mullen, 1987). Trenberth (1986) investigated the barotropic as well as the baroclinic TE activity with the help of the Eliassen-Palm flux. He found that both the barotropic and the baroclinic component are of importance for flow dynamics. The barotropic component decelerates the west drift. The baroclinic component, which dominates the subtropical jet branch, reduces the meridional temperature gradient (influencing the thermal wind).

A recent study of Yamazaki and Itoh (2013) presented a new perspective on the transient eddy feedback

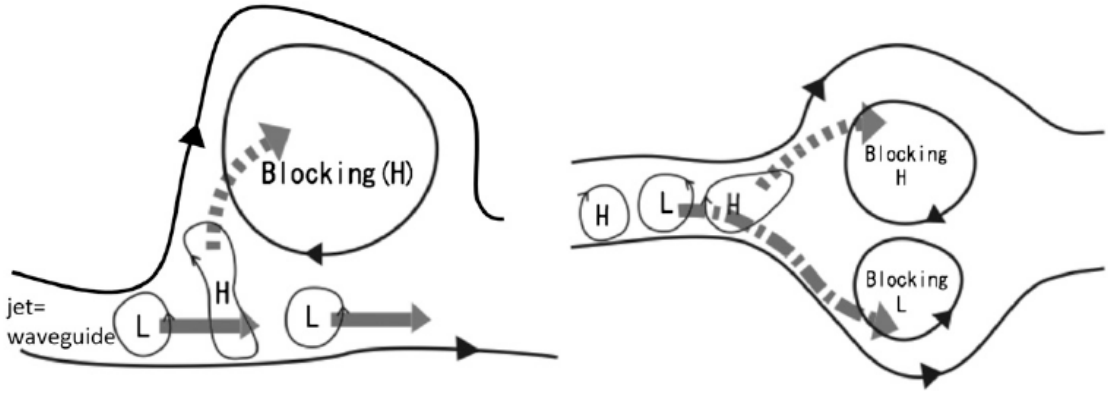

Fig. 2.8.: Conceptual diagrams illustrating the SAM. (left) For a V-type block, when synoptic eddies propagating along a waveguide approach a blocking anticyclone, synoptic anticyclones (H) are selectively absorbed by the blocking anticyclone, while synoptic cyclones (L) are repelled and drift downstream. (right) for a dipole-type block. Figure and caption adopted from Yamazaki and Itoh (2013). ©American Meteorological Society. Used with permission.

in a barotropic flow, named the selective absorption mechanism (SAM). The SAM can be described as follows (Figure 2.8). Anticyclonic TE of low PV air are absorbed by the block, since they have the same polarity. The upstream trough (corresponding to the block's western flank) is maintained by cyclonic eddies. They require vorticity conservation on the f plane. Hence, the vortex-vortex interactions can be described by the equation below:

$$\frac{\partial \zeta}{\partial t} = -J(\psi^B, \zeta^B) - J(\psi^{TE}, \zeta^{TE}) - J(\psi^B, \zeta^{TE}) - J(\psi^{TE}, \zeta^B) \qquad [2.8]$$

where ζ is the relative vorticity, ψ the stream function and J the Jacobian operator. B represents the blocking vortex and TE the vortex of the transient eddy. The first two terms on the right-hand side represent the self-advection effects and can be neglected (since they are zero for circular vortices). The vorticity advection of TE by winds of the block is represented in the third term. The forth term shows the advection of the vorticity of the block by the flow of the TE, which leads to a drift of the TE toward the block. The approach of Yamazaki and Itoh (2013) differs from the classical idea of the TE feedback mechanism, since the polarity, the vortex-vortex interaction and the absorption are crucial criteria for the SAM. However, there were already earlier studies, which considered aspects of the SAM theory. Nakamura and Wallace (1993) pointed out that the effect of anticyclonic TEs on blocks is higher than that of the cyclonic TEs, corresponding to the polarity of the TEs. Moreover, they and also many other studies (e.g. Berggren et al., 1949) mentioned the idea that the TEs are absorbed by the block.

Numerical studies of Chen and Juang (1992) showed that if the TEs, which potentially interact with the block, are included in the initial conditions, the predictability of the block can be increased. The TE feedback mechanism seems to be favorable for the block, however, not crucially required (e.g. Chen and

Juang, 1992).

Diabatic Processes

Both the adiabatic advection of PV as well as the diabatic PV modifications are important for blocking activity (Pfahl et al., 2015). To introduce diabatic processes, first, we have a look at the time-averaged thermodynamic energy equation (Hoskins and Sardeshmukh, 1987):

$$c_p \left[\overline{\vec{v}} \cdot \nabla \overline{T} + \left(\frac{p}{p_0} \right) \overline{\omega} \frac{\partial \overline{\theta}}{\partial p} + \nabla \cdot \overline{\vec{v}' T'} + \left(\frac{p}{p_0} \right)_k \frac{\partial}{\partial p} \overline{\omega' \theta'} \right] = \overline{H} \qquad [2.9]$$

where c_p is the specific heat capacity, $\vec{v}$ the horizontal wind vector, T the temperature, p the pressure (p_0 = 1000 hPa), $k = \frac{R}{c_p}$ (with R as gas constant), ω the vertical velocity, θ the potential temperature, and H the diabatic heating. The bar refers to a time-average, while the prime stands for the deviation from the time-average. The first and the second term on the left-hand side reflect the steady terms, while the others represent the transient terms. The first and the third term show the horizontal temperature advection, while the second and the fourth term show the vertical advection. Thus, the 3D temperature advection is equal to the mean diabatic heating. Sinking air parcels warm adiabatically, rising air parcels cool adiabatically. Independently of the vertical motion of the air parcel, cooling and warming can also occur due to diabatic processes. They arise from the influence of radiation and condensation. If we have a look at the equation for temporal changes in the PV field, we note that there are PV changes due to diabatic processes (Ertel, 1942):

$$\frac{dPV}{dt} = \frac{1}{\rho} \left(\vec{\eta} \cdot \nabla \dot{\theta} + \nabla \times \vec{F} \cdot \nabla \theta \right) \qquad [2.10]$$

where $\vec{\eta}$ is the absolute vorticity, $\dot{\theta}$ represents diabatic heating and $\vec{F}$ friction. Thus, a maximum of diabatic heating (due to latent heat release) leads to a positive PV anomaly below and a negative anomaly above the maximum. Such PV modifications are for example realized in Warm Conveyor Belts (WCB). WCBs origin from the warm sector of cyclones and are of particular importance for meridional energy transport (Eckhardt et al., 2004). They are defined as moisture trajectories with an ascent of 600 hPa within two days (Madonna et al., 2014). The requirements for WCBs are low-level moisture, baroclinicity, and upper-level forcing of ascent (Madonna et al., 2014). Along WCB trajectories, moisture decreases due to precipitation. The release of latent heat (due to condensation) leads to an increase of the potential temperature with height. Along the trajectories, PV first increases, than decreases, since due to diabatic heating, there is a PV production at lower levels and a destruction near the tropopause (Madonna et al., 2014; Pfahl et al., 2015). This leads to a positive impact of WCBs on ridge amplification at the upper troposphere and thus, on blocking activity (Madonna et al., 2014).

Surface Feedback

Kikuchi (1971) made numerical experiments in which he investigated the influence of mountains and the land-sea distribution on blocking activity. He compared four numerical runs (with/without land-sea distribution and with/without mountains). He found that blocks occur even without an effect of mountains or the land-sea distribution. However, the propagation and duration of the block seem to depend on orography and surface conditions. Furthermore, this dependence is relevant for different areas. Between 30°E and 150°E, as well as between 30°W and 150°W, thermal forcing due to the land-sea distribution as well as orography influence blocking activity. For the remaining longitudes, only the dynamical effect of mountains is of relevance.
Other studies, in which the dependence of atmospheric blocking on orography is investigated, showed similar results (e.g. Egger, 1978).

Precursor Blocks

Sometimes, there is a precursor block, meaning that a development of a block is preceded by another block. The first block decelerates the background flow and supports the development of a block further downstream. A weak background flow is favorable for the development of a block, as it allows the wave to become stationary (Luo et al., 2001). In the literature, no general requirements about the duration or intensity of precursor blocks are mentioned. A precursor block is - as mentioned - favorable, but not essential (Luo et al., 2001).

2.2.5. Link to High Impact Weather

Long-lasting atmospheric blocks may cause high impact weather events. High surface pressure within the block may favor the development of cold spells in winter (e.g. Hoskins and Sardeshmukh, 1987) and heat waves in summer (e.g. Green, 1977; Black et al., 2004). The high surface pressure can lead to clear sky conditions. In winter, this leads to surface cooling, due to an increase in out-going longwave radiation during the night (Sillmann et al., 2011). Moreover, for Europe, blockings support the northeasterly inflow of cold and dry air masses (Sillmann et al., 2011). One example is winter 2010, during which anomalously cold temperatures evolved in Northern Europe. This temperature anomaly was caused by an extreme persistence of the negative phase of the NAO (Cattiaux et al., 2010), which can be interpreted as high over low block. In summer, the increase in incoming shortwave radiation during daytime due to less cloudiness (caused by the blocking anticyclone) is of relevance, as it favors surface heating. Heat waves are discussed in detail in section 2.3.
In addition to heat waves and cold spells, blocking may also be linked to flooding. Two circumstances can lead to large amounts of precipitation. The first one is that a system is of high intensity, for example

convective systems (like thunderstorms) or winter storms. A block can influence the flow pattern in such a way that arriving stormy cyclones are led along a certain path. Hence, a sequence of cyclones may affect the same areas. As consequence, flooding events can occur. One impressive example was the flooding events in Europe in June 2013. Two blocks over the Atlantic and Scandinavia disturbed the westerly flow and over Europe, three short-lived cyclones, which were triggered by Rossby wave breaking, led to severe weather (Grams et al., 2014). The second possibility for large amounts of precipitation is that a low pressure system is slowly moving or even stationary so that it continuously rains out over a specific region. Such low pressure systems can be found on the flanks of an omega block. Commonly, favorable conditions for floods are triggered by an interaction of different processes, where blocking could be one of the relevant ones, since there is a massive moisture transport via the elongated upstream and downstream troughs. For example the record-breaking floods in Pakistan in summer 2010, which were placed downstream of a blocking ridge, resulted from monsoon surges, extratropical disturbances, and topography (Hong et al., 2011; Houze Jr et al., 2011; Lau and Kim, 2012; Martius et al., 2013).

2.2.6. Predictability

Tibaldi and Molteni (1990) investigated predictability of blocking events in operational ECMWF forecasts for all winters from 1980-81 to 1986-87. One of their results was that only 1/4 of observed blocks are captured by the 10-day forecasts. The predictability of blocks with regards to their genesis, duration and decay is low. The duration is generally underestimated. However, they also found that the predictability is increased if the block is already part of the initial conditions. A comparison between Euro-Atlantic blocks and Pacific blocks showed that Euro-Atlantic blocks are predicted too far east, whereas their Pacific counterparts are predicted too far west. As reasons for the low predictability of atmospheric blocking, Tibaldi and Molteni (1990) mentioned that the models have problems with the transition from a zonal to a meridional flow pattern, as the transition is too slow in the model. Moreover, it is difficult for atmospheric models to handle the large amplitudes of the blocking ridge and the jet splitting correctly, as they tend to reduce the splitting.
In a later study from 2003 by Pelly and Hoskins, ECMWF ensembles for a whole year (summer 2000 to summer 2001) were investigated. They found that the onset is less predictable than the decay, since the onset happens more rapidly. Pelly and Hoskins (2003a) concluded from their investigations that ensemble forecasts are useful for blocking prediction in the short as well as in the medium range, since the forecasts from the EPS are at all lead times more skillful than the deterministic control forecast.
Frederiksen et al. (2004) made ensemble experiments with two atmospheric models and found that the error is larger during the onset or decay phase of a block than during its mature stage. Additionally, the ensemble spread as well as the error grow fast in the blocked region. They concluded that the predictability of weather systems in the Northern hemisphere is generally reduced due to baroclinic transient eddies in the storm track and blocking.

Studies of Matsueda (2009), which were based on ensemble forecasts from 9 EPS, show that the predictability of blocking becomes lower with increasing lead time. He also investigated the predictability in connection to the different regions of occurrence. In the medium range, the prediction of frequencies for Pacific and Euro-Atlantic blocks are quite good. In contrast, the prediction of Greenland and Ural blocks is more difficult. Regarding only the onset phase, the predictability for Pacific blocks is higher than for Euro-Atlantic blocks.
In conclusion, since blocking is associated with a transition from zonal to meridional flow conditions, its prediction is challenging for numerical models. Overall, its predictability depends on the season, the region of occurrence and its life-cycle phase.

2.3. Heat Waves

In the following, heat waves are discussed in more detail. As mentioned in 2.2.5, blocking systems can cause such high impact weather events. In this study, the focus is laid on the Russian heat wave in summer 2010. Hence, previous studies which investigated this event are represented in the last subsection.

2.3.1. Definition and Identification

Heat waves can basically be described as long-lasting periods of unusually high atmosphere-related heat stress which has a highly negative impact on human comfort (Robinson, 2001). As well as maximum temperature, the drop of temperature at night times is also relevant to classify heat waves (Robinson, 2001). However, the World Meteorological Organization (WMO) has not clearly defined the term *heat wave*, yet (Robinson, 2001). In fact, the operational definition differs from country to country, since the temperature sensation of the population depends on the prevailing climate (Gasparrini et al., 2015). The range is from regions characterized by cold temperature (like Canada or Sweden) to areas which are dominated by subtropical or tropical conditions (like Thailand). There are also large countries that do not have a homogenous climate (like China or Russia).
As quantification for heat, different thresholds of certain weather variables are used, like air temperature, relative humidity and wind speed (Davis et al., 2006). Two heat indices are introduced in section 3.2.4.

2.3.2. Conditions and Development

The pattern of occurrence of heat waves in the European-Mediterranean sector can be divided into six classes (Stefanon et al., 2012): the Russian, the Western Europe, the Eastern Europe, the Iberian, the North Sea, and the Scandinavian cluster. All these heat wave patterns have in common that they are triggered by a persistent anticyclonic anomaly, like a block, which has to be in phase with a temperature

anomaly (Stefanon et al., 2012). The pre-conditioning by hydrological conditions can provide favorable conditions for the evolution of heat waves, but is not a criterion which has to be necessarily fulfilled (Stefanon et al., 2012).

A high pressure leads to enhanced subsidence which causes adiabatic atmospheric warming. This is only one part of the increase in temperature. Temperature also increases due to advection of warm air and due to diabatic warming. The advection of warm air can be driven by the wave pattern if the upstream trough of the blocking anticyclone reaches far to the south. Thus, subtropical air can be advected northwards. For the discussion of diabatic processes, we introduce the relevant components with the help of the energy balance (Kraus, 2008):

$$Q - B - H - E = 0 \qquad [2.11]$$

Q is the radiation balance, B the surface heat flux, H the sensible heat flux and E the latent heat flux. The radiation balance is defined as follows (Kraus, 2008):

$$Q = (K\downarrow - K\uparrow) - (L\downarrow - L\uparrow) \qquad [2.12]$$

$K\downarrow$ is the global radiation and $K\uparrow$ the reflected shortwave radiation. $L\downarrow$ is the counterradiation and $L\uparrow$ the emitted longwave radiation. During a heat wave, the controlling high pressure system leads to reduced cloudiness due to increased subsidence. This results in increased downward solar radiation enhancing surface warming (resulting in an enhanced sensible heat flux) and reducing soil moisture. The reduction in soil moisture is equivalent to a reduction in evaporation latent heat flux from land to atmosphere. Moreover, less longwave radiation is emitted and less shortwave radiation is reflected without clouds. Persistent clear sky conditions allow more downward solar radiation, leading to more warming and surface drying, causing even more reduction in clouds. Thus, heat waves have a self-sustaining character, as long as the anticyclonic pattern is dominant.

The end of a heat wave is influenced by the upper level wave pattern. If the blocking decays and low pressure systems become the dominant factor or if a cold front moves to the heat affected area, the heat wave loses its intensity. The heat wave can also end if the blocking anticyclone still exists, but moves. Then, the anticyclonic and the temperature anomaly might be out of phase.

2.3.3. Impact on Society and Economy

The human body is naturally protected against high temperatures, as long as its thermoregulatory system is within its control range, meaning that heat production of the body is balanced by heat loss (Koppe et al., 2004). Two of the most important mechanisms to regulate body temperature are sweating and skin blood flow. Both are essential for thermal regulation during heat stress (Koppe et al., 2004). During heat waves, the risk of heat-related illnesses (like skin eruptions, fatigue, cramps, syncope, exhaustion and stroke) increases. In the worst case scenario, extreme body temperatures can damage cellular structures and the

thermoregulatory system, leading to an increased risk of mortality (Koppe et al., 2004). Susceptibility to heat-related illnesses are dependent on several factors: age, acclimatization, hydration, fitness, body weight, sleep deprivation, or ingested drug affecting the temperature regulation system (Koppe et al., 2004). What does an increased risk of mortality mean in numbers? In a study of Gasparrini et al. (2015), the mortality risk attributable to high and low ambient temperature was investigated for a period from 1985 to 2002, including data from 13 countries. They found that 0.42 % of total mortality was caused by extreme hot temperatures, but even 7 % by extreme coldness. Thus, the effect of extreme coldness is linked to a higher mortality than extreme heat. However, heat waves are one of the deadliest natural phenomenon (e.g. Robine et al., 2008).

Heat waves can cause droughts. Thus, the economic impact, which is discussed below, refers to heat waves and droughts. Summer droughts have a negative influence on water quality and quantity; this is of major interest since water is vital for life. During droughts, the amount of water is reduced and the water quality is for example impaired by heavy metals or major irons (Zwolsman and Van Bokhoven, 2007). This hydrological aspect has in turn an impact on agriculture, since the lack of water can lead to crop failure (Masih et al., 2014). And agriculture is additionally threatened by wildfires, for which the dry conditions are favorable (Haines, 1988; Athanasopoulou et al., 2014). Those fires destroy forests, cultivated fields or even inhabited areas. Another factor is the emission of gases and aerosols, leading to massive air pollution, which has an impact on human health again, as well as on boundary layer dynamics and radiation (Athanasopoulou et al., 2014; Péré et al., 2014). All together, heat waves are extreme events which can cause a massive economic loss (e.g. Kunkel et al., 1999).

2.3.4. Russian Heat Wave 2010

The Russian heat wave in summer 2010 was caused by an enormous high pressure system which blocked the zonal flow for more than two months from mid-June to mid-August (Figure 2.9, Trenberth and Fasullo, 2012). The unusually high surface temperatures and low relative humidity favored wildfires which led to a massive air pollution (Grumm, 2011; Witte et al., 2011). In Russia, 55.000 people died from the consequences of the heat wave. It was the worst drought since 1972 and caused an economic loss about US$15 billion (Barriopedro et al., 2011; Grumm, 2011). Additionally, the heat wave was linked to record-breaking floods in Pakistan, caused by three heavy precipitation events followed by a period of moderate stratiform rainfall (Lau and Kim, 2012). The extreme rainfalls resulted from a combined effect of monsoon surges, extratropical disturbances, and topography (Hong et al., 2011; Houze Jr et al., 2011; Martius et al., 2013). As a consequence, 20 million people were affected by the flooding, with 3000 fatalities (Hong et al., 2011).

The responsible blocking system was favored by different atmospheric and surface conditions. Already in spring 2010, a rapid transition to La Niña conditions was observed. La Niña was providing extra energy and moisture transport from the ocean and created a more diffluent flow over the Atlantic-European sector (Hong et al., 2011; Schneidereit et al., 2012; Trenberth and Fasullo, 2012). Schneidereit et al.

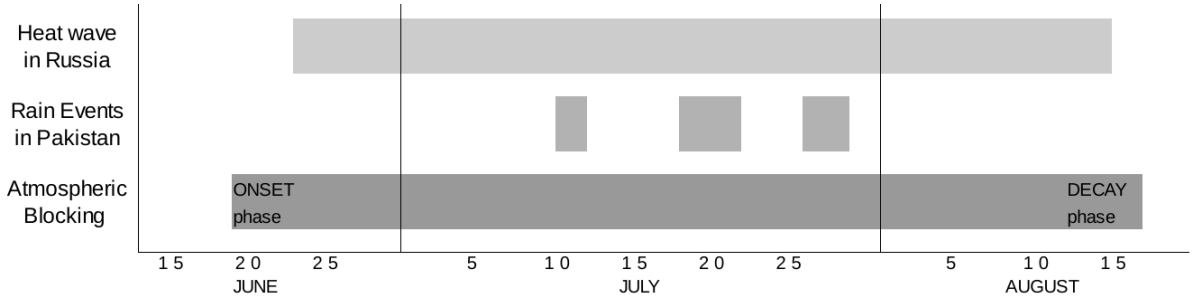

Fig. 2.9.: Time line providing an overview of the atmospheric blocking event over the European-Russian sector, the heat wave in Russia (Barriopedro et al., 2011), and the extreme precipitation events in Pakistan (Lau and Kim, 2012) in summer 2010 (modified from Quandt et al., 2017). ©American Meteorological Society. Used with permission.

(2012) also found that the NAO was in its negative phase and fluctuated in intensity. This influenced the synoptic-scale eddies over the Atlantic which then propagated to the block downstream. Another relevant feature in summer 2010 was a Rossby wave train extending into Europe. It affected the conditions over the Mediterranean and the amplification of the blocking high (Schneidereit et al., 2012; Trenberth and Fasullo, 2012). In addition, during the blocking event, there was a positive feedback between the atmospheric wave pattern and the dry soil with moisture content below normal (Lau and Kim, 2012).
The 2010 Russian heat wave led to record-breaking seasonal temperatures over approximately 50 % of Europe (Barriopedro et al., 2011). Wildfires were also exceptional regarding their intensity and their number (Witte et al., 2011). These phenomena lead to the question whether this heat wave was connected to the anthropogenic climate change. Rahmstorf and Coumou (2011) estimated a probability of 80 % that the 2010 heat record has its origin in climate warming. However, Dole et al. (2011) ranked the intensity of the Russian heat wave within the boundaries of natural variability. These controversial results are discussed in greater detail by Otto et al. (2012).
In this study, we will investigate the evolution of the 2010 Russian heat wave in respect of the forecast variability of the blocking system in the medium range.

3. Medium-Range Forecasts

3.1. Introduction

In this chapter, the focus lies on the forecast variability of the Euro-Russian 2010 summer block in medium-range forecasts. We focus on the three major developmental stages of the block's life cycle: the onset phase, the mature stage, and the decay phase. Medium-range forecasts are suitable for phenomena like blockings and heat waves, since these may be long-lasting. Furthermore, the medium-range development is important for emergency managers and their planning.

Therefore, we will show how differences in the representation of the blocking ridge may impact surface conditions and how these differences arise. Moreover, we will show how to get information about surface impacts from available operational ensemble forecasts. We address the following research questions. Does low predictability of the blocking transfer to a low predictability of the associated high impact weather? What are the main development scenarios of the block in the forecast? Can the scenarios be linked to specific impacts or a lack thereof? What are the relevant dynamical processes which were responsible for the forecast variability?

Data from the THORPEX Interactive Grand Global Ensemble (TIGGE) multi-model ensemble prediction system (EPS) were used (Swinbank et al., 2016). Considering the first and second empirical orthogonal function (EOF), we clustered the ensemble forecast members at the time of high variability (defined here as a large spread between the forecast members within the ensemble) of the block (method adapted form Harr et al., 2008; Keller et al., 2011) and investigated the impact of this variability on the intensity of the heat wave and in the precipitation distribution over Europe, where heavy rain events were reported (e.g. in Austria on 2 August 2010). We further quantify the contributions of the ensemble prediction systems (EPSs), used in this study, to the different development scenarios (corresponding to clusters that resulted from the clustering methodology). For the investigation of the relevant dynamical features that caused the forecast uncertainty, we used a correlation method known as ensemble sensitivity analysis (ESA; Torn and Hakim, 2008; Keller, 2017). An illustration of the data and methods is given in Figure 4.1.

The structure of this chapter is as follows. The data and the methods are presented in section 3.2 and 3.3, followed by the results for the onset phase, the mature stage and the decay phase of the block, starting with the variability patterns, going on with the surface impact and closing with the responsible dynamics. The summary and conclusions are given in the last section.

Several passages are cited from Quandt et al. (2017), wherein all results, except those of the ESA, were already published (©American Meteorological Society).

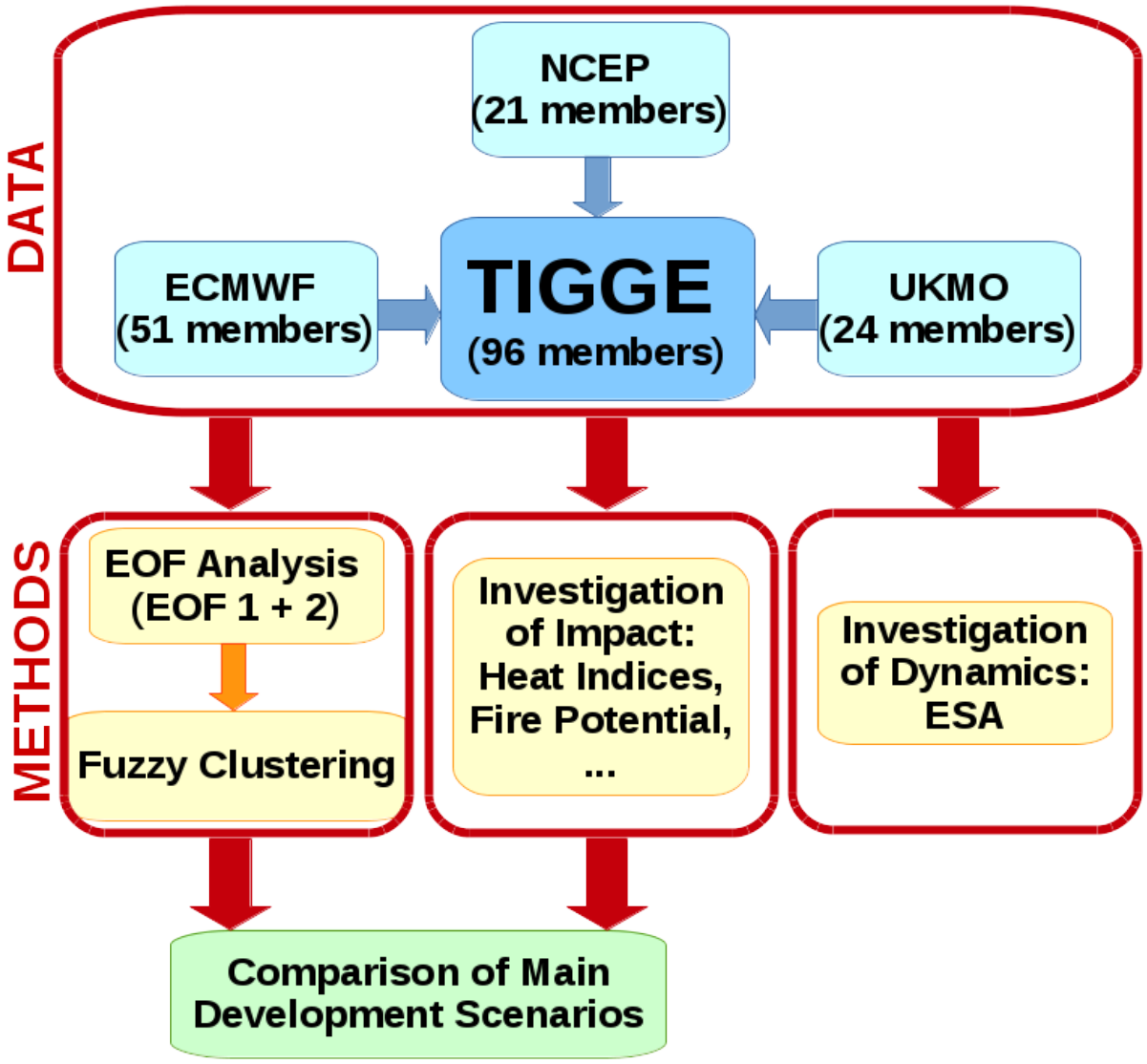

Fig. 3.1.: A schematic overview of data and methods used for the investigations of the predictability of the Russian summer block in 2010 in the medium forecast range.

3.2. Data

We used data from the THORPEX Interactive Grand Global Ensemble (TIGGE) multi-model ensemble prediction system (EPS). The TIGGE project was initiated in 2005 and has the overall goal to accelerate improvements in high impact weather forecasting in the medium range (Bougeault et al., 2010;

Swinbank et al., 2016). To reach that goal, the following objectives were formulated (Bougeault et al., 2010): enhancement of collaborations on ensemble prediction (international as well as between prediction centers and universities), development of new methods to combine ensembles, correction of model bias, and improvement in understanding the contribution of observations, initial and model uncertainties to predictability. In the last decade, studies showed that TIGGE is suitable to investigate predictability and dynamical processes, and to develop new products to support forecasts and warnings for high impact weather (Swinbank et al., 2016). What is of high relevance for this study is that especially in the case of heat waves, the 2 m temperature forecast benefits from the multi-model approach (Bougeault et al., 2010). However, the performance of the multi-model ensemble depends on the integrated individual ensembles. The performance is only better with the multi-model ensemble if each ensemble is equally skillful (Park et al., 2008).

Because one of our blocking identification techniques requires potential temperature on the dynamical tropopause (2 PVU surface) as input variable, only three of the ten EPS in TIGGE could be considered: the European Centre for Medium-Range Weather Forecasts (ECMWF, 51 members), the National Centers for Environmental Prediction (NCEP, 21 members) and the United Kingdom Meteorological Office (UKMO, 24 members). With this selection, each TIGGE forecast contained 96 members. The members were retrieved in 12 hour forecast steps at an interpolated grid of 1° x 1°.

The initial conditions of the three control forecasts at the same spatial resolution as the forecasts were used as analysis data. As these differed only slightly, an unweighted mean of the control runs was used as the "analyzed" scenario, which is referred to as "analysis mean". Since the minimum and maximum temperature variables of the model are defined over the last six hours, we used short-term forecasts of 6 hours for these variables as pseudo-analysis. For total precipitation, first guess daily analysis data based on SYNOP messages from the Global Precipitation Climatology Centre (GPCC), provided by the Deutscher Wetterdienst (DWD), were used as reference (Schamm et al., 2013).

3.3. Methods

3.3.1. Selection of Forecasts

We focused on three different phases of the blocking life-cycle: the onset phase, the mature stage, and the decay period.

To select the forecasts best suited to investigate the onset and decay phases of the blocking, we first determined the onset and the decay of the block. We applied the blocking index of Tibaldi and Molteni (1990) to the analysis data, and identified 20 June as onset date and 17 August as the date of decay (Fig. 3.2). Regarding the decay phase, no blocking was identified in this index between 12 and 14 August. This non-continuous blocking signal reflected the limits of blocking identification. The index failed to identify the block since the block's structure was not favorable for that index (meaning that there were

no overturning features), although the ridge was still amplified (not shown, but visible in the 500 hPa geopotential height field). In the light of these results, we chose forecasts initialized prior to 20 June for the onset phase, and prior to 17 August for the decay phase. Matsueda (2011) mentioned high forecast variability of the block's western flank at the end of July. Hence, for the mature stage, we chose forecasts with initialization times in mid-July. This selection still provided us with a large amount of data, making a further sub-selection necessary. We confined ourselves to one highly variable ensemble forecast for each phase, for which we discussed different main development scenarios of the block in detail.
These forecasts were selected based on ensemble spread maxima in the 500 hPa geopotential field, associated with the block, as revealed in Hovmoeller diagrams averaged between 40°N and 80°N. Selecting the forecasts based on ensemble spread only works for ensemble forecasts in which some members predict blocking. It is not suitable for forecasts in which all members fail to predict the blocking (Matsueda, 2011). In addition, we did the EOF and clustering analysis for more than one forecast for each life-cycle phase of the block. For each phase, we chose the forecast with the most different development scenarios. The forecast uncertainty associated with the blocking high, identified by the blocking index of Tibaldi and Molteni (1990), could be seen clearly in the chosen ensemble forecasts (between 0° and 120°E, Fig. 3.2). For the onset phase, a maximum in 500 hPa geopotential height ensemble spread was located between 0° and 40°E, coinciding with the position of the blocking system. Over the western Atlantic, the ensemble spread was small, indicating only a slight forecast variability upstream of the block around 100°W. During the mature stage, the 500 hPa geopotential height ensemble spread at 20°E and 100°E grew continuously until the end of the forecast time, when values of around 75 gpm were reached. Near the center of the blocking system at 60°E, the ensemble spread was at its minimum pointing to a general high predictability of the block itself. The increased forecast variability corresponded to the flanks of the block, being the troughs upstream and downstream of the blocking ridge, and was investigated for the mature stage of the block. Prior to the decay of the block, the ensemble spread was high in the vicinity of the block, compared to areas farther downstream (around 140°E) and upstream (around 80°W). In all three ensemble forecasts, forecast uncertainty increased over the Pacific (180°). Investigating this aspect of the forecast is not in the scope of this work.

3.3.2. Selection of Main Development Scenarios

Since every forecast contained 96 members, investigating the development in every single member is not expedient. However, if we use an average over all members, we miss important details. Hence, an empirical orthogonal function (EOF) analysis and fuzzy clustering methodology was employed to group members based on characteristic structural features. In this study, we applied the EOF analysis and fuzzy C-Means clustering method (Harr et al., 2008) to the 500 hPa geopotential height.

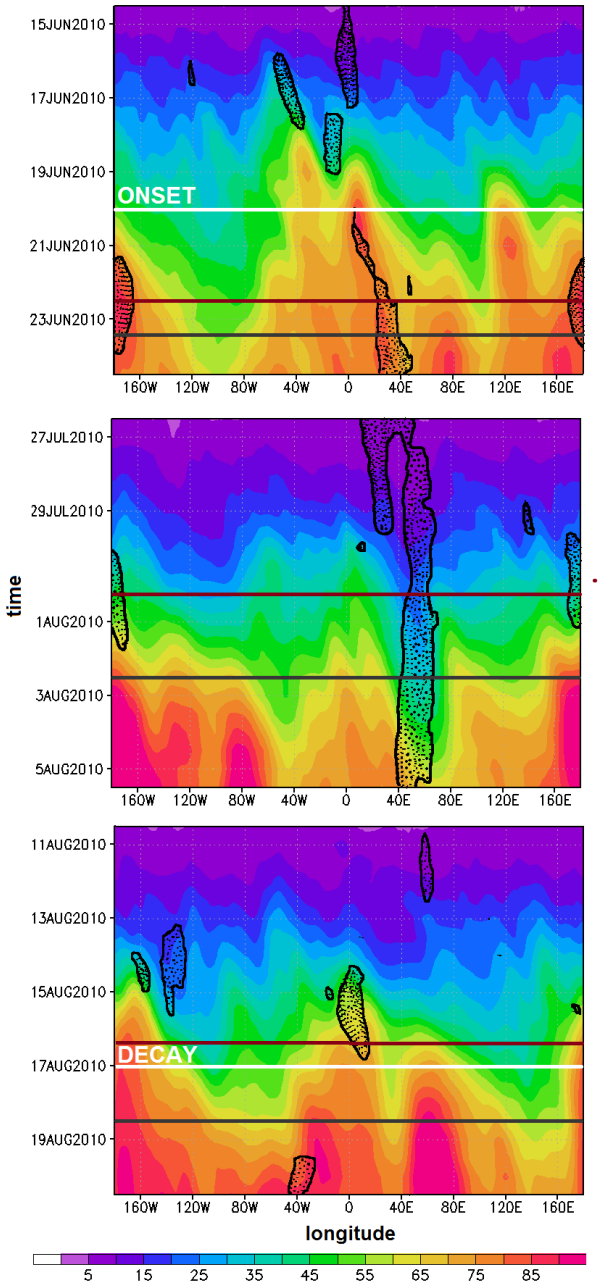

Fig. 3.2.: Hovmoeller diagrams for ensemble spread of 500 hPa geopotential height (in gpm) in the TIGGE EPS 10-day forecasts, averaged between 40°N and 80°N, and positive values of the southern geopotential height gradient (GHGS, in gpm(°latitude)$^{-1}$) of the blocking index of Tibaldi and Molteni (1990) from the analysis mean as black dotted field. Dark red line marks the clustering time and the gray line the investigation time for each forecast. The forecasts are initialized at 1200 UTC 14 June 2010 (top), at 1200 UTC 26 July 2010 (middle), and at 1200 UTC 10 August 2010 (bottom). Figure and caption adopted from Quandt et al. (2017). ©American Meteorological Society. Used with permission.

Empirical Orthogonal Functions

The following derivation of and information about empirical orthogonal functions (EOF) originate from Wilks (2011). The EOF analysis is a multivariate statistical method which is also known as principle component analysis (PCA). The goal of an EOF analysis is to reduce a large dataset without losing information or reducing variability. Therefore, redundant information has to be filtered out in some way. If the variables of a data vector $\vec{x}$ with the dimension $K \times 1$ are correlated, there is redundant information. Hence, a new vector, whose elements are uncorrelated, is created. First, an anomaly vector $\vec{x}'$ of the initial data vector is defined as the deviation from the mean. Then, the eigenvectors of the variance-covariance matrix of $\vec{x}'$ are determined. With these eigenvectors, a reduced data vector $\vec{u}$ with the dimension $M \times 1$ (where $M \ll K$) can be defined. The elements of $\vec{u}$ are named principle components (PC). The mth PC of $\vec{u}$ can be calculated as follows:

$$u_m = (\vec{e}_m)^T \vec{x}' = \sum_{k=1}^{K} e_{km} x'_k \qquad [3.1]$$

where m ranges from 1 to M. $\vec{e}_m$ is the eigenvector of $u_m \cdot \vec{x}'$. The first eigenvector $\vec{e}_1$ points in the direction with the largest variability and has the highest eigenvalue. In line with this, the second eigenvector points in the direction of the second largest variability and is orthogonal to $\vec{e}_1$. Now, the data is regarded in a new phase space, spanned by the eigenvectors. Thus, for $\vec{u}$ we found:

$$\vec{u} = [E]^T \vec{x}' \qquad [3.2]$$

where $[E]$ is the eigenvector matrix. Therefore, the anomaly vector is found to be:

$$\vec{x}' = [E]\vec{u} \qquad [3.3]$$

With the following elements:

$$x'_k = \sum_{m=1}^{M} e_{km} u_m \qquad [3.4]$$

where k ranges from 1 to K. A detailed description of how EOFs are calculated, can be found in Björnsson and Venegas (1997). The derivation above is applicable to a single data vector. In this study, the method was used for a data array.

For the method, it is necessary to determine the time at which the EOF should be calculated (hereafter, referred to as clustering time) as well as the calculation area. Our choice of parameters considered the following criteria (Table 3.1):

- *Clustering Time*: At this time, the ensemble spread associated with the block should noticeable. Thus, we were looking for the strongest variability. This differs from other studies (Anwender et al., 2008; Keller et al., 2011), in which lead times showing the strongest increase in variability were used as clustering times. Hovmoeller plots (Fig. 3.2) and/or spaghetti plots showing the isolines of e.g. a characteristic 500 hPa geopotential height value of all ensemble members (not shown) helped to identify a suitable clustering time. We checked if a shift of the clustering time

to +/- 12 hours had an impact on the cluster solutions. We found that the cluster membership was quite similar for 12 hourly varying clustering times, as quantified by calculating the similarly index of Rand (1971) (not shown). With increasing differences between the clustering times (more than 12 hours), the distribution of members between the clusters differed increasingly, resulting in small values of the Rand index.

- *Calculation Area*: After choosing the clustering time, it is also necessary to determine the area for which the EOFs should be calculated. The calculation area should cover the important flow features, revealed at clustering time. We determined the area using plots of the ensemble mean 500 hPa geopotential height field (not shown).

Since we were interested in medium-range predictability, late clustering times are reasonable. The clustering times are not equal to the investigation times (Table 3.1), clustering times are linked to high variability of the block itself, while the investigation times are associated with high variability in impact relevant surface variables. For the three phases of the block, different lead times turned out to be suitable as investigation times.

Fuzzy Clustering

With the clustering procedure, ensemble members with similar PC (from the EOF analysis) can be grouped. This means that members which have a similar contribution to the variability (corresponding to members with similar development scenarios) are put in one cluster. The method is described in Harr et al. (2008) and Keller et al. (2011).
After the number of clusters were set (for example from 2 to 10), the clustering is conducted as follows.

1. Cluster centers are placed random in the PC1-PC2 phase space.

2. The ensemble members (defined as data points in the PC1-PC2 phase space) are assigned to the nearest cluster center. Assigned members exceed a distinct threshold[1]. If the distance to two or more cluster centers is about the same for a given member (then the mentioned threshold is not exceeded), it is not assigned to a cluster.

3. The cluster centers are re-calculated by minimizing the distance between each center and each member.

4. The ensemble members are re-assigned to the new cluster centers.

This is an iterative process that stops if the ensemble members are not re-assigned anymore, but stay in a certain cluster. Then the cluster centers remain at the same position in the PC1-PC2 phase space.

[1] A membership-matrix is defined that contains the weights of how strong the members are assigned to the clusters. The threshold is calculated as difference between the strongest weight and the standard deviation of the weights.

In addition to the clustering time and the calculation area (which have to be already set for the EOF analysis), the number of clusters has to be determined (Table 3.1):

- *Number of Clusters*: To find the best cluster solution, we ran the clustering procedure for 2 to 10 clusters. With an additional stability criteria (Keller et al., 2011), the number of cluster solutions was limited. This criteria helped to identify solutions for which the clustering did not depend on the initial choice of seed points. For each number of clusters the algorithm was run 100 times, each time with varying and randomly chosen seed points. The solution was declared as stable only if the cluster centers were identical in all 100 cluster runs. The final cluster solution was chosen from those stable solutions so that they showed distinct synoptic developments, but still contained a reasonable amount of members, meaning that e.g. one cluster should not contain only two members.

We use the term *main development scenario* for the forecast scenario represented by one cluster. One commonly used way to illustrate the evolution within the individual clusters is to use the cluster mean. However, the cluster mean is a smoothed version of the individual ensemble members that make up the cluster. Thus, important features (e.g. small-scale features, or shortwave troughs and ridges) can be averaged out (being especially a problem at the end of the forecast when forecast variability is high). An alternative is to chose an individual ensemble forecast that can be considered to represent the cluster as a whole. The members with the smallest Euclidean distance to their cluster center in the phase space, spanned by the first and second PC, are called representative members and were used to compare main development scenarios. Our results were sensitive to the choice of representative members since they were representative for the clustering time. With increasing lead time, the spread between the forecast members becomes larger, also within one cluster. However, after clustering time the differences between members of different clusters are still stronger than differences among members of the same cluster.

3.3.3. Blocking Identification

For the selected main development scenarios, we identified blocking with two blocking indices, which were already introduced in section 2.2.2. The first index is one-dimensional and identifies blocking as overturning of the geopotential height field at 500 hPa (Tibaldi and Molteni, 1990). For each longitude, a southern, as well as a northern gradient of the geopotential height is computed as follows:

$$GHGS = \frac{Z(\Phi_0) - Z(\Phi_S)}{\Phi_0 - \Phi_S} \quad [3.5]$$

$$GHGN = \frac{Z(\Phi_N) - Z(\Phi_0)}{\Phi_N - \Phi_0} \quad [3.6]$$

where Z is the geopotential height in gpm and Φ is the latitude with $\Phi_N = 80°N + \Delta$, $\Phi_0 = 60°N + \Delta$, and $\Phi_S = 40°N + \Delta$ (Δ = -5°, 0° or 5°). A blocking system is identified at a certain longitude if the southern

Tab. 3.1.: Clustering parameters for the three phases of the 2010 summer block over Russia that were investigated. Adopted from Quandt et al. (2017). ©American Meteorological Society. Used with permission.

Clustering Parameters	Onset	Mature Stage	Decay
Initialization	1200 UTC 06/14/10	1200 UTC 07/26/10	1200 UTC 08/10/10
Clustering time	0000 UTC 06/22/10	1200 UTC 07/31/10	1200 UTC 08/16/10
Investigation time	1200 UTC 06/23/10	1200 UTC 08/02/10	1200 UTC 08/18/10
EOF area	40°W-120°E/40-90°N	40°W-120°E/40-90°N	40°W-120°E/40-90°N
No. of clusters	4	3	3
No. of mem. per cluster	22, 18, 20, 20	19, 24, 33	14, 34, 28
	(no cluster: 16)	(no cluster: 20)	(no cluster: 20)

gradient is positive and the northern gradient is less than -10 m (°latitude)$^{-1}$.

The second index identifies Rossby wave breaking (RWB) in the potential temperature field at 2 PVU as indicator for atmospheric blocking (Pelly and Hoskins, 2003b). In its original version, this index is also one-dimensional. Here, we computed a two dimensional version of the index following Woollings et al. (2008). The index is defined as:

$$B = \overline{\theta_N} - \overline{\theta_S} \qquad [3.7]$$

where $\overline{\theta_N}$ and $\overline{\theta_S}$ are northern and southern box averages (5° latitude x 15° longitude) of the potential temperature (in K) at the 2 PVU surface. Blocking is identified for positive values of B (corresponding to $\overline{\theta_N} > \overline{\theta_S}$).

Since both methods have advantages and disadvantages (see section 2.2.2), we employed two indices to increase the probability of correctly identifying blocking. We considered blocking to be present, if the blocking criterion of at least one method was met.

3.3.4. Definition of Impacts

Heat indices and temperature thresholds

To investigate the impact of the heat wave, we used two heat indices and common temperature thresholds. It is reasonable to take more than one heat index into account, because the dependence of human comfort on temperature and humidity differs from region to region (Robinson, 2001; Koppe et al., 2004; Gasparrini et al., 2015). These indices represent heat stress in a simplified way, but are better suited to capture the effect of heat on humans than the 2 m temperature, because they also consider moisture (being important for regarding humid heat).

The first index is the heat index (HI) used operationally by the U.S. National Centers for Environmental Prediction (NCEP)[2]. It is defined as follows:

$$\begin{aligned} \mathrm{HI} = c_1 + (c_2 T) + (c_3 \mathrm{RH}) - (c_4 T \cdot \mathrm{RH}) - (c_5 T^2) - \\ (c_6 \mathrm{RH}^2) + (c_7 T^2 \mathrm{RH}) + (c_8 T \cdot \mathrm{RH}^2) - (c_9 T^2 \mathrm{RH}^2) \end{aligned} \quad [3.8]$$

where T is the temperature at 2 m in °F and RH the surface relative humidity in %. The equation of the HI used here and the c-values[3] are an approximation to a heat stress model of Steadman (1979). The critical thresholds of the heat index can be found in Table 3.2.

The second index called Humidex is discussed in Masterton and Richardson (1979) and is operationally used by Environment Canada (EC)[4]. The Humidex is defined as:

$$\mathrm{Humidex} = \vartheta + \frac{5}{9}(e - 10) \quad [3.9]$$

where ϑ is the temperature in °C at 2 m and e the vapor pressure in hPa. The Humidex can be understood as air temperature plus a value that considers the impact of moisture. The four warning levels are described in Table 3.3.

For the Humidex, temperature has a stronger impact than humidity. Thus, in general, Humidex decreases as latitude increases, following the annual mean surface temperature.[5] For the HI, temperature and humidity contribute similarly. Nevertheless, for example above 50°N, a portion of high HI values are only artifacts of high humidity, since temperature does not reach values over 20°C. Consequently, it is necessary to filter the HI (taking account of the temperature range). As both indices are dependent on latitude and as Russia is located at approximately the same latitudes as Canada, the Canadian Humidex seemed to be more suitable to investigate a heat wave in Russia. In this study, we compared the heat intensity represented in one forecast scenario to those represented by another forecast scenario, thus, it is more a *relative* consideration. For investigations which aim to more *absolute* results, it could be necessary to adapt the danger thresholds. For the Mediterranean region for example, the danger thresholds of the Humidex could be scaled up, since the population has a higher physical tolerance against hot temperatures.

In addition to these heat indices, we also looked at the temporal evolution of the spatially averaged maximum (minimum) temperature in the daytime (at nighttime). We discussed the extreme temperatures using the following thresholds: *extremely hot day* ($\vartheta_{max} \geq 35$°C), *hot day* ($\vartheta_{max} \geq 30$°C), *summer day* ($\vartheta_{max} \geq 25$°C) and *tropical night* ($\vartheta_{min} \geq 20$°C). We considered these temperature thresholds, since they are commonly used and to show the evolution of "dry" heat (since moisture is not considered).

We averaged the 2 m temperature, as well as the heat indices over the region with the strongest heat wave intensity centered over Moscow (35°E-55°E and 50°N-60°N, see also Figs. 3.7 and 3.23; Dole et al.,

[2] `http://www.wpc.ncep.noaa.gov/html/heatindex_equation.shtml`

[3] $c_1 = 42.379$, $c_2 = 2.04901523$, $c_3 = 10.14333127$, $c_4 = 0.22475541$, $c_5 = 6.83783e(-3)$, $c_6 = 5.481717e(-2)$, $c_7 = 1.22874e(-3)$, $c_8 = 8.5282e(-4)$ and $c_9 = 1.99e(-6)$

[4] `http://ec.gc.ca/meteo-weather/default.asp?lang=En&n=6C5D4990-1#humidex`

[5] `http://ec.gc.ca/meteo-weather/default.asp?lang=En&n=6C5D4990-1#humidex`

Tab. 3.2.: Ranges of the NCEP heat index and the associated warning levels (adopted from: http://www.srh.noaa.gov/ama/?n=heatindex).

Heat index	Degree of Danger
27-32	Caution: Fatigue possible with prolonged exposure and/or physical activity.
33-41	Extreme Caution: Sunstroke muscle cramps, and/or heat exhaustion possible with prolonged exposure and/or physical activity.
41-54	Danger: Sunstroke, muscle cramps, and/or heat exhaustion likely. Heatstroke possible with prolonged exposure and/or physical activity.
>54	Extreme Danger: Heat stroke likely

Tab. 3.3.: Ranges of Humidex and the associated warning levels (adopted from: http://ec.gc.ca/meteo-weather/default.asp?lang=En&n=6C5D4990-1#humidex).

Humidex	Degree of Comfort
20-29	No discomfort
30-39	Some discomfort
40-45	Great discomfort; avoid exertion
>45	Dangerous; possible heat stroke

2011). As 11,92 million people live in Moscow, we also focused on the coordinates of this city, namely 55,75°N and 37,62°E, and averaged the indices over just the four surrounding grid points.

Wildfire potential

Widespread wildfires were one of the most devastating impacts of the Russian heat wave in 2010 (Witte et al., 2011) and are hence of interest in this study. For our studies, we used the lower atmosphere severity index (LASI) for wildlife fires of Haines (1988):

$$\mathrm{LASI} = (\vartheta_{p1} - \vartheta_{p2}) + (\vartheta_{p2} - \tau_{p2}) \qquad [3.10]$$

where ϑ is the temperature and τ the dew point, both in °C. $p1$ and $p2$ are pressure levels in the lower troposphere, with $p1$ at a lower height than $p2$. The first term describes the stability of the atmosphere, whereas the second part of the index is the moisture term. The resulting values of both terms are assigned to factor values between 1 and 3. These factor values are then added. This sum is the effective LASI with a range between 2 and 6. There are three configurations of LASI that are adjusted to the different

Tab. 3.4.: Ranges of the LASI and the associated danger classes adapted from Haines (1988).

LASI	Danger class
2 or 3	very low
4	low
5	moderate
6	high

elevation levels (low, mid and high) of the United States. Following Witte et al. (2011), we confined the computation of the LASI to a region where active fires were observed (from 37°E to 49°E and from 51°N to 57°N). The geographical height of this region varies from 130 to 200 m above sea level, requiring the use of the low-elevation index. The stability is calculated between 950 hPa and 850 hPa and the moisture term is defined for 850 hPa (corresponding to $p2$). As the required input variables from TIGGE are not available at 950 hPa, we used the variables at 925 hPa (corresponding to $p1$). This results in an overestimation of the stability term, leading to an overestimation of the LASI itself (Potter et al., 2008). The LASI is separated into four danger classes (Table 3.4), indicating the probability for wildfires.
LASI does not consider surface conditions like soil moisture, however, it represents atmospheric conditions which influence fire behavior as well (Brotak, 1991). Thus, it can be interpreted as an indicator whether the vertical lapse rate and the amount of moisture in the air are favorable for the fire evolution (Brotak, 1991). Although LASI was developed for predicting the fire risk in the United States, it was also employed successfully outside the United States, e.g. in Korea (Choi et al., 2006) or Australia (McCaw et al., 2007).

3.3.5. Ensemble Sensitivity Analysis

Basic Idea

The ensemble sensitivity analysis (ESA) is a tool that is used in this thesis to obtain insight into the physical and dynamical mechanisms that play a role in blocking and in the associated forecast uncertainty. It was developed to quantify how initial conditions influence the forecast at later lead times (Torn and Hakim, 2008; Torn, 2010b; Zheng et al., 2013). Thus, the idea is that small deviations of a state variable from the ensemble mean at time t are correlated to deviations of a forecast metric from the ensemble mean at time t+Δt (being defined as metric time). It is defined as (Torn and Hakim, 2008):

$$\text{sens} = \frac{\partial \mathbb{J}}{\partial \mathbb{X}} \cdot \sigma_x = \frac{\text{cov}(\mathbb{J}, \mathbb{X})}{\text{var}(\mathbb{X}, \mathbb{X})} \cdot \sigma_x \qquad [3.11]$$

where $\mathbb{X}$ is an independent state variable, $\mathbb{J}$ the forecast metric and σ_x the standard deviation of the state variable. Due to the normalization with σ_x, changes in the forecast metric between the ensemble mem-

bers go with 1 σ_x changes in the state variable between the ensemble members (Keller, 2017). This is beneficial, since the sensitivities of different state variables can then be compared. Advantages of the ESA are that it can be calculated easily and that the forecast metric can be chosen flexibly (Chang et al., 2013). A disadvantage, being more a limitation of the method, is that it cannot be used to investigate nonlinear relationships, since linear error growth is assumed (Keller, 2017). For this study, it is also of relevance that the method is suitable for medium-range forecasts. Although a medium-range forecast is clearly nonlinear, so that ESA is formally not valid to investigate the evolution, previous studies have demonstrated that the method can be used because also linear sensitivities have an impact on the nonlinear evolution of certain weather systems (Chang et al., 2013).

In this study, we used ESA to identify the dynamical processes which led to the forecast variability at clustering time. Thus, our clustering times were chosen as metric times. For an individual ensemble member, $\mathbb{X}$ is here a 2D array of a forecast variable (for example PV at 320 K) and $\mathbb{J}$ a single value (for example the peak in the geopotential height at 500 hPa). In 12 hourly time steps, we calculated sensitivities until 6 days before metric time, corresponding to results of Chang et al. (2013). In the case of the mature stage of the block, we only went back to 4 days, since earlier times are affected by the "memory of initial conditions" (Torn and Hakim, 2008), meaning that the variability is mainly caused by the disturbances in initial conditions. Moreover, following Torn and Hakim (2008) and Keller (2017), only sensitivities on a 95 % level of significance are considered.

Metrics

A forecast metric describes the object (for example a certain flow feature), with regard to which the sensitivities are calculated. Therefore, the metric should capture the variability of this object within the ensemble forecast. In the following, the forecast metrics for the three different phases of the block (corresponding to three ensemble forecasts) are presented. In addition to those shown here, we also tested several other metrics. We only present the metrics which turned out to be most suitable in terms of significance and clarity of the resulting ESA signals.

To represent the blocking system during its onset phase, we chose the peak value in the 500 hPa geopotential height field as forecast metric. We used the geopotential height maximum within the box which can be seen in Figure 3.3 (top). The idea behind this approach was that the maximum geopotential height value reflects the amplitude of the blocking ridge. Thus, with a trough or a less amplified ridge, we expect low values and with a strongly amplified ridge corresponding to a blocking ridge, we expect high values.

During the mature stage of the block, the variability of its western flank is of interest. We chose a difference of two spatial averages of two neighboring boxes as forecast metric. The idea was to create a metric which reflects the position and/or the tilt of the trough upstream of the blocking ridge. In the middle panel of Figure 3.3, it is shown that the boxes captured the variability of the troughs at 0° in the 500 hPa geopotential height field. The variability within the boxes can be seen in the spread between the

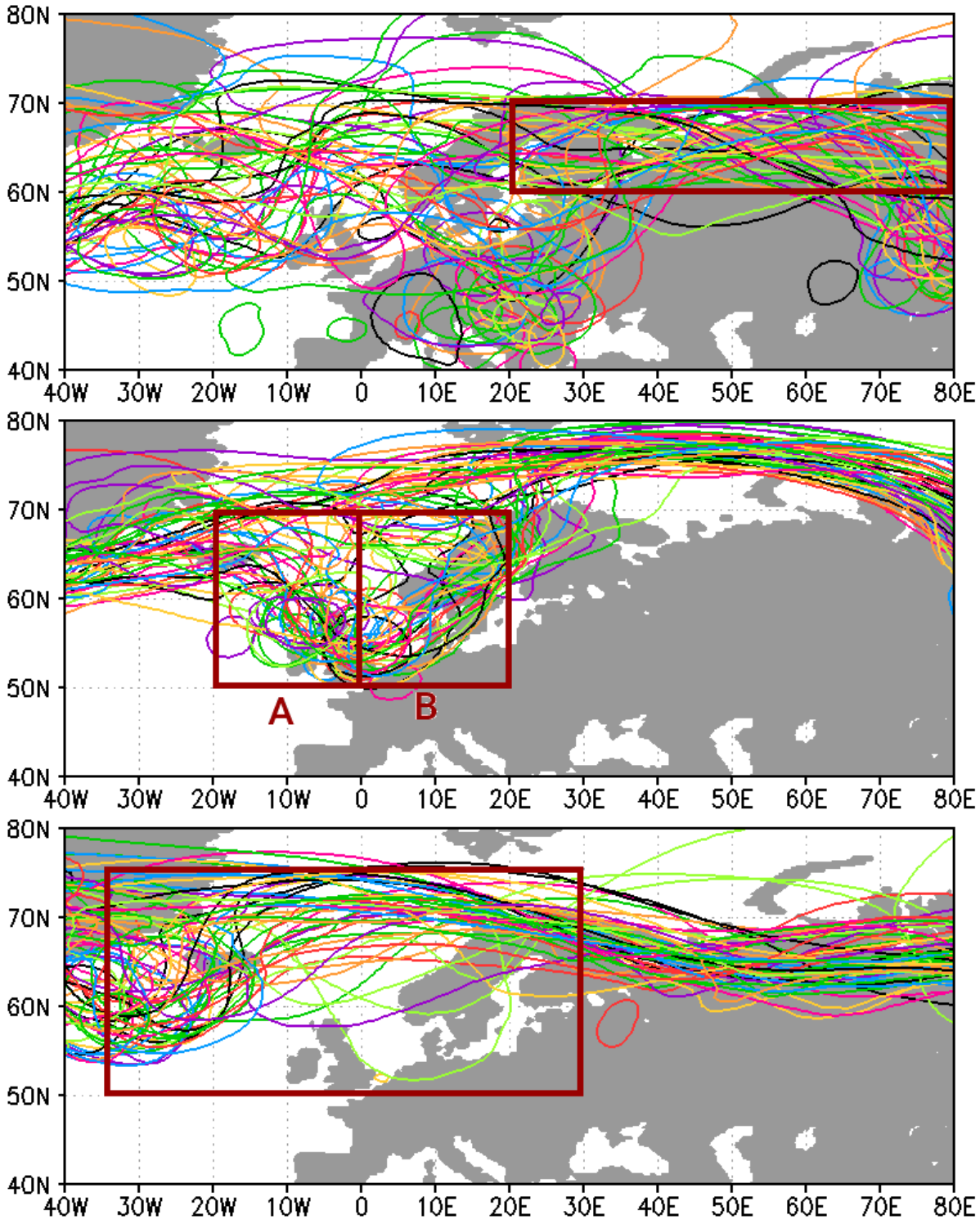

Fig. 3.3.: (top) 5600 gpm isolines of all ensemble members at 1200 UTC 22 June 2010 for the forecast initialized at 1200 UTC 14 June 2010. Dark red box marks the area for which the peak value of 500 hPa geopotential height was determined. (Middle) 5600 gpm isolines of all ensemble members at 1200 UTC 31 July 2010 for the forecast initialized at 1200 UTC 26 July 2010. Dark red boxes mark the areas over which the 500 hPa geopotential height was averaged. (Bottom) 5600 gpm isolines of all ensemble members at 1200 UTC 16 August 2010 for the forecast initialized at 1200 UTC 10 August 2010. Dark red box marks the area over which the 500 hPa geopotential height was averaged.

5600 gpm isolines of all ensemble members. The spatial mean of box B is subtracted from the spatial mean of box A. Thus, if the geopotential height is lower in box A than in box B, the index is negative. It is positive if the geopotential height is higher in box A than in box B. Therefore, positive values of the index reflect an eastward shifted trough without tilt or LC2 (cyclonic wave breaking), while negative values reflect a westward shifted trough without tilt or LC1 (anticyclonic wave breaking). The position and the tilt of the trough influence the precipitation distribution over Europe (as will be discussed in section 3.4.2). For the forecast used for the investigation of the mature stage of the block, we found that 41 % of the ensemble members exhibited a positive index value, with 25 % showing a LC2 and 16 % showing a trough shifted to the east. 39 % of the ensemble members exhibited a negative index value, with 16 % showing a LC1 and 23 % showing a trough shifted to the west. The remaining ensemble members (20 %) had index values close to zero, corresponding to a trough without a noticeable tilt centered at 0° (in the middle of the boxes A and B).
To represent the blocking system during its decay phase, we chose the spatial mean in the 500 hPa geopotential height field as forecast metric. In Figure 3.3 (bottom), the box, for which the spatial mean was calculated, is shown. Due to movements of the block during its life-cycle, this metric box has a different location as that one for the onset phase. High values corresponded to a larger geopotential height, reflecting that the block was still there. Low values mirrored low geopotential height which can be interpreted as a flow configuration without an amplified blocking ridge.

Variables

The metrics are correlated to different state variables. To investigate the impact of weather systems and the feedback of waves on the block as well as jet splitting and displacement, we used the following variables and quantities:

- Mean sea level pressure (MSLP)
- Transient eddies (TE)
- Geopotential height at 500 hPa
- PV at 320 K
- Potential temperature at 2 PVU
- Horizontal wind speed at 200 hPa

All but the transient eddies are variables which are available in the TIGGE dataset. We calculated transient eddies as the deviation of the instantaneous 500 hPa geopotential height field in the forecast from the monthly mean (as calculated from ERA-Interim data). For the investigation of diabatic processes we used the following variables and quantities:

Tab. 3.5.: Assistance for interpretation of ESA signals for the onset and the decay phase of the block.

variable/quantities	positive ESA signal	negative ESA signal
Geopotential height at 500 hPa, MSLP, potential temperature at 2 PVU, TE	within ridge/high, favorable for block; within trough/low, unfavorable for block	within ridge/high, unfavorable for block; within trough/low, favorable for block
PV at 320 K	within ridge, unfavorable for block; within trough, favorable for block	within ridge, favorable for block; within trough, unfavorable for block
AR, precipitation, horizontal wind speed at 200 hPa	increase favorable for block; decrease unfavorable for block	increase unfavorable for block; decrease favorable for block

Tab. 3.6.: Assistance for interpretation of ESA signals for the mature stage of the block. An increase in the metric corresponds to cyclonic wave breaking (CWB) or an eastward shift of the trough. A decrease in the metric corresponds to anticyclonic wave breaking (AWB) or a westward shift of the trough.

variable/quantities	increase in the metric	decrease in the metric
Geopotential height at 500 hPa, MSLP, potential temperature at 2 PVU, TE	positive sensitivity within ridge/high; negative sensitivity within trough/low	positive sensitivity within trough/low; negative sensitivity within ridge/high
PV at 320 K	positive sensitivity within trough/low; negative sensitivity within ridge/high	positive sensitivity within ridge/high; negative sensitivity within trough/low
AR, precipitation, horizontal wind speed at 200 hPa	positive sensitivity where variable increases; negative sensitivity where variable decreases	positive sensitivity where variable decreases; negative sensitivity where variable increases

- 12 hourly accumulated precipitation.

- Atmospheric rivers (AR).

Atmospheric rivers are mesoscale filaments of high water vapor transport in the troposphere (Neiman et al., 2008; Lavers et al., 2012). On average, they are over 2000 km long and less than 1000 km wide (Neiman et al., 2008), can persist for 18 hours or longer (Lavers et al., 2012), form in the warm sector of low pressure systems and play an important role in the global water cycle (Neiman et al., 2008; Ralph and Dettinger, 2011). As they make landfall (especially at mountains), the moist air is forced to ascend so that water vapor condenses, causing large amounts of precipitation and maybe even flooding events (Ralph and Dettinger, 2011; Lavers et al., 2012; Lavers and Villarini, 2013). For detection, AR can be calculated as vertically integrated water vapor transport (*IVT*; Lavers et al., 2012; Lavers and Villarini, 2013):

$$IVT = \sqrt{\left(\frac{1}{g}\int_{1000}^{300} qu\,dp\right)^2 + \left(\frac{1}{g}\int_{1000}^{300} qv\,dp\right)^2} \qquad [3.12]$$

where g is the acceleration due to gravity, q the specific humidity in kg kg^{-1}, u and v the zonal and meridional wind components in m s^{-1}. We used ARs for the investigation of diabatic forcing as alternative for WCBs, since there are not enough vertical levels in the TIGGE dataset for calculating WCB trajectories (Eckhardt et al., 2004). ARs and WCBs are different phenomena, but are strongly connected, since ARs can be seen as moisture reservoirs for WCBs (Sodemann and Stohl, 2013).
Tables 3.5 and 3.6 provide a guide on how to interpret the positive and negative ESA signals for the metrics and variables used in this study.

3.4. Results

Three phases of the block's life-cycle are considered: the onset phase of the block, the mature stage, and the decay phase. For each phase, the forecast variability (in terms of the EOF patterns and the differences between the development scenarios), the surface impact (addressing the heat wave evolution and precipitation), as well as the dynamical processes which caused the forecast variability are discussed.

3.4.1. Forecast Variability during the Onset Phase of the Block

Selection and Characteristics of Forecast Scenarios

The spatial EOF patterns indicate those flow features that show largest variability in the 500 hPa geopotential height among the EPS members at +180 forecast hours. The strongest variability was represented by EOF 1 with 24.5 %. Positive values (corresponding to higher geopotential height, and therefore to ridges) and negative values (corresponding to lower geopotential height, and therefore to troughs) could

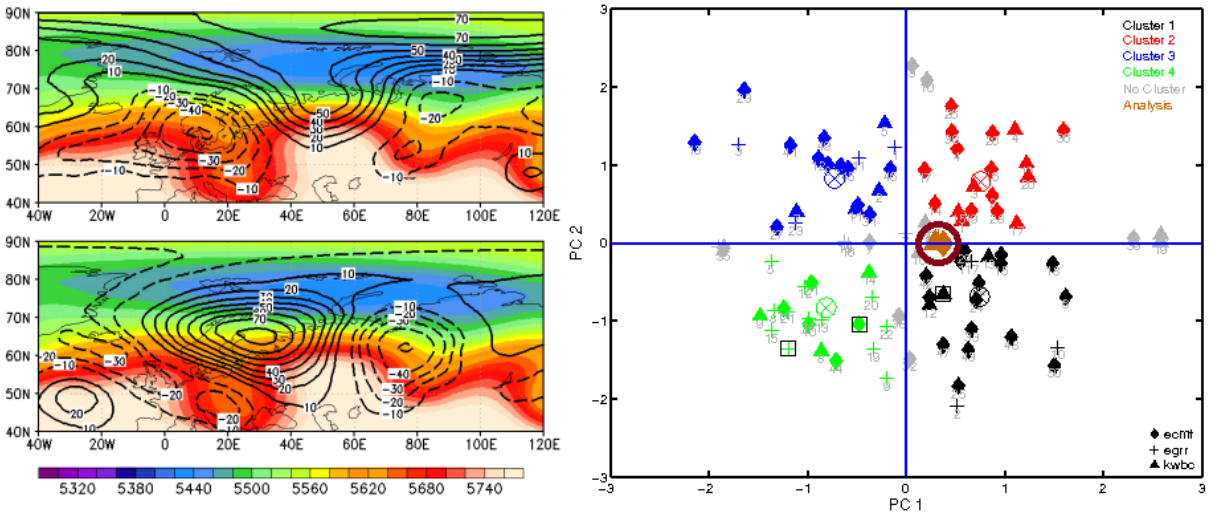

Fig. 3.4.: (left) Ensemble mean of the 500 hPa geopotential height (shaded, in gpm) and distribution of (top) EOF 1 and (bottom) EOF 2 (contours, in gpm) for blocking onset forecast at +180 hours (0000 UTC 22 June 2010). (right) The first and second principle component (PC) for the four-cluster solution based on EOFs from TIGGE ensemble members (forecast initialized 1200 UTC 14 June 2010) at +180 hours (0000 UTC 22 June 2010). Symbols show the EPS membership (rhombus for ECMWF, triangle for NCEP, and cross for UKMO) and colors the cluster membership. Cluster centers are defined by the circled cross. The analysis members are additionally circled in dark red. Figures and caption adopted from Quandt et al. (2017). ©American Meteorological Society. Used with permission.

be found along the block that was located around 60°E (Figure 3.4, left, top). Negative values of EOF 1 were located in the upstream (round 20°E) and downstream troughs (around 80°E) of the blocking ridge. Positive values of EOF 1 were found in the peak of the blocking ridge and at latitudes higher than 70°N. This distribution resembled an amplitude pattern (Anwender et al., 2008). A positively contributing member showed the blocking ridge to be more amplified and the upstream and downstream troughs to be deeper in their geopotential height, compared to the ensemble mean. Moreover, the blocking ridge was narrower in its zonal expansion, whereas the neighboring troughs had a large zonal extent. A forecast member with a negative contribution to EOF 1 was characterized by a less amplified blocking ridge and the upstream and downstream troughs had a less zonal extend. Additionally, an area of low geopotential height was found around 80°N.

The second strongest variability that was represented by EOF 2 amounted to 11.8 % (Figure 3.4, left, bottom). It resembled a shift pattern following Anwender et al. (2008). There was a dipole with a positive signal of EOF 2 to the west and a negative signal to the east of the ridge axis at 60°E. In a forecast member with positive contribution to EOF 2, the blocking ridge was shifted to the west. In addition, a massive cut-off low was located at 40°E/45°N. A negatively contributing member forecast the blocking ridge farther east. The wave structure between 40°W and 120°E showed a double ridge pattern with a trough around 30°E and two small cut-off systems at 20°W and 70°E.

Four clusters turned out to be most suitable, since this solution was stable and the scenarios of the clusters showed clear differences (Table 3.1). All four clusters contained approximately 20 ensemble members, indicating their equal probability of occurrence in this ensemble forecast (Figure 3.4, right). In the PC phase space the three analysis members were located between cluster 1 and 2. The forecast members from the three different EPS contributed to the four clusters as follows: The ECMWF and the NCEP EPS were present in all four main scenarios, while UKMO missed one of the development scenarios and had most of its members in cluster 4. Thus, the full range of development scenarios could not be captured by the UKMO ensemble, which was dominated by the scenario of cluster 4. This shows the added value of the TIGGE ensemble, as more scenarios were captured than with the UKMO ensemble alone.

Main Development Scenarios for the Onset

At 1200 UTC 23 June (+216 hours forecast), the blocking system (between 20°E and 80°E) had formed in three of the four scenarios (Fig. 3.5). The index of Tibaldi and Molteni (1990) identified the block in scenario 2 and 3, the index of Pelly and Hoskins (2003b) in scenario 1 and 2. The position of the blocking ridge in scenario 1 and 2 was quite similar, but its shape was different. The trough upstream of the block was narrower in scenario 2, while the downstream trough was positioned farther west (at 80°E). The trough downstream was positioned farther east (at 110°E) in scenario 1. Northwest of the blocking system at around 80°N, higher potential temperature on the 2 PVU surface was present in scenario 2, indicating a stronger blocking. In scenario 3, the blocking system merged with an upstream ridge. As a result, the blocking complex was zonally more extended compared to the blocks in scenario 1 and 2. Another difference were two merging cut-off systems between 0° and 40°E at 40°N. In the *no-blocking* scenario 4, the ridges and troughs over the Atlantic-European sector were less amplified, leading to more zonal flow conditions. Around 70°N, an area of low pressure stretched from 20°W to 80°E. Scenario 1 and 2 coincided best with the analysis mean, despite differences in the area of low pressure north of the block (between 70°N and 80°N) and in the pressure field just below the blocking ridge.

Forecast Variability of impact-related Parameters

We will now focus on the influence of the blocking system on surface variables. At 1200 UTC 23 June (+216 hours forecast), the surface temperatures over Moscow became uncomfortable in the analysis (Fig. 3.6). In scenario 1, hot temperatures could be found in the region east of Moscow and HI as well as Humidex indicated no warning for Moscow itself. This was different in scenario 2, where the 2 m temperatures were higher near Moscow and the first warning level of the two heat indices was reached. Scenario 3 showed the city in a border area with higher temperatures to the south. In scenario 4, the extreme heat was confined to the south of 50°N.

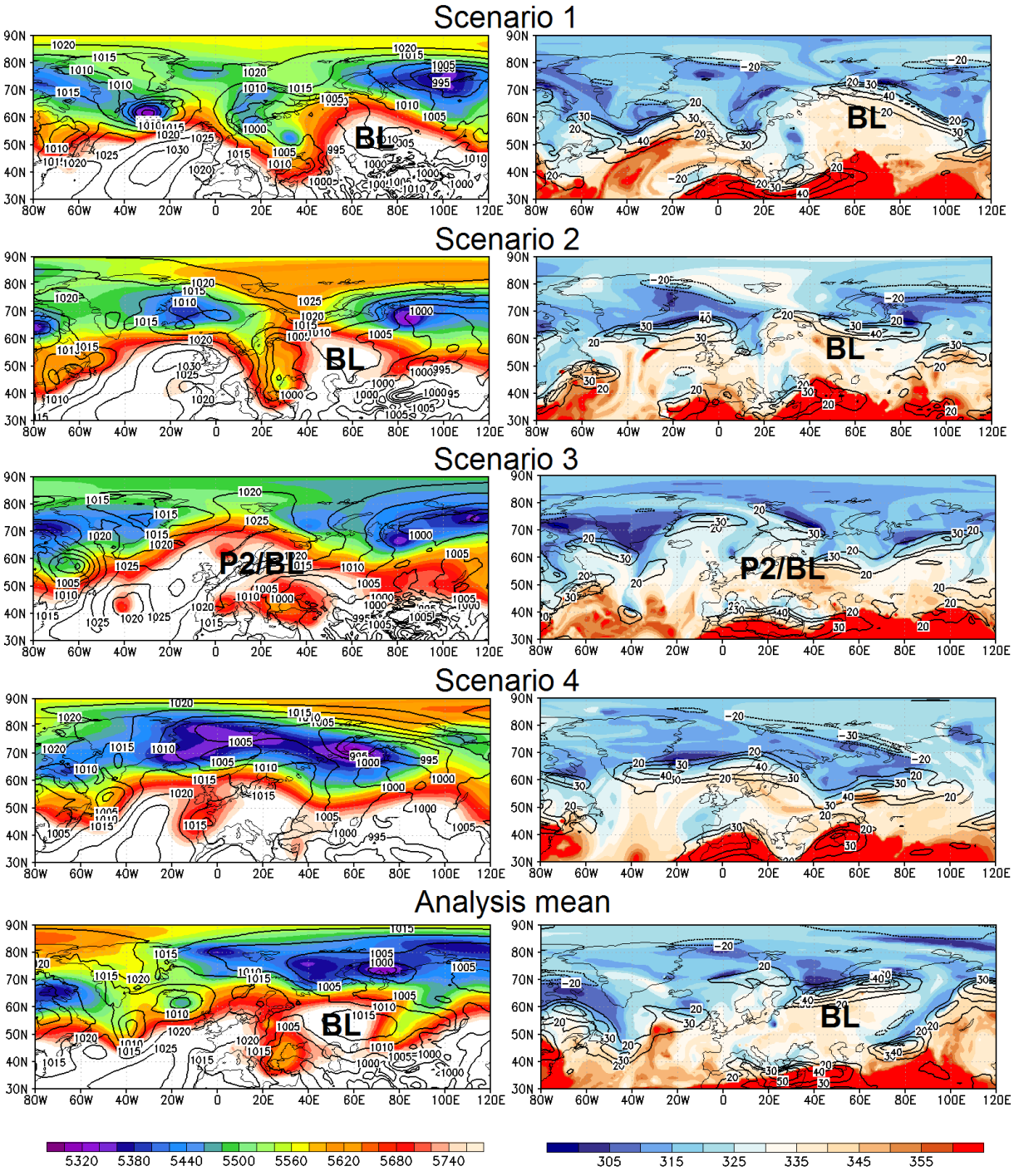

Fig. 3.5.: (left) 500 hPa geopotential height (shaded, in gpm) and mean sea level pressure (contours, in hPa), (right) potential temperature at 2 PVU (shaded, in K) and 300 hPa zonal wind (contours, in m s^{-1}) at +216 hours (1200 UTC 23 June 2010) for the four forecast main scenarios and the analysis mean for blocking onset. BL marks the blocking system. P2 marks the position of poleward anticyclonic RWB (Gabriel and Peters, 2008). Figure and caption adopted from Quandt et al. (2017).©American Meteorological Society. Used with permission.

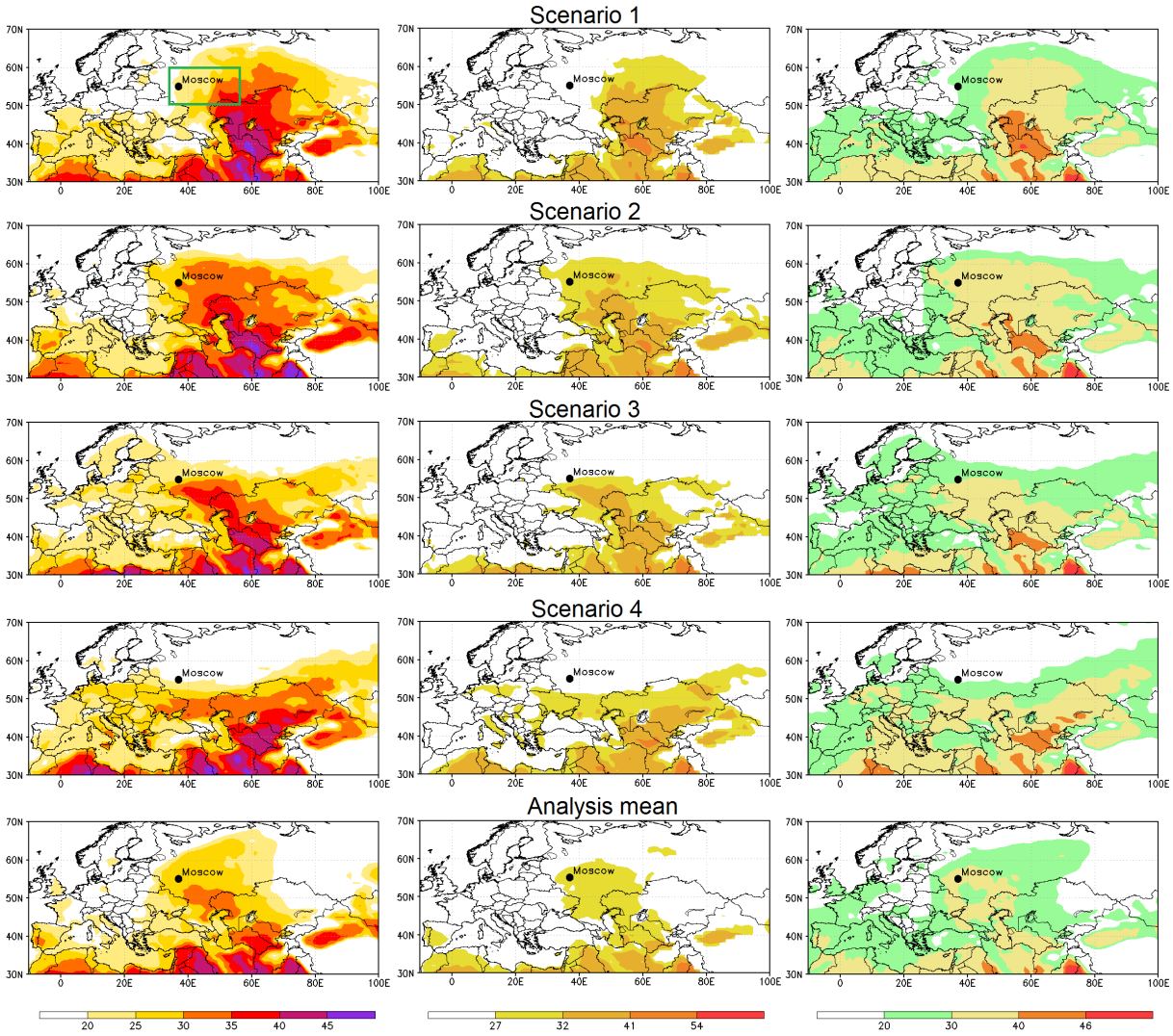

Fig. 3.6.: (left) 2 m temperature, (middle) HI and (right) Humidex (all in °C) at +216 hours (1200 UTC 23 June 2010) for the four main forecast scenarios and the analysis mean for blocking onset. The green box marks the region for which we calculated the averaged temperatures (for Fig. 3.7). Figure and caption adopted from Quandt et al. (2017). ©American Meteorological Society. Used with permission.

In three of four scenarios, the blocking ridge was forecast, however details varied significantly. Accordingly, the surface temperature distribution differed in all main development scenarios, leading to varying heat intensities for different areas (Fig. 3.6). Interestingly, the scenarios that captured the upper-level flow best exhibited remarkable differences in their representation of the surface temperature compared to the analysis mean. Before, we found for the wave pattern that scenario 1 and 2 coincided best with the analysis mean. However, scenario 1 and 2 overestimated the temperature, especially for the area southeast of Moscow.

The spatially averaged temperatures (showing us the temporal evolution of the heat wave) increased with time from 19 June onward in all scenarios except scenario 4 (Fig. 3.7). This increase coincided with blocking onset. In scenario 2, the increase was most prominent, and the threshold for a *hot day* was reached. The maximum temperatures of scenario 1 and 3, as well as of the short-term forecast (corresponding to the analysis mean) only reached the threshold for a *summer day*. Thus, the temperatures in scenario 2 were overestimated. Moreover, in scenario 1 to 3, the threshold for a *summer day* was reached at least one day too early compared to the short-term forecast. In scenario 4, the non-block scenario, temperature decreased until 21 June. At nighttime, the minimum temperatures did not reach the threshold for a *tropical night*, either in the analysis or the forecast scenarios. The impact of this temperature evolution could be further investigated by means of the heat indices. The second warning level of the Humidex, representing *some discomfort*, was reached in scenario 2 on 21 June. However, this was an overestimate compared to the analysis mean, which reached this level on June 24. The HI of scenario 2 was overestimated, also approaching the threshold for *extreme caution*. Scenario 2 and 3 reached the *caution* level already around 21 June. In scenario 1, this level was reached one day later, in agreement with the analysis mean.

The spatially averaged LASI (averaging area: 37-49°E and 51-57°N), indicating fire potential, was in line with the findings above: In scenario 2 and 3, the LASI increased in time (Fig. 3.7). The strongest increase could be found around blocking onset, leading to values just under 5, indicating a *moderate* potential for fire. This increase could be observed in scenario 1 also, but in accordance with temperature there was a decrease after 21 June. In scenario 1 to 3, the threshold for *low* fire potential was reached one day too early compared to the analysis mean. The LASI for scenario 4 indicated a *very low* potential for large fires. On 23 June, the LASI in all forecast scenarios was below the analysis mean. For scenario 2 to 4 and for the analysis mean, the LASI increased with blocking onset. However, not in scenario 1. One possible explanation considers the differences in the representation of the western flank of the blocking system (Fig. 3.5): The trough at 30°E was deeper in scenario 1, compared to the troughs in scenarios 2 and 3 as well as in the analysis mean. This was relevant, since parts of the block's western flank were inside the averaging area for the LASI.

For Moscow, temperature increased in all scenarios (Fig. 3.8), but the threshold for a *summer day* (25°C) was not reached in scenario 1 and 4. In scenario 2 and 3, 25°C were reached one day too early compared to the short-term forecast. After 20 June, the date of the block's onset, the HI increased continuously

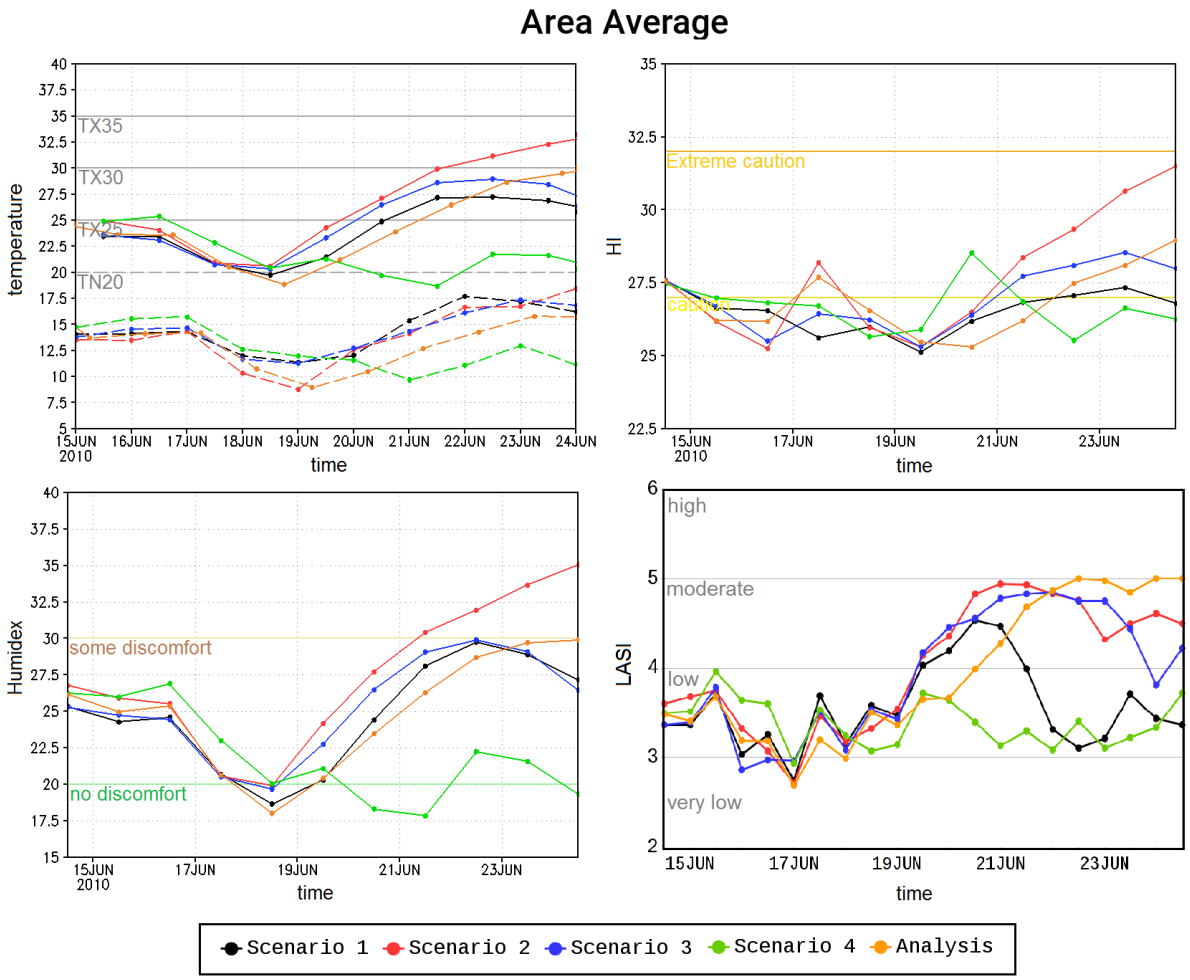

Fig. 3.7.: Time series (left, top) of 2 m minimum temperature at nighttime (long dashed) and 2 m maximum temperature in the daytime (solid), (right, top) of HI and (left, bottom) of Humidex in the daytime averaged over an area from 35-55°E and from 50-60°N as well as (right, bottom) of LASI averaged over an area from 37-49°E and from 51-57°N. Colors mark the different scenarios for blocking onset. Horizontal lines show impact relevant thresholds (for the temperature extremes: TN20 stands for *tropical night*, TX25 for *summer day*, TX30 for *hot day*, TX35 for *extremely hot day*). Figure and caption adopted from Quandt et al. (2017). ©American Meteorological Society. Used with permission.

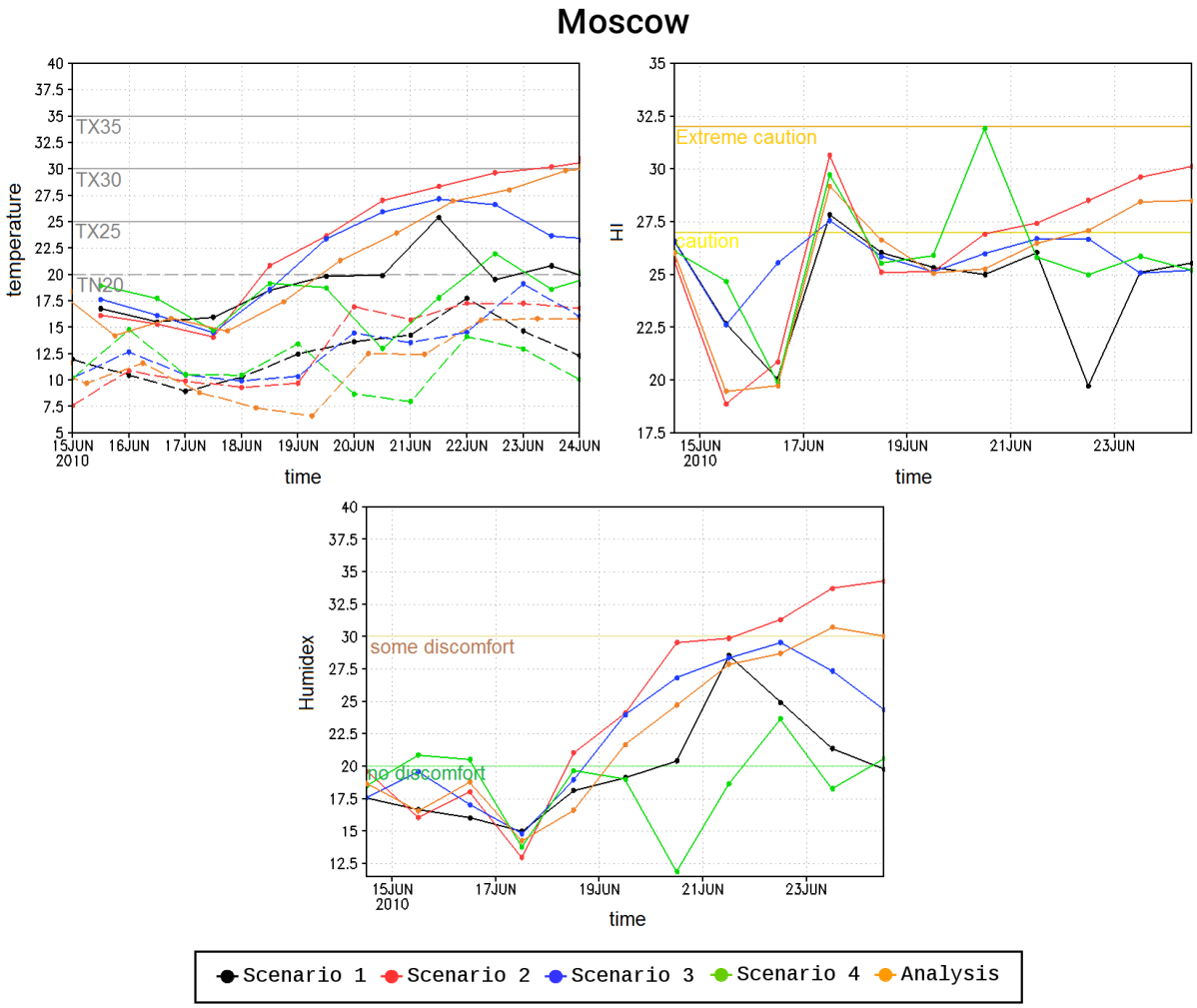

Fig. 3.8.: Time series (left, top) of 2 m minimum temperature at nighttime (long dashed) and 2 m maximum temperature in the daytime (solid), (right, top) of HI and (bottom) of Humidex in the daytime for Moscow. Colors mark the different scenarios for blocking onset. Horizontal lines show impact relevant thresholds (for the temperature extremes: TN20 stands for *tropical night*, TX25 for *summer day*, TX30 for *hot day*, TX35 for *extremely hot day*). Please note that for HI and Humidex, the range of the ordinate of Fig. 3.7 is different. Figure and caption adopted from Quandt et al. (2017). ©American Meteorological Society. Used with permission.

in the analysis. Scenario 2 agreed best with the analysis mean, although the *caution* level was reached two days too early. In scenario 4, this increase was too fast, so that even the *extreme caution* level was reached, followed by a large decrease. The HI values in scenario 3 remained under the *caution* level. For the Humidex, also scenario 2 fit best to the analysis mean. The threshold for *some discomfort* was reached two days before it was reached in the analysis mean. Using a spatial average over a larger area (as described above, Fig. 3.7), the shape of the Humidex curves were quite similar. For Moscow, the heat indices and the temperatures were lower, compared to the spatial mean, since there, high temperatures of surrounding areas were also considered. Moreover, the spread between the scenarios and the amplitude of the fluctuations were larger in the grid point investigation, indicating a challenge for accurate predictions on surface conditions over Moscow.
In summary, in the analysis the onset of the heat wave could be identified with the mentioned heat indices and temperature thresholds. In the scenarios with blocking (scenario 1 to 3), the heat wave evolution was also visible, however, different in its amplification between the scenarios. In the scenario without blocking (scenario 4), there was no temperature increase which could be related to the evolution of a heat wave.

Dynamical Processes Responsible for the Forecast Variability

To investigate the dynamical processes that may have led to the forecast variability, discussed previously, we used an ensemble sensitivity analysis. The method is formally valid for linear evolutions, but the consistency between sensitivities and the synoptic patterns over a six day period confirms its applicability for analyzing the nonlinear evolution, as discussed by Chang et al. (2013). Below, the temporal evolution of the sensitivities in the 500 hPa geopotential field is presented. Then, special features (jet displacement, diabatic feedback) are shown. The times which are shown correspond to the metric time (being equal to the clustering time), which was 0000 UTC 22 June 2010.
The metric (corresponding to a peak in the 500 hPa geopotential height) was positively correlated to a ridge in the geopotential height field at 40°E at -12 hours (Figure 3.9). This mirrored the suitability of the metric to represent the block. The ridge signal formed already at -60 hours and intensified continuously. A negative sensitivity was located in the upstream trough of the blocking ridge (between 0° and 30°E). It developed at -96 hours. The positive and negative sensitivity formed a dipole, reflecting the pattern of a ridge-trough couplet. Downstream and upstream, there were additional positive sensitivities, showing a correlation of the metric (corresponding to the block) to ridges at 50°W and 90°E. The former was located at high latitudes (from 70°N into the polar region) and intensified between -96 and -60 hours, but then rapidly lost intensity. The latter was visible for the whole period with a peak intensity at -72 hours. Overall, the sensitivity patterns showed that the block's amplitude was correlated to the amplification of a trough upstream near 20°E (being part of the blocking system) as well as to the amplification of upstream (30°W) and downstream (90°E) ridges. These ridges might be interpreted as precursor blocks (section 2.2.4), which decelerated the flow, favored the meridional transport of low PV air and hence

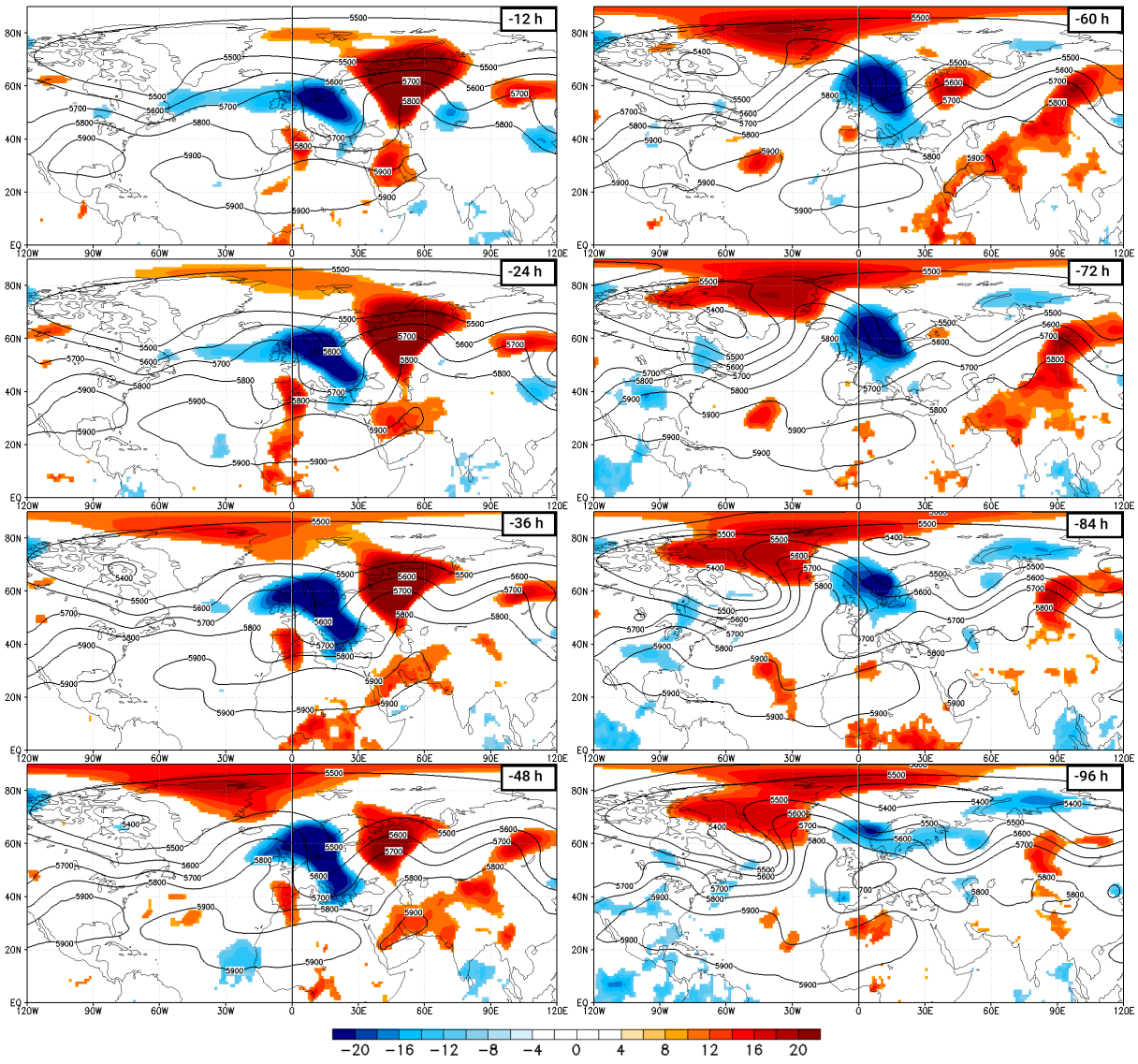

Fig. 3.9.: Statistically significant sensitivity (shading in gpm) of peak in 500 hPa geopotential height (metric representing block's amplitude during the onset phase) at 0000 UTC 22 June 2010 (being the metric time) to the 500 hPa geopotential height at (from top to bottom, left column) -12, -24, -36, -48, (right column) -60, -72, -84, and -96 hours before metric time, plus corresponding ensemble mean of 500 hPa geopotential height (contours in gpm).

created conditions which helped the ridge at 40°E to become stationary and develop into a block. We verified their blocking character with the help of Hovmoeller plots of the blocking index of Tibaldi and Molteni (1990) (not shown). The described sensitivity patterns could also be found in other fields, for example the surface pressure (not shown), corroborating the conclusions drawn from the investigation of the 500 hPa geopotential height sensitivities. The coherency in time and space of the evolution if the sensitivity fields with the synoptic-scale development of the blocking system over a four day period confirms that the ESA can be used to investigate the relevant dynamical processes that caused the forecast variability of the block.

In the following, we will focus on important times to further discuss relevant processes. A series of positive and negative sensitivities in the 200 hPa horizontal wind speed extended from 90°W/80°N to 60°E/20°N (Figure 3.10). The positive sensitivities indicated that an increase in the upper-level wind speed was favorable for the blocking, while the negative sensitivities showed that a decrease was favorable. The positive signals between 90°W and 20°E around 80°N together with the negative signal at 20°W/60°N were connected to the upstream precursor block that was discussed before in the 500 hPa geopotential height field (Figure 3.9), meaning that the amplification of this precursor block (supporting the amplification of the Russian heat wave block) was connected to a poleward displacement of the jet. The sensitivity pattern to the east of 0° were connected directly to the main block. A large positive sensitivity, being in between negative signals at 20°E/60°N and 40°E/50°N, originated at 0°/40°N and meandered to 60°E/70°N. Two smaller positive sensitivities were at 30°E/40°N and 50°E/40°N. The pathway of the positive sensitivities showed two branches of high wind speed, a southern and a northern one, which split at 30°E/40°N. This pattern of sensitivities can be interpreted as jet splitting that is known to be apparent during blocking episodes (e.g. Rex, 1950). The series of increasing and decreasing wind speeds also reflected the strengthening of the gradient northwest and southeast of the wind maxima between 0° and 60°E (corresponding to the large meandering positive sensitivity). The strengthening of the gradient strengthened the upstream trough (seen in Fig. 3.9 at 20°W as negative sensitivity) and the blocking ridge itself.

Diabatic forcing was also of relevance for the development of the block. At -96 hours, positive sensitivities for atmospheric rivers were found along the US East Coast and towards Greenland (Figure 3.11). This AR elongated along the western side of a subtropical anticyclone (seen in the 500 hPa geopotential height ensemble mean in Fig.3.9). The negative AR sensitivities could be interpreted as positions of the AR being unfavorable for the blocking evolution over Europe. Hence, the positive and negative AR sensitivities had to be considered in common, reflecting how the AR could be shifted to be unfavorable or favorable for the block. In addition to a description of a favorable or an unfavorable position of the AR, positive sensitivities also reflected an intensified moist air transport, while negative sensitivities showed where drier conditions were favorable for the blocking evolution. Thus, these sensitivities addressed the position and the intensity of ARs. In vicinity of the positive AR sensitivities, also precipitation areas with positive correlation to the block could be found. The negative precipitation sensitivities in the

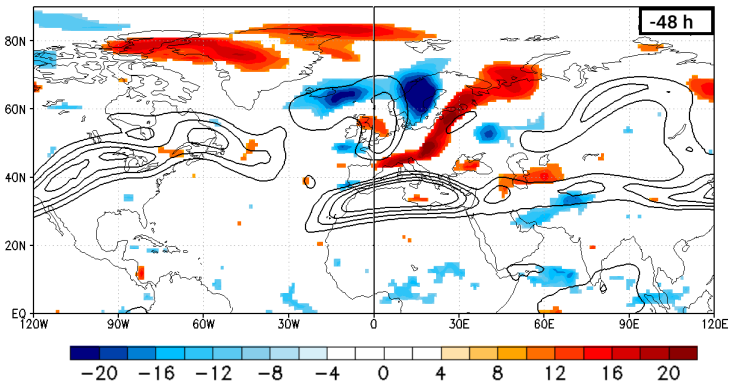

Fig. 3.10.: Statistically significant sensitivity (shading in gpm) of peak in 500 hPa geopotential height (metric representing block's amplitude during the onset phase) at 0000 UTC 22 June 2010 (being the metric time) to the 200 hPa horizontal wind speed at -48 hours before metric time, plus corresponding ensemble mean of 200 hPa horizontal wind speed (contours in ms^{-1}) .

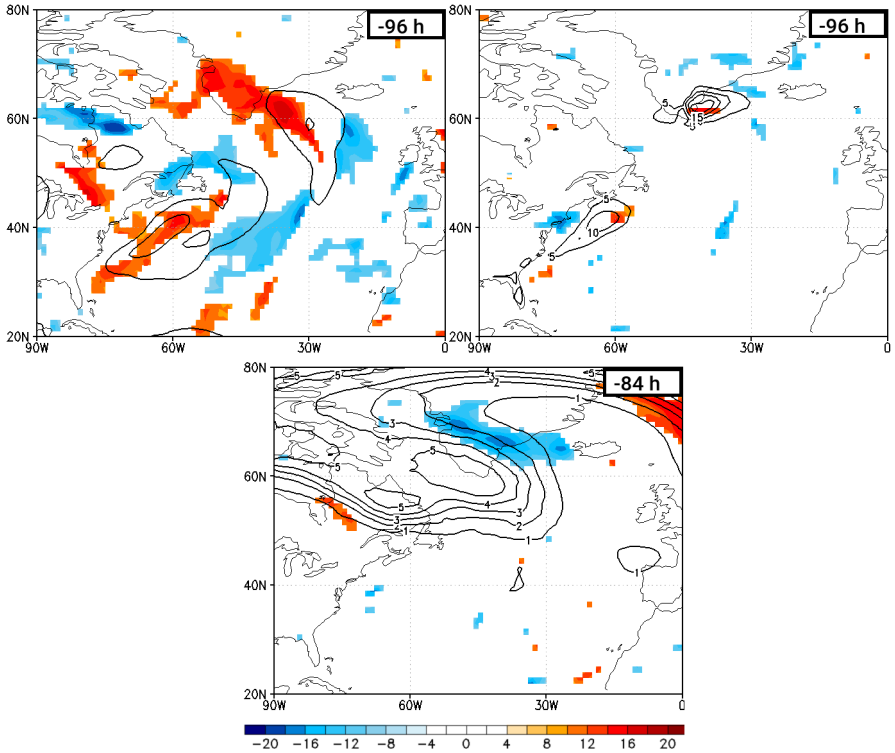

Fig. 3.11.: Statistically significant sensitivity (shading in gpm) of peak in 500 hPa geopotential height (metric representing block's amplitude during the onset phase) at 0000 UTC 22 June 2010 (being the metric time) to (top, left) the vertically integrated water vapor transport (corresponding to AR) and to (top, right) the 12 hourly accumulated precipitation at -96 hours as well as to (bottom) the PV at 320 K at -84 hours before metric time. Corresponding ensemble means in contours (for AR in kg m^{-1} s^{-1}, for precipitation in mm and for PV in PVU).

surrounding areas, which had a more scattered appearance showed areas where less precipitation (drier conditions) could be favorable for the block. 12 hours later, a negative sensitivity became apparent in the PV field, showing that a decrease in PV within the upper-level ridge is favorable for the blocking. These aspects can be brought together. The ARs transported water vapor. Near the coast (either east of the US or Greenland), they were forced to ascend. The water vapor condensed and fell out as rain (see mean precipitation in Fig.3.11). Due to diabatic heating, a negative PV anomaly was produced at upper levels and transported with the upper-level flow, which might have contributed to the amplified ridge at 30°W. The influence of orographically induced cloud-diabatic processes at the south-eastern coast of Greenland on North Atlantic blocks was already found and investigated by Schwierz (2001).

Something similar could be found at -60 hours over Central Europe (Figure 3.12). Along 30°E, a positive sensitivity to an AR was visible. The ensemble mean of the AR was weak here as smoothing effect from averaging. In this area, also a positive correlation between precipitation and the block could be found. Again, it was indicated that the AR provided water vapor, which ascended and fell out as rain, resulting in a PV reduction above. Since at upper levels, positive and negative PV anomalies were already there before -60 hours, we hypothesize that the negative PV anomaly was not created, but strengthened by diabatic forcing from the ARs. Both the positive and negative PV anomaly were predominantly adiabatic due to a zonal shift in the wave pattern (Figure 3.12, bottom). In Figure 3.12 (top, right), additional precipitation sensitivities could be found at 60°N. In the ensemble mean, no precipitation areas were visible, since they were smoothed out by averaging. In certain ensemble members, precipitation areas were located close to, or even at the same place as the precipitation sensitivities (not shown). The positive sensitivity (reflecting a larger amount of precipitation to be favorable for the block) was connected to low surface pressure and an upper level trough (being the block's western flank), and the negative sensitivity (reflecting less precipitation to be favorable for the block) was related to high surface pressure and an upper level ridge (being the block itself). Thus, these precipitation sensitivities reflected the blocking wave pattern (see Fig.3.9). The precipitation over Scandinavia (corresponding to the positive sensitivity at 60°N), which could be enhanced additionally by orography, could also lead to a reduction of upper-level PV at that location. This negative PV anomaly could have been advected within the next 12 hours downstream, having a direct impact on the amplification of the block.

In summary, the results of the ESA suggested that the onset of the block was supported by the appearance of two precursor blocks, downstream as well as upstream. They created favorable flow conditions for the block over Russia. Moreover, the block was supported by diabatic processes creating negative PV anomalies at the upper troposphere. One of them was an indirect trigger, since it supported the North Atlantic precursor block.

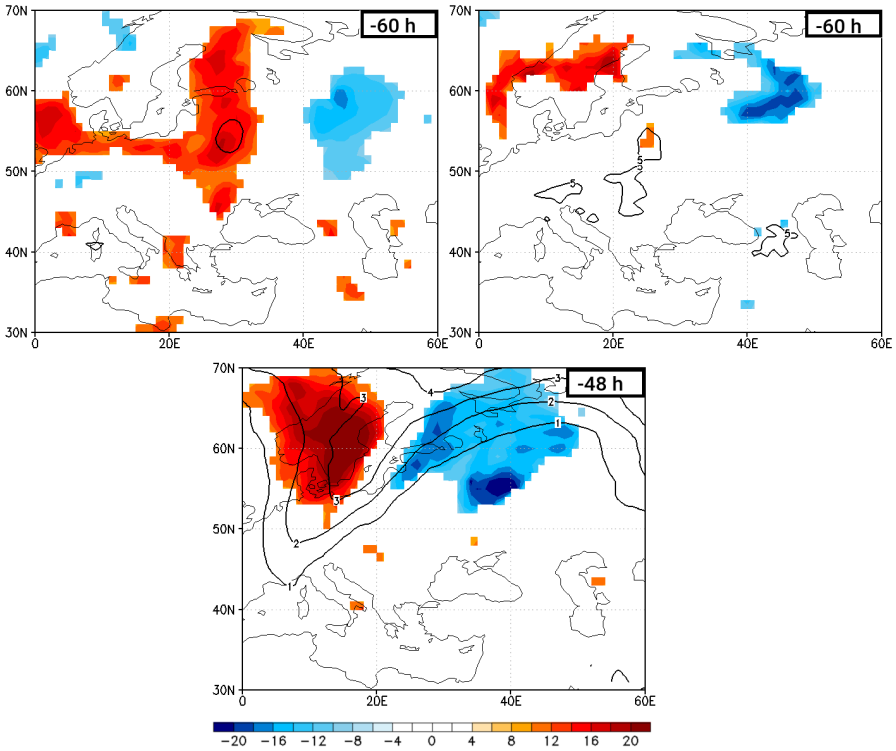

Fig. 3.12.: Statistically significant sensitivity (shading in gpm) of peak in 500 hPa geopotential height (metric representing block's amplitude during the onset phase) at 0000 UTC 22 June 2010 (being the metric time) to (top, left) the vertically integrated water vapor transport (corresponding to AR) and to (top, right) the 12 hourly accumulated precipitation at -60 hours as well as to (bottom) the PV at 320 K at -48 hours before metric time. Corresponding ensemble means in contours (for AR in kg m^{-1} s^{-1}, for precipitation in mm and for PV in PVU).

3.4.2. Forecast Variability during the Mature Stage of the Block

Selection and Characteristics of Forecast Scenarios

The forecast variability was investigated with the help of the first two EOFs at 1200 UTC 31 July 2010. EOF 1 represented 21.4 % of the total variability (Figure 3.13, left, top). Highest values of EOF 1 were distributed north of the block between 70°N and 90°N, capturing variability in the amplitude of the blocking ridge (around 50°E). There was also a negative signal at 100°E. Furthermore, EOF 1 showed a meridional dipole with negative values in the north and positive values in the south within the trough around 10°E. This signal could be interpreted as variability in the amplitude of the trough upstream of the blocking ridge, forming the block's western flank. A member with positive contribution to EOF 1 forecast the blocking ridge to be more amplified than the ensemble mean. In this member, the western flank of the block was tilted to the south-west, and the blocking ridge itself also showed an overturning structure at 20°E/70°N. A member with a negative contribution to EOF 1 forecast the blocking ridge to be less amplified and the trough around 0° less tilted. Moreover, in a negatively contributing member, there was a shortwave trough around 30°E.

The second strongest variability (20.2 %), represented by EOF 2, appeared as strong dipole with negative values to the west of the block and positive values to the east (Figure 3.13, left, bottom). This pattern mirrored the variability in the zonal position and tilt of the ridge. A member contributing positively to EOF 2 forecast the blocking ridge with a north-east tilt. In a member contributing negatively to EOF 2, the blocking ridge was tilted to the north-west. Additionally, in such a member, there was a cut-off low at 20°E.

Here, the 3 clusters-solution was most suitable (Table 3.1). Every EPS contained all of the three scenarios (Figure 3.13, right). Members of the ECMWF ensemble were mostly part of cluster 3, thus, the corresponding scenario was in a sense dominant in this ensemble. The UKMO ensemble had the equivalent number of members in cluster 2 and 3, whereas only one member was part of cluster 1. Thus, the scenario of cluster 1 was not very probable considering the UKMO EPS only. Members of the NCEP ensemble were mostly part of cluster 1, meaning that the scenario of cluster 1 was dominating the NCEP ensemble forecast. Thus, the use of TIGGE gave a different probability for the clusters than the individual EPS did. The analysis members were closest to the center of cluster 3. Given the number of members, this scenario was the most probable one in this ensemble forecast.

Main Development Scenarios for the Mature Stage

At 1200 UTC 2 August (+168 hours forecast), the amplitude of the blocking ridge was forecast similarly in all scenarios (Fig. 3.14), indicating a high predictability of the block itself during mid-July and early August. However, the block's western flank (0°-20°E) differed strongly between the scenarios. In scenario 1, the trough was tilted to the southeast and was less elongated to the south, compared to scenario 2

and 3. In scenario 2, the trough axis had no remarkable tilt, but its zonal extension was largest. A cut-off of the trough occurred in scenario 3. Here, the trough axis was tilted to the southwest. Moreover, the western flank was positioned farther west in comparison to scenario 1 and 2, leading to a more zonally extended blocking complex. Thus, the variability of the block's western flank was clearly visible in this forecast at the mature stage of the block. The differences in the representation of the surface pressure below the western side of the blocking ridge (around 30°E) were also noticeable. The pressure values varied by 10 hPa.

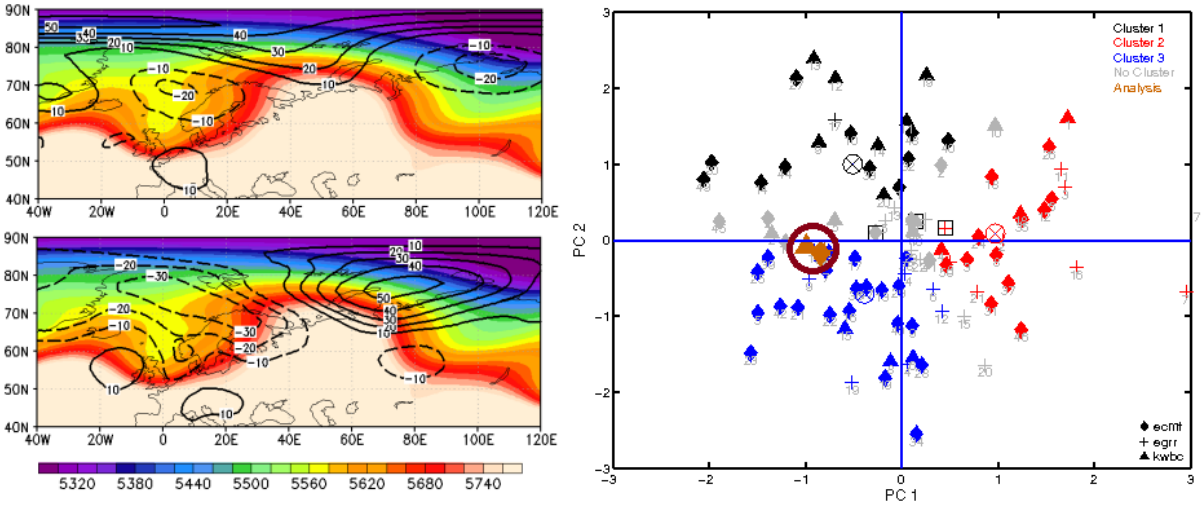

Fig. 3.13.: (left) Ensemble mean of the 500 hPa geopotential height (shaded, in gpm) and distribution of (top) EOF 1 and (bottom) EOF 2 (contours, in gpm) for mature stage forecast at +120 hours (at 1200 UTC 31 July 2010). The first and second principle component (PC) for the three-cluster solution based on EOFs from TIGGE ensemble members (forecast initialized 1200 UTC 26 July 2010) at +120 hours (1200 UTC 31 July 2010). Symbols show the EPS membership (rhombus for ECMWF, triangle for NCEP, and cross for UKMO) and colors the cluster membership. Cluster centers are defined by the circled cross. The analysis members are additionally circled in dark red. Figures and caption adopted from Quandt et al. (2017). ©American Meteorological Society. Used with permission.

Forecast Variability of impact-related Parameters

For the mature stage, we investigated the impact of the variability of the blocking anticyclone on the heat intensity, and of the block's western flank on precipitation. We compared the forecast precipitation with the first guess daily analysis data from the GPCC (section 3.2). The reports on high impact weather events were taken from the European Severe Weather Database (ESWD; Dotzek et al., 2009).

At 1200 UTC 2 August 2010, temperatures over Russia varied between the scenarios (Fig. 3.15). In the analysis, Moscow and especially southern regions had temperatures over 30°C. There, the HI and the

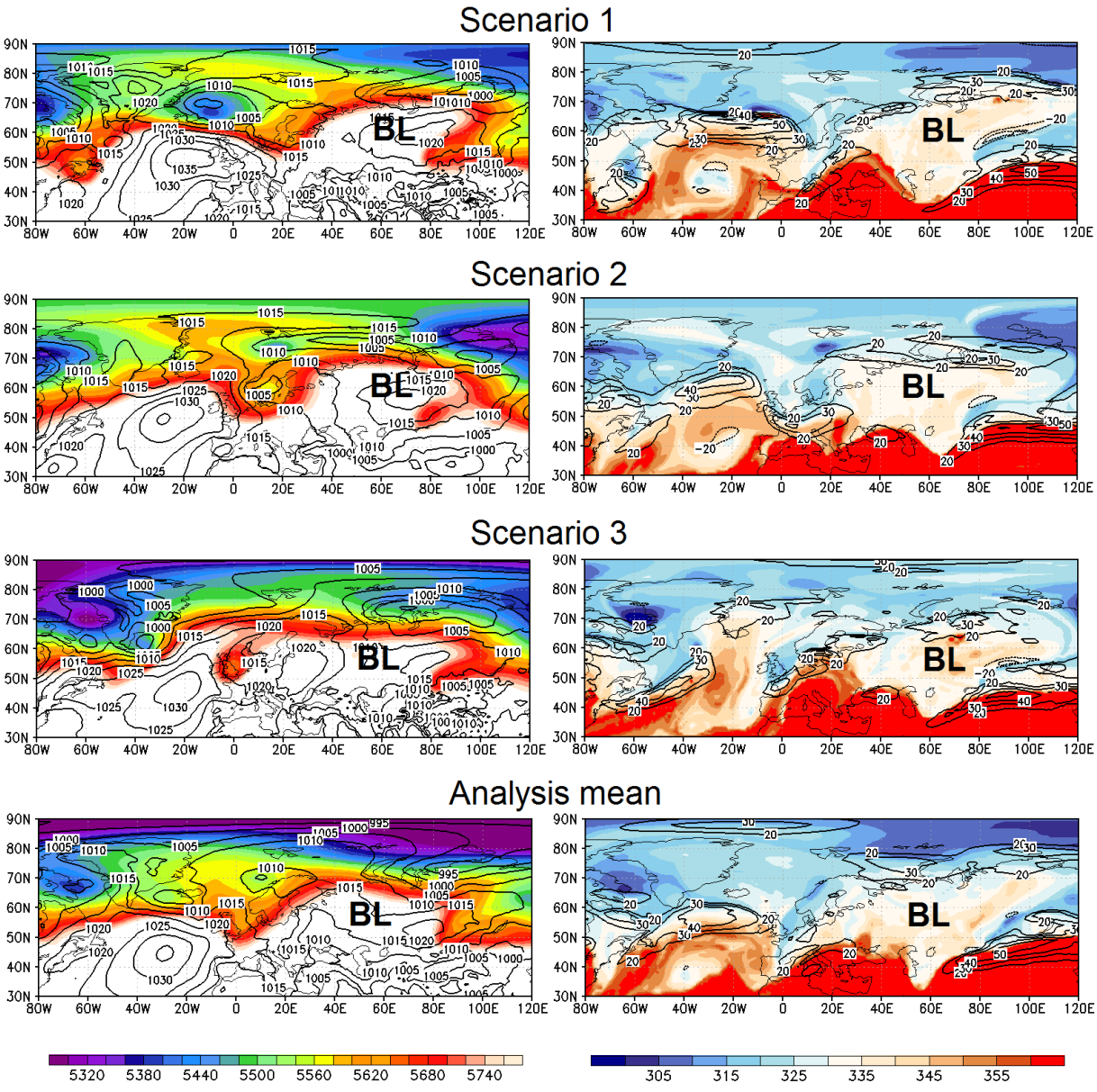

Fig. 3.14.: (left) 500 hPa geopotential height (shaded, in gpm) and mean sea level pressure (contours, in hPa), (right) potential temperature at 2 PVU (shaded, in K) and 300 hPa zonal wind (contours, in m s^{-1}) at +168 hours (1200 UTC 2 August 2010) for the three forecast main scenarios and the analysis mean for the mature stage of the block. BL marks the blocking system. Figure and caption adopted from Quandt et al. (2017). ©American Meteorological Society. Used with permission.

Humidex reached their second warning levels (corresponding to *extreme caution* and *some discomfort*). In scenario 1, temperatures exceeded 30°C in Moscow and the surrounding area. For Moscow itself, the HI indicated *caution*. The Humidex level *some discomfort* was reached in the area surrounding Moscow. In scenario 2, temperatures over 35°C and HI values indicating *extreme caution* extended farther north and affected a larger area. In scenario 3, Moscow did not experience extreme temperatures, only south-eastern areas were affected. By comparing all three scenarios, it could be seen that the western side of the heat affected area (in terms of 2 m temperature, HI and Humidex distribution) had a higher variability than the eastern one. We hypothesize that this was directly linked to the variability of the western flank of the blocking complex. A comparison revealed that the heat distribution in scenario 1 was closest to the analysis, whereas it was overestimated in scenario 2 and underestimated in scenario 3.
Substantial differences in the precipitation field over Europe can be seen in Fig. 3.16. In the analysis, one precipitation area spread from 0°/45°N to 20°E/55°N and another one was located over Scandinavia. This agrees with the reports of ten heavy rain events and four large hail events in Europe on 2 August 2010 (ESWD). Most of these events occurred in Austria. In scenario 1, it rained in areas around the Gulf of Venice and from 20°E/50°N to 35°E/65°N. In both precipitation areas, amounts over 30 mm were reached. In scenario 2, it rained in Austria, Croatia, Slovenia and Hungary. Another difference to scenario 1 was the precipitation center over Scandinavia. In scenario 3, strongest precipitation was found in Germany, France and Scandinavia. Here, a larger area was affected by rain amounts over 30 mm, in comparison to scenario 1 and 2. Another precipitation center could be found over Great Britain. The position of the western flank of the block was closely linked to the precipitation distribution, since in all scenarios, the rain bands were located ahead of the western trough of the block and the smaller precipitation centers underneath the trough. Compared to the first guess daily analysis, the precipitation amount was overestimated and the position of the rain band was displaced in all forecast scenarios.

Dynamical Processes Responsible for the Forecast Variability

In the following, we investigate the results from ESA, to evaluate which dynamical processes were responsible for the variability of the block's western flank during the mature stage. After showing a time series of the 500 hPa geopotential height sensitivities, special features are presented. The time lags refer to the metric time (1200 UTC 31 July 2010).
At -12 hours, around 0°, a dipole of negative and positive sensitivities was visible within a trough (Figure 3.17). This pattern reflected the metric. An increase in the metric was correlated to a stronger trough farther east (corresponding to an increase in the geopotential height between 0° and 30°W and a decrease between 0° and 20°E). A decrease in the metric was correlated to a stronger trough farther west (corresponding to a decrease in the geopotential height between 0° and 30°W and an increase between 0° and 20°E). The dipole was visible for the whole investigation period (from -72 to -12 hours), whereas it followed a clockwise rotation. Thus, at the beginning (-72 hours) the negative sensitivity was north

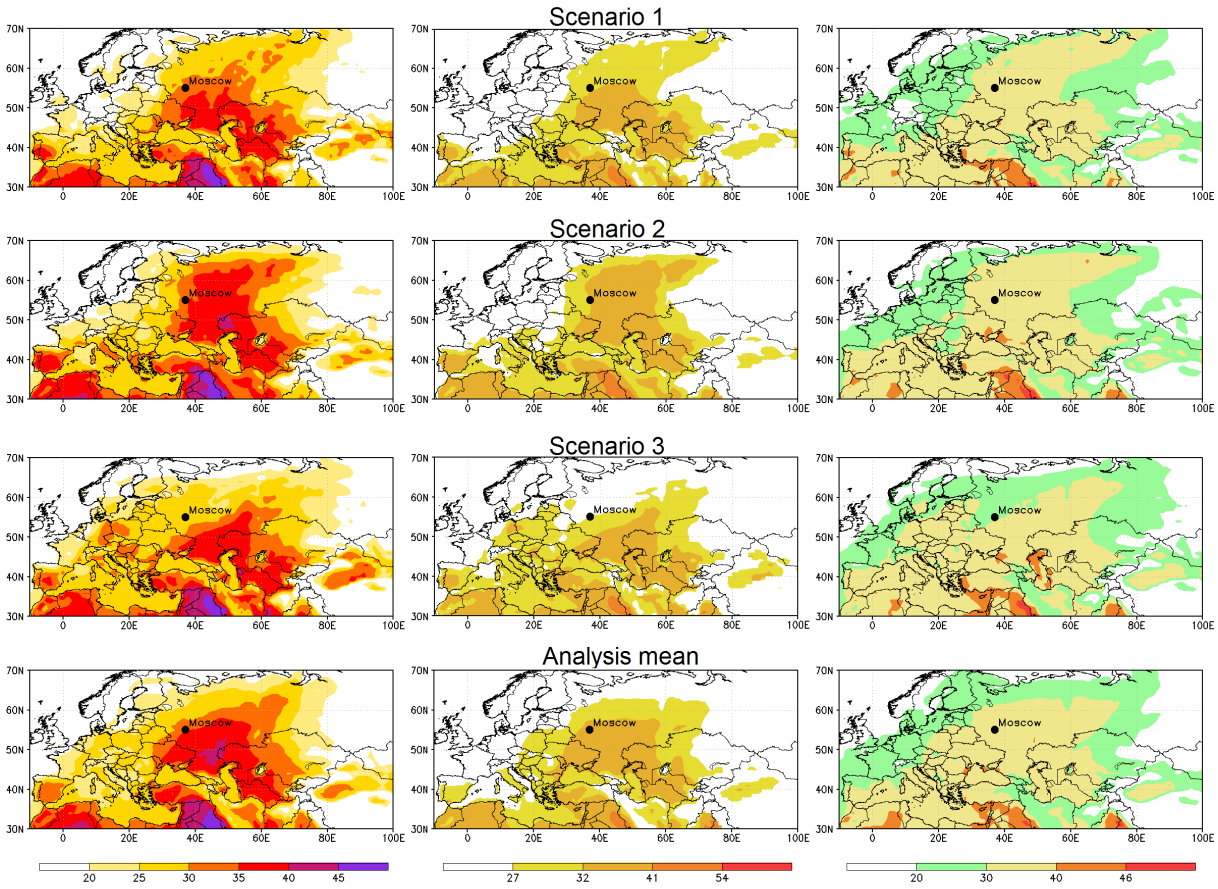

Fig. 3.15.: (left) 2 m temperature, (middle) HI and (right) Humidex (all in °C) at +168 hours (1200 UTC 2 August 2010) for the four main forecast scenarios and the analysis mean for the mature stage of the block. Figure and caption adopted from Quandt et al. (2017). ©American Meteorological Society. Used with permission.

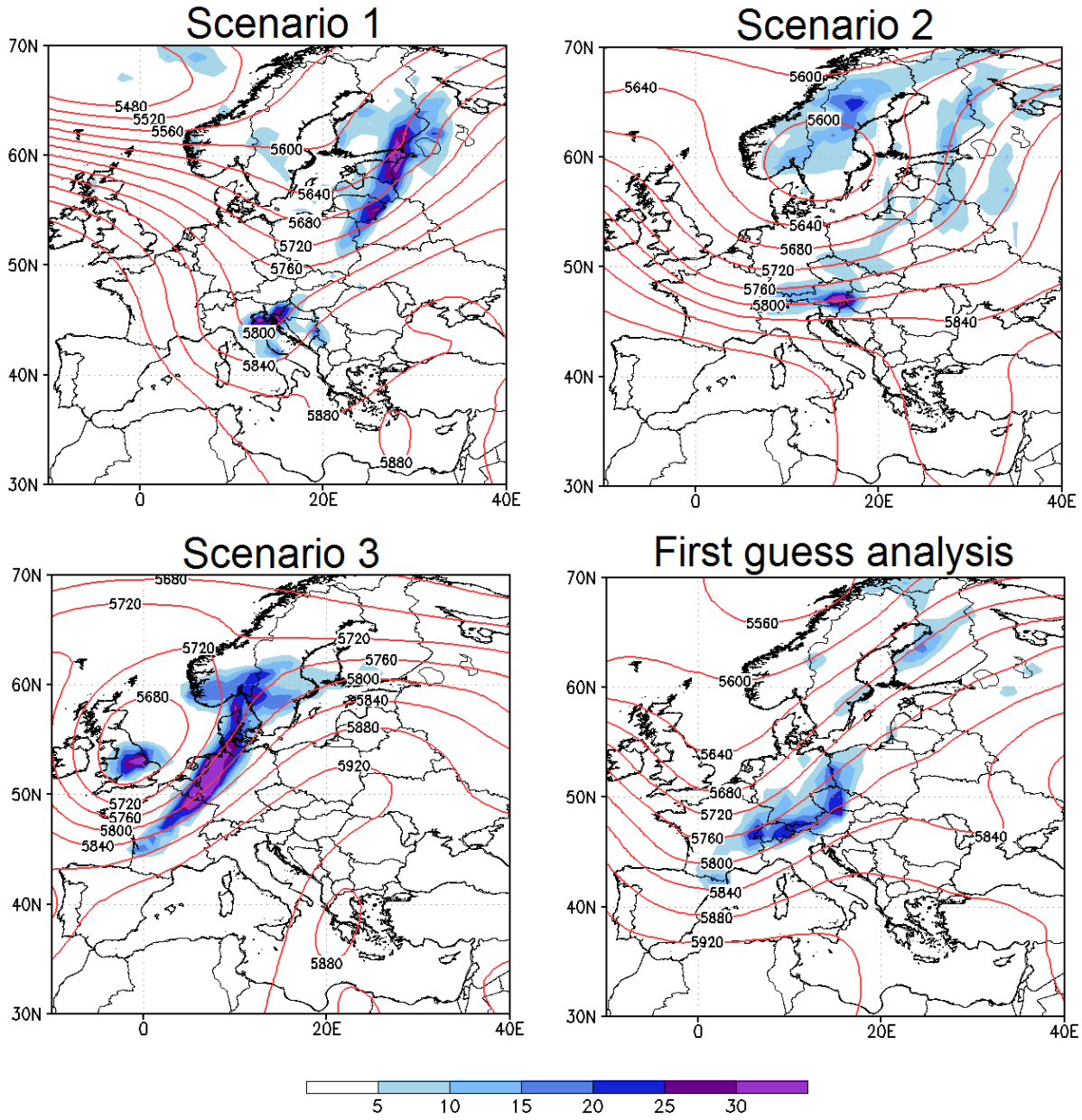

Fig. 3.16.: Accumulated surface total precipitation (shaded, in mm) and the daily mean of the 500 hPa geopotential height (red contours, in gpm) for 2 August for the three main scenarios for the mature stage of the block. At the bottom on the right-hand side, the daily mean of the 500 hPa geopotential height of the analysis mean and the total precipitation from the GPCC first guess daily analysis, also for 2 August. Figure and caption adopted from Quandt et al. (2017). ©American Meteorological Society. Used with permission.

of the positive one (around 30°W), and in the end (-12 hours), the negative one was placed westward of the positive one (around 0°). The positive part of the north-south oriented dipole at -72 hours was ahead of a trough (at 50°W) and the negative part was at the apex of a ridge (at 30°W). The metric increased if the trough weakened and/or the ridge was strengthened, and the metric decreased if the trough was strengthened and/or the ridge was weakened. In the investigated time period, the pattern was related to an amplification of the ridge-trough couplet (around 40°W) at -72 hours, while it was related to a zonal shift of the trough (around 0°) at -12 hours. Besides these sensitivities, additional positive sensitivities could be found in upstream and downstream regions. Upstream (at 70°W), the positive sensitivity was within a trough, meaning that an increase in the geopotential height (weakening the trough) led to an increase in the metric (related to CWB or an eastward shift of the block's western flank), while a decrease in the geopotential height (strengthening the trough) led to a decrease in the metric (related to AWB or a westward shift of the block's western flank). This positive sensitivity signal developed already at -72 hours and propagated eastward. This context is discussed in more detail below. First, the second downstream signal is analyzed. A north-south oriented dipole with positive values in the north and negative values in the south was located within the blocking ridge. The positive sensitivity was smaller and weaker than the negative one. This pattern was first visible at -24 hours. It shows that the variability of the block's amplitude was related to the variability of its western flank. The positive sensitivity within the blocking ridge was related to an increase in the metric that corresponded to a western flank farther east or cyclonic breaking. Indeed, the negative sensitivity was also within the block, but mainly at the position of shortwave ridges (being visible as dents in the geopotential height isolines at 30°E/60°N and 70°E/60°N) along the blocking ridge. There, the negative sensitivities led to an decrease in the metric (showing the tendency for anticyclonic breaking or a westward shift of the trough upstream). A stronger block had a western flank farther east or breaking cyclonically, while a weaker block was correlated to a western flank farther west or breaking anticyclonically. The presence of shortwave ridges were favorable for a western flank farther west or breaking anticyclonically. Thus, the sensitivity pattern around 50°E represented the correlation of the block's western flank to the shape and the amplitude of the block. In respect of the amplitude, we hypothesize that this correlation was linked to PV advection. The cyclonically breaking trough favored the transport of low PV air from lower latitudes directly to the amplified blocking ridge, leading to a further amplification.

The effect of diabatic forcing can be seen in Figure 3.18. A strong positive and negative sensitivity were located at 40°W between 50°N and 70°N in vicinity of an AR along the US East Coast. A stronger AR towards Greenland increased the metric, while a stronger zonally oriented AR (at 50°N) decreased the metric. The positive sensitivity of the AR coincided with a positive precipitation anomaly, meaning that stronger precipitation at the southern coast of Greenland resulted in an increase of the metric, while less precipitation decreased the metric. Bringing these aspects together, an AR which favored the meridional transport of water vapor was forced to ascend as it reached Greenland. As consequence, precipitation fell out at the coast. This effect was also found to be relevant for the onset phase of the block (section

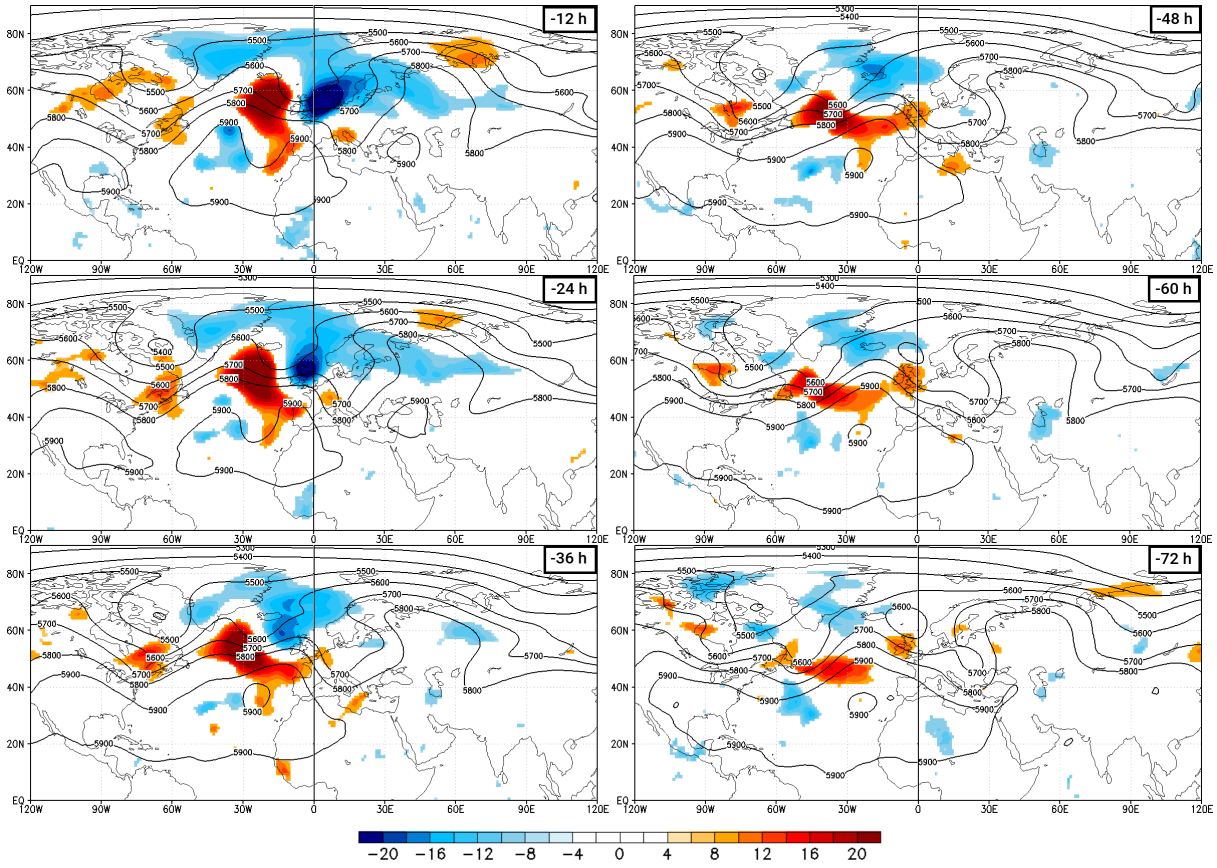

Fig. 3.17.: Statistically significant sensitivity (shading in gpm) of difference of means of two neighboring boxes in 500 hPa geopotential height (metric representing shape and position of block's western flank during the mature stage) at 1200 UTC 31 July 2010 (being the metric time) to the 500 hPa geopotential height at (from top to bottom, left column) -12, -24, -36, (right column) -48, -60, and -72 hours before metric time, plus corresponding ensemble mean of 500 hPa geopotential height (contours in gpm).

3.4.1; Schwierz, 2001). The enhanced low-level moisture transport led to a faster destabilization of the atmosphere, since relatively moister air moved below relatively drier air. This stratification allowed air parcels to ascend, leading to a pressure decrease at the surface (supporting a cyclonic development in the low levels). Thus, more CWB than AWB events are triggered (Riviere and Orlanski, 2007).
Now we go back to the positive sensitivity at 70°W (Figure 3.17). It was also clearly visible in the TE sensitivity pattern, illustrated in Figure 3.19. The positive sensitivity within the negative TE reflected that a stronger negative TE decreases the metric. Thus, this TE was favorable for the anticyclonic breaking of the block's western flank and unfavorable for cyclonic breaking. Storms (belonging to the transient weather systems) are able to influence the direction of wave breaking, since they can trigger a meridional jet displacement (Riviere and Orlanski, 2007). However, we did not find a sensitivity in the 200 hPa horizontal wind speed, pointing to jet displacement, which could be linked to the TE (not shown). Hence, the TE had to influence the block in a different way. Before, we investigated the diabatic processes (Figure 3.18), where we found the appearance of an AR being favorable for CWB of the block's western flank, due to moisture transport. It is possible that the TE (favoring AWB) was fed by moisture from the AR. Consequently, less moisture was available for the further poleward transport, being unfavorable for CWB, since a further destabilization at lower levels in northern areas could not be supported.
In summary, the variability of the block's western flank was influenced to the variability of the block's amplitude. CWB favored advection of low PV air into the ridge, leading to a further intensification of the block itself. Moreover, also diabatic forcing was relevant for the direction of breaking of the block's western flank. An AR transported moisture poleward and favored CWB. TE activity at the US East Coast could interrupt the moisture transport, as it diverted water vapor from the AR. In this way, the TE favored the anticyclonical breaking of the block's western flank.

3.4.3. Forecast Variability during the Decay Phase of the Block

Selection and Characteristics of Forecast Scenarios

The distributions of the first two EOFs reflected the forecast variability of the flow features at +144 forecast hours. The strongest variability, represented by EOF 1 with 25.6 % of the total variability, could be found as dipole along the blocking ridge (Figure 3.13, left, top). Another weaker positive signal of EOF 1 was visible between 40°W and 10°E and between 40°N and 65°N. Thus, EOF 1 described the variability of the amplitude of the shortwave ridges (at 0° and at 70°E) within the longwave blocking ridge (between 20°W and 80°E) and also a meridional shift of the low at 60°E/80°N. In a member with a positive contribution to EOF 1, the block was shifted to the east. Its axis was tilted to north-east. The cut-off low over Central Europe was located farther south compared to the ensemble mean. A member with a negative contribution to EOF 1 forecast the block farther west with a ridge axis tilted to north-west. Here, the cut-off system was placed farther north-west.

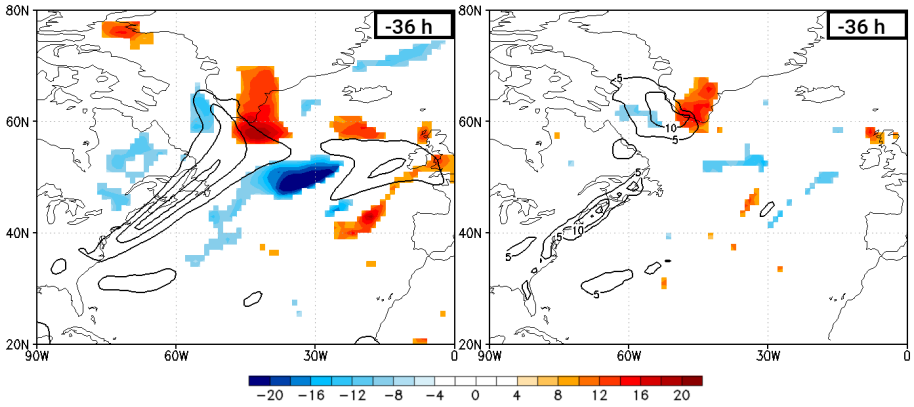

Fig. 3.18.: Statistically significant sensitivity (shading in gpm) of difference of means of two neighboring boxes in 500 hPa geopotential height (metric representing shape and position of block's western flank during the mature stage) at 1200 UTC 31 July 2010 (being the metric time) to (left) the vertically integrated water vapor transport (corresponding to AR) and to (right) the 12 hourly accumulated precipitation at -36 hours. Corresponding ensemble means in contours (for AR in kg m^{-1} s^{-1}, and for precipitation in mm.).

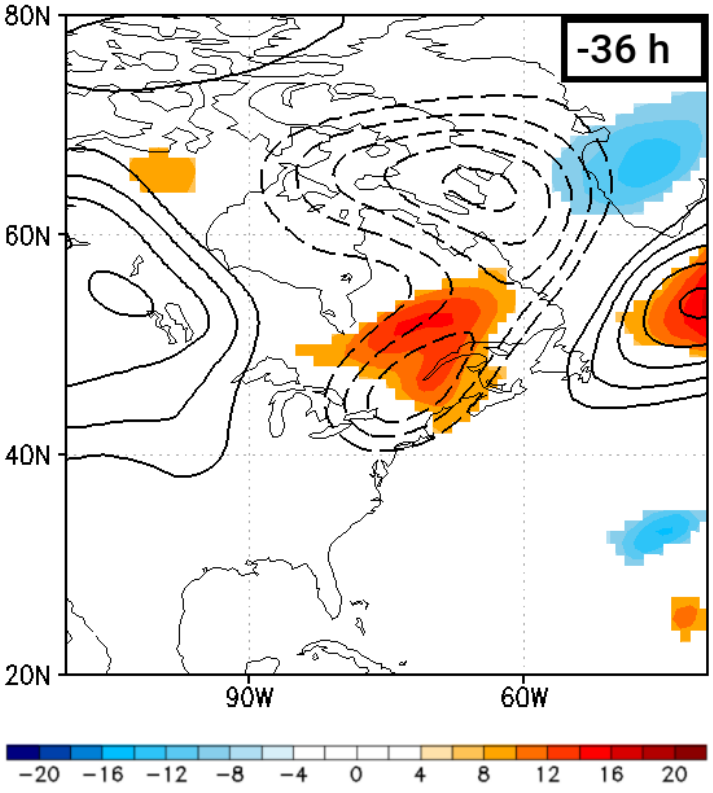

Fig. 3.19.: Statistically significant sensitivity (shading in gpm) of difference of means of two neighboring boxes in 500 hPa geopotential height (metric representing shape and position of block's western flank during the mature stage) at 1200 UTC 31 July 2010 (being the metric time) to TE at -36 hours before metric time, plus corresponding ensemble mean of TE (contours in gpm), where dotted lines show negative and continuous lines positive values.

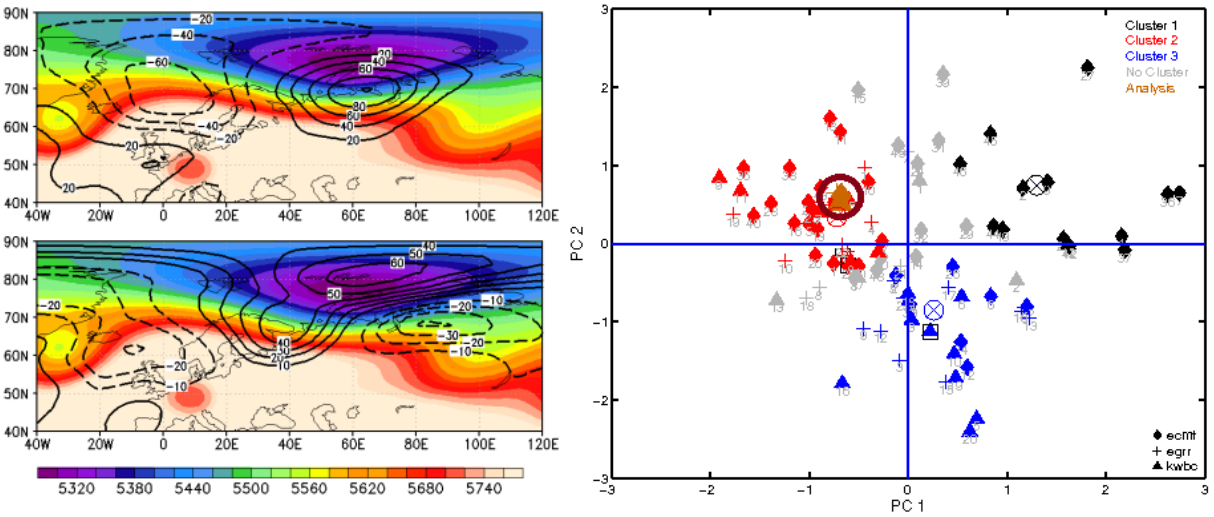

Fig. 3.20.: (left) Ensemble mean of the 500 hPa geopotential height (shaded, in gpm) and distribution of (top) EOF 1 and (bottom) EOF 2 (contours, in gpm) for blocking decay forecast at +144 hours (1200 UTC 16 August 2010). (right) The first and second principle component (PC) for the three-cluster solution based on EOFs from TIGGE ensemble members (forecast initialized 1200 UTC 10 August 2010) at +144 hours (1200 UTC 16 August 2010). Symbols show the EPS membership (rhombus for ECMWF, triangle for NCEP, and cross for UKMO) and colors the cluster membership. Cluster centers are defined by the circled cross. The analysis members are additionally circled in dark red. Figures and caption adopted from Quandt et al. (2017). ©American Meteorological Society. Used with permission.

The second strongest variability (with 16.8 %) was found as pattern with a change from negative to positive and again to negative values along the ridge (Figure 3.13, left, bottom), with the two shortwave ridges being captured by the negative EOFs and the dent in between by positive EOF. Moreover, EOF 2 also represented the variability of an area of low geopotential height northeast of the blocking system. In a member with a positive contribution to EOF 2, no remarkable shortwave troughs passed the blocking ridge. The block appeared as long wave with an enormous zonal extension from 40°W to 90°E. A member which contributed negatively to EOF 2 forecast the block with a dent at 40°E which divided the ridge in two ridges of smaller wavelengths.
The clustering procedure resulted in the 3 clusters-solution (Table 3.1). The members from the three individual EPS were distributed between the clusters as follows (Figure 3.13, right). The ECMWF and the NCEP EPS contributed to all three clusters. In contrast, none of the UKMO members was found in cluster 1. Hence, the UKMO ensemble did not capture the same range of development scenarios as the ECMWF or the NCEP ensemble. The three analysis members were located close to the center of cluster 2, which meant that at clustering time, the 500 hPa geopotential height scenario of cluster 2 closely resembled the analysis. Based on this forecast the occurrence of the scenario represented in clusters 2 and 3 were more probable than the scenario of cluster 1, since most of the members were assigned to cluster 2 and 3.

Main Development Scenarios for the Decay

At 1200 UTC 18 August (+192 hours forecast), the decay of the block was forecast only in scenario 1, while blocking was still identified in scenario 2 and 3. In scenario 1, a deep trough was located between 20°E and 100°E (Fig. 3.21). At 500 hPa, this trough created zonal flow conditions at 60°N between 0° and 60°E. In scenario 3, the blocking ridge broke cyclonically (between 20°W and 40°E). This was different in scenario 2, in which a cut-off system was apparent at 20°E/50°N. In the analysis mean, the low at 60°E was much smaller than in the forecast scenarios. Scenario 1 was most similar to the analysis mean, however, the ensemble members overestimated the extension of the low and the amplitude of the ridge upstream.

Forecast Variability of impact-related Parameters

At 1200 UTC 18 August (+192 hours forecast), the blocking was still identified in scenarios 2 and 3. The surface temperature evolution, as well as the evolution of HI and Humidex were closest to the analysis in scenario 2, despite the fact that in scenario 2, the block was still present while it has already decayed in the analysis (Fig. 3.22). Scenario 1, which had forecast the decay correctly, underestimated the temperature values and thus the heat intensity around Moscow. Hence, for the decay phase, the forecast of

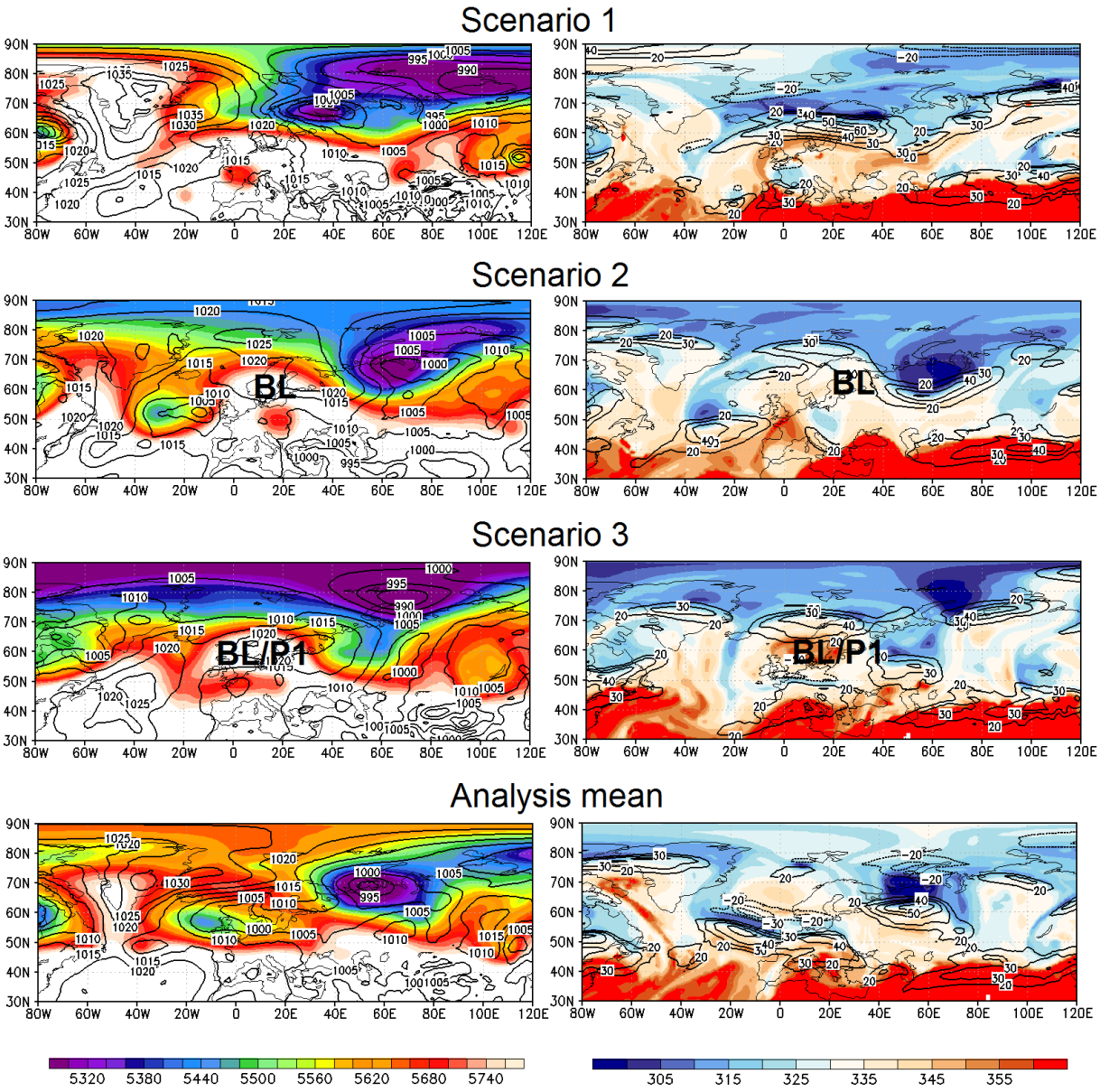

Fig. 3.21.: (left) 500 hPa geopotential height (shaded, in gpm) and mean sea level pressure (contours, in hPa), (right) potential temperature at 2 PVU (shaded, in K) and 300 hPa zonal wind (contours, in m s^{-1}) at +192 hours (1200 UTC 18 August 2010) for the three forecast main scenarios and the analysis mean for blocking decay. BL marks the blocking system. P1 marks the position of poleward cyclonic RWB (Gabriel and Peters, 2008). Figure and caption adopted from Quandt et al. (2017). ©American Meteorological Society. Used with permission.

the heat intensity did not depend on blocking prediction.

This was also visible in the temporal evolution of the minimum and maximum temperature, and of the heat indices and the LASI (Fig. 3.23): In all scenarios, the temperatures, the heat indices, and the LASI decreased with time, independent of whether the decay was forecast or the block remained. On 11 August, the maximum temperature of the short-term forecast corresponded to an *extremely hot day*. Ten days later, the maximum temperature dropped below 25°C. Scenario 1 and 2 captured this trend. In scenario 3, the drop in temperature after 16 August was stronger. The drop in temperature below the *hot day* level occurred later in scenario 1 and 3 than in scenario 2. Scenario 2 agreed with the short-term forecast. In all scenarios, the minimum temperature dropped below the threshold for a *tropical night* after 14 August, in the short-term forecast already after 12 August. After 19 August, HI and Humidex decreased strongly in all scenarios. In scenario 1, the HI fell below the *extreme caution* level too early, compared to the analysis mean, whereas scenario 2 and 3 forecast this decrease too late. For the Humidex, the drop below the *some discomfort* level was forecast too late in all scenarios, whereas scenario 2 was closest to the analysis. According to LASI, the risk for large fires decreased in all scenarios from a *moderate* to *low* level. However, the drop below the *low* fire potential level occurred two days earlier than in the analysis mean. At the end of the forecast time, the LASI in the analysis mean was significantly lower than in the forecast scenarios.

For Moscow, the heat relevant variables decreased over time (Fig. 3.24). Until 15 August, the trend in the maximum temperature was similar in the short-term forecast and the scenarios, except for scenario 2, in which temperature was underestimated. The drop in temperature under 25°C occurred more than two days too early in scenario 3. In scenario 2, the temperatures were higher than 25°C for the whole period; in scenario 1, they were higher than 25°C at least most of the time. The period, during which *tropical nights* were detected, was 3 days longer in scenario 2 and 3, and even 6 days longer in scenario 1, compared to the short-term forecast. HI decreased steadily in the analysis mean. The drop below the *caution* level occurred up to two days earlier than in the analysis, expect for scenario 3, which fell below *extreme caution* one day after the observed decrease in HI. A similar evolution was found for the Humidex (Fig. 3.24).

All scenarios predicted the end of the heat wave, although the blocking system still existed in scenario 2 and 3. Heat waves have a spatial dependence. Thus, a shift of the controlling upper-level wave pattern leads to the end or to an interruption of the heat wave (Stefanon et al., 2012). Interruption means here that a heat wave possibly redevelops, as long as the surface and upper-level weather systems are again favorable. In our scenarios, the blocking system was either dissolved or shifted to the west. Both cases led to the end of the heat wave in the region around Moscow.

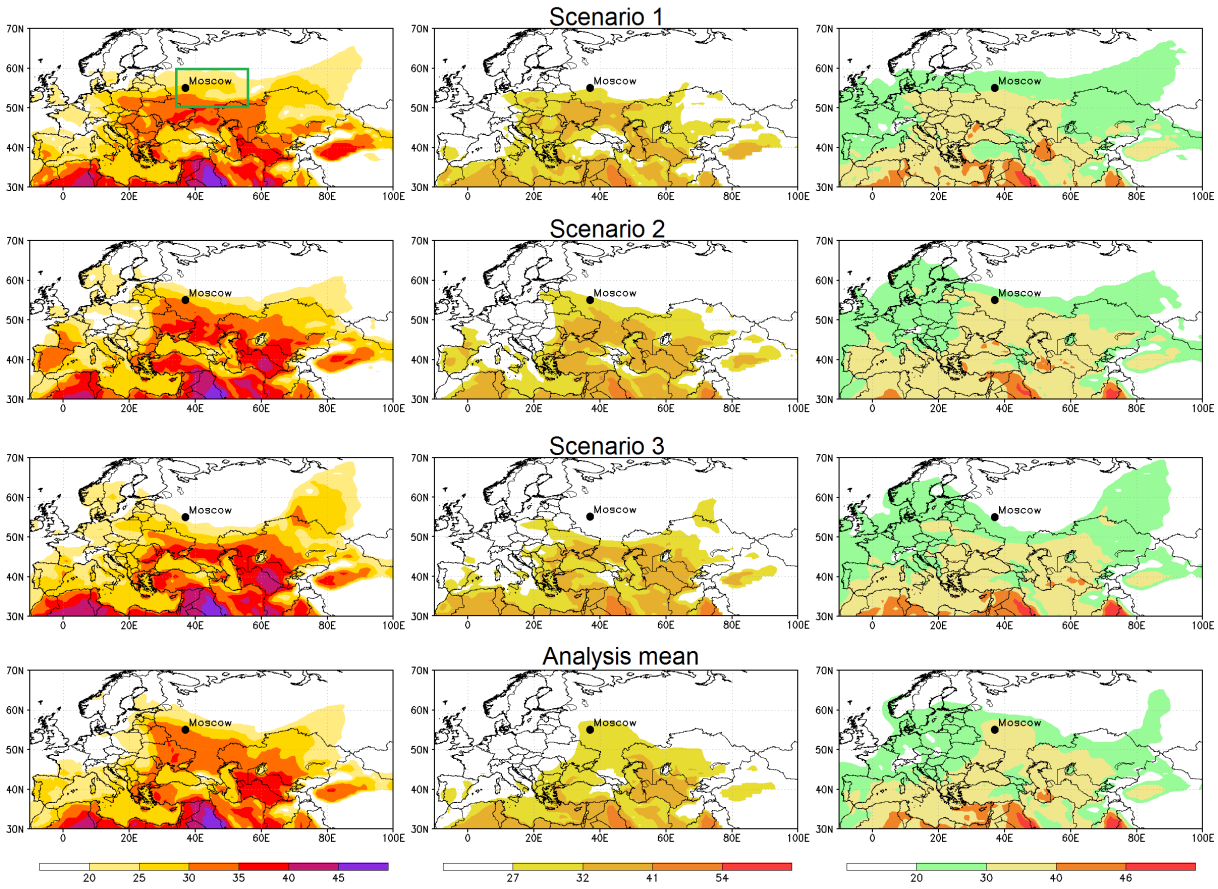

Fig. 3.22.: (left) 2 m temperature, (middle) HI and (right) Humidex (all in °C) at +192 hours (1200 UTC 18 August 2010) for the four main forecast scenarios and the analysis mean for blocking decay. The green box marks the region for which we calculated the averaged temperatures (for Fig. 3.23). Figure and caption adopted from Quandt et al. (2017). ©American Meteorological Society. Used with permission.

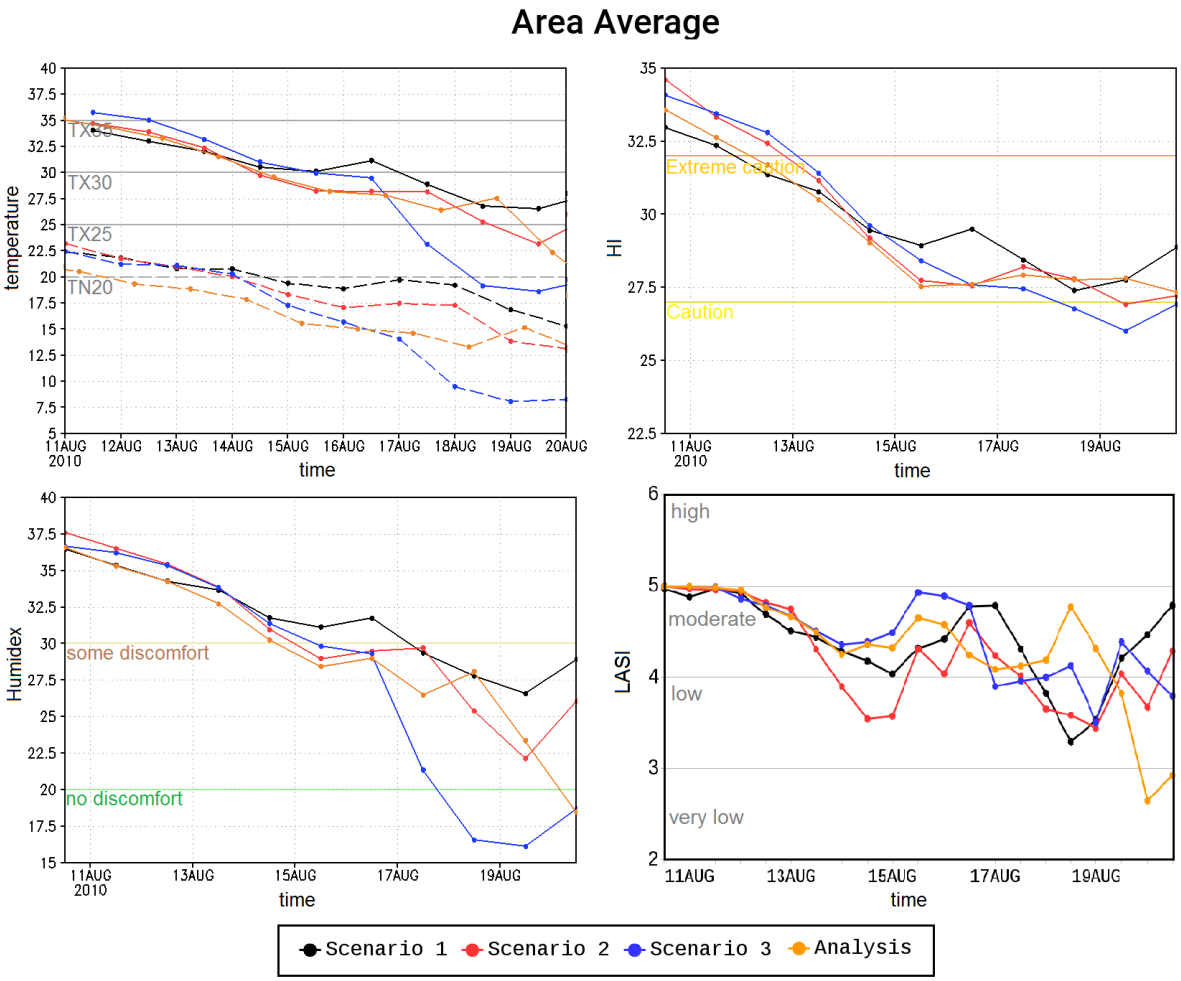

Fig. 3.23.: Time series (left, top) of 2 m minimum temperature at nighttime (long dashed) and 2 m maximum temperature in the daytime (solid), (right, top) of HI and (left, bottom) of Humidex in the daytime averaged over an area from 35-55°E and from 50-60°N as well as (right, bottom) of LASI averaged over an area from 37-49°E and from 51-57°N. Colors mark the different scenarios for blocking decay. Horizontal lines show impact relevant thresholds (for the temperature extremes: TN20 stands for *tropical night*, TX25 for *summer day*, TX30 for *hot day*, TX35 for *extremely hot day*). Figure and caption adopted from Quandt et al. (2017). ©American Meteorological Society. Used with permission.

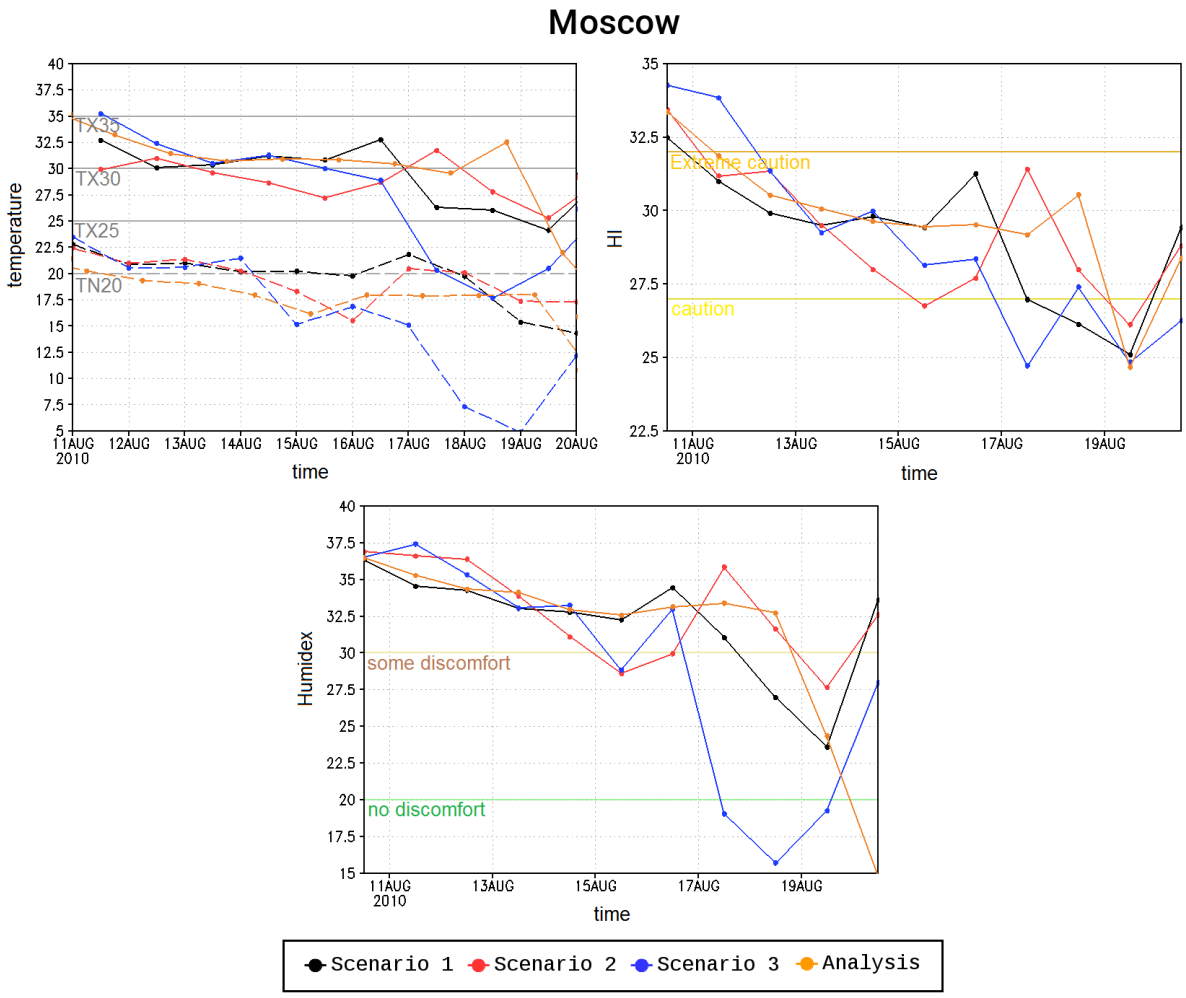

Fig. 3.24.: Time series (left, top) of 2 m minimum temperature at nighttime (long dashed) and 2 m maximum temperature in the daytime (solid), (right, top) of HI and (bottom) of Humidex in the daytime for Moscow. Colors mark the different scenarios for blocking decay. Horizontal lines show impact relevant thresholds (for the temperature extremes: TN20 stands for *tropical night*, TX25 for *summer day*, TX30 for *hot day*, TX35 for *extremely hot day*). Figure and caption adopted from Quandt et al. (2017). ©American Meteorological Society. Used with permission.

Dynamical Processes Responsible for the Forecast Variability

As for the onset phase and the mature stage of the block, we also used ESA to investigate the dynamics responsible for the variability during the decay phase of the block. In the following, the sensitivities for the geopotential height at 500 hPa are shown as a time series. Additional effects of ARs and TEs are also shown at specific times. The times refer to the metric time, being 1200 UTC 16 August 2010.
A positive sensitivity developed around 0°/60°N, coinciding with the blocking ridge (Figure 3.25). It intensified with time and grew in the zonal as well as in the meridional direction. This signal represented the metric used here, which increased with increasing geopotential height and decreased with decreasing geopotential height. Upstream (between 60°N and 80°N), there was a negative sensitivity which evolved at -48 hours. This negative sensitivity coincided with an upper level low, and together with the positive sensitivity formed a dipole within the block. Additional sensitivities were visible downstream and south of the block. These mirrored the effect of TEs on the maintenance of the block, since TEs release momentum and energy to the block (e.g. Shutts, 1983). The sensitivities for TEs at -24 hours can be also seen in Figure 3.26. The block itself appeared here as a positive anomaly around 0°/ 60°N. This could be misleading, since blockings are by definition not transient, but stationary. The reason why the block was visible in the TE signatures is that the background flow for August 2010 was only partly dominated by the Russian heat wave block (as it disappeared after mid-August). Hence, the block appeared in the TE field as positive anomaly. There was a positive TE at 60°W/40°N (coinciding with a positive sensitivity) and a negative TE at 40°W/60°N (coinciding with a negative sensitivity) which were both favorable for the block, as they led to an increase in the metric. A negative sensitivity at 40°W/40°N was within an elongated part of the positive block anomaly. This negative TE sensitivity could be explained in two ways. One possibility was that the elongated part of the block was unfavorable for the main part of the block, as it might have prevented other TEs propagating along the southern jet branch and thus disturbed their release of energy and momentum to the block. Another possibility could be that this elongated part of the positive TE anomaly caused the zonal displacement of an Atlantic AR (Figure 3.27, left), as discussed in the next paragraph in more detail. In a RWB perspective, the negative TE at 0° could be seen as a remnant cut-off low, as often observed in huge blocking systems (Berggren et al., 1949). This negative TE was beneficial for the block as it coincided with a negative TE sensitivity and thus increased the metric. These cut-off systems in the middle of the block benefit the amplification or maintenance of the block, as they trigger the poleward advection of low PV air along their eastern flank. The TE sensitivity pattern showed that positive (corresponding to anticyclonic) as well as negative (corresponding to cyclonic) TEs had an impact on the block. Thus, we did not find that anticyclonic TEs were preferred for the feedback on the block, which is in contrast to the study of Yamazaki and Itoh (2013).
As for the onset phase and the mature stage of the block, we found an effect of ARs on the block. This, however, was now farther east of Greenland (Figure 3.27). In the ensemble mean, an Atlantic AR was visible, whereas the negative and positive sensitivities showed where the air had to be moister

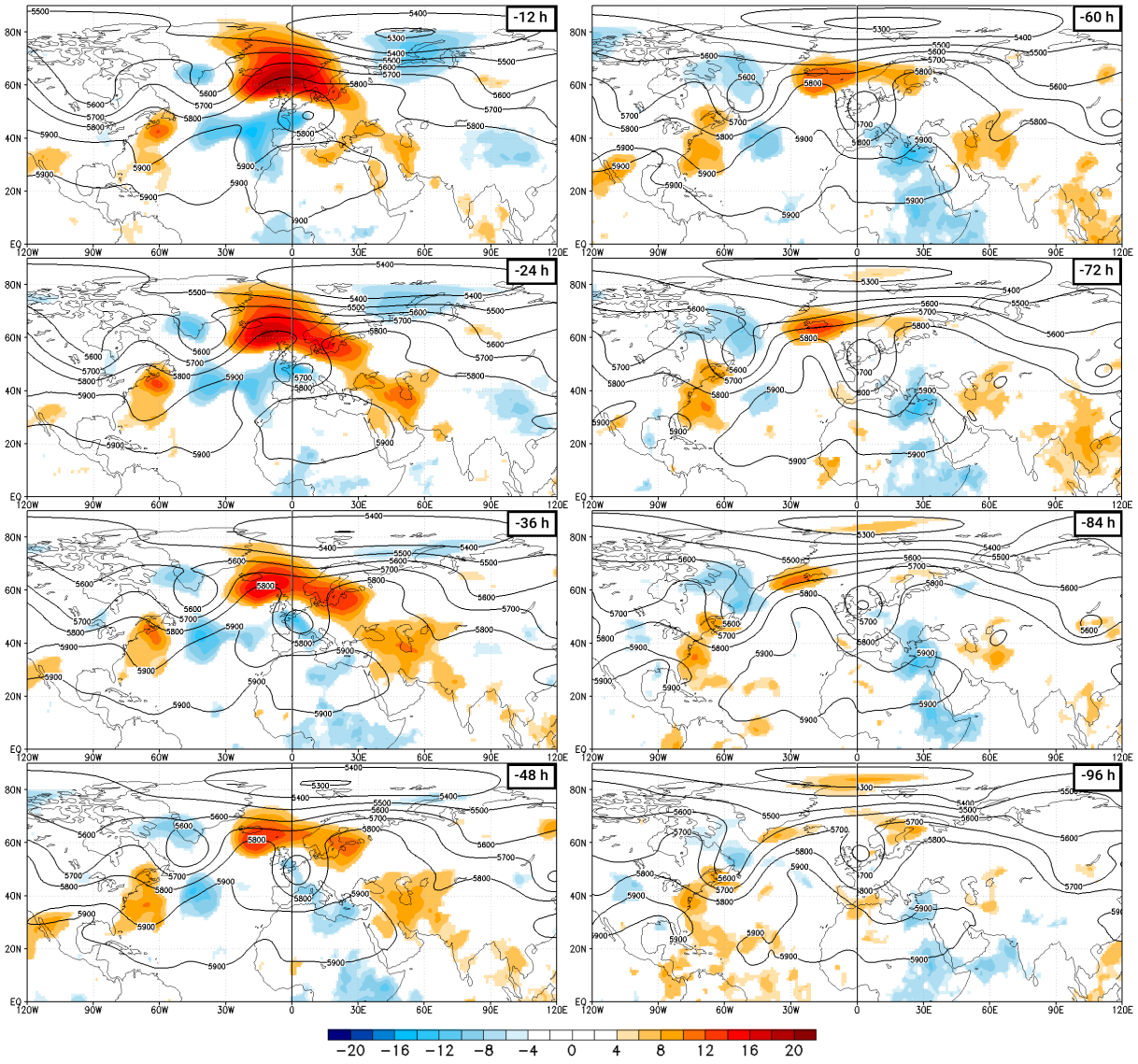

Fig. 3.25.: Statistically significant sensitivity (shading in gpm) of box mean in 500 hPa geopotential height (metric representing block's amplitude during the decay phase) at 1200 UTC 16 August 2010 (being the metric time) to the 500 hPa geopotential height at (from top to bottom, left column) -12, -24, -36, -48, (right column) -60, -72, -84, and -96 hours before metric time, plus corresponding ensemble mean of 500 hPa geopotential height (contours in gpm).

(corresponding to positive sensitivities) and where the air had to be drier (corresponding to negative sensitivities) to be beneficial for the block (corresponding to an increase in the metric). Enhancing the AR to the east of Greenland and shifting the northern portion away from Greenland and towards the north of the British Isles would have a negative impact on the block, as indicated by the negative AR sensitivities. The Atlantic AR transported moisture to the north and was forced to ascend as it reached Iceland. It also made landfall at the eastern coast of Greenland. The resulting cloud formation and precipitation (whose correlation to the block could be seen in the positive sensitivity at 30°W/70°N) led to the release of latent heat which favored the destruction of PV at upper levels and thus supported the maintenance of the blocking system. The negative precipitation sensitivity around 15°W/60°N showed that a southeast shift of the aforementioned precipitation was unfavorable for the block (corresponding to a decrease in the metric).

In summary, the forecast of the decay of the block depended on the performance of the TE feedback, the diabatic forcing over the Atlantic and of the dominance of the high latitude low pressure system downstream.

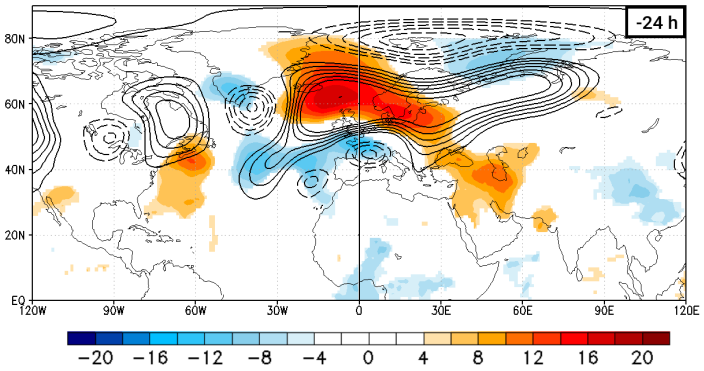

Fig. 3.26.: Statistically significant sensitivity (shading in gpm) of box mean in 500 hPa geopotential height (metric representing block's amplitude during the decay phase) at 1200 UTC 16 August 2010 (being the metric time) to TE at -24 hours before metric time, plus corresponding ensemble mean of TE (contours in gpm), where dotted lines show negative and continuous lines positive values.

3.5. Summary and Conclusions

In this chapter, we investigated the forecast variability of the blocking anticyclone that caused the 2010 Russian heat wave and its impact on surface conditions in the medium forecast range. For three periods in the blocking's life-cycle we extracted main forecast scenarios from a given TIGGE forecast and compared their development. Moreover, we investigated the dynamics that caused the forecast variability of the block.

The onset of a blocking system is associated with the transition from a zonal to a meridional flow pattern. In our case, the onset was forecast in three of four scenarios for the analyzed onset time. This indicates

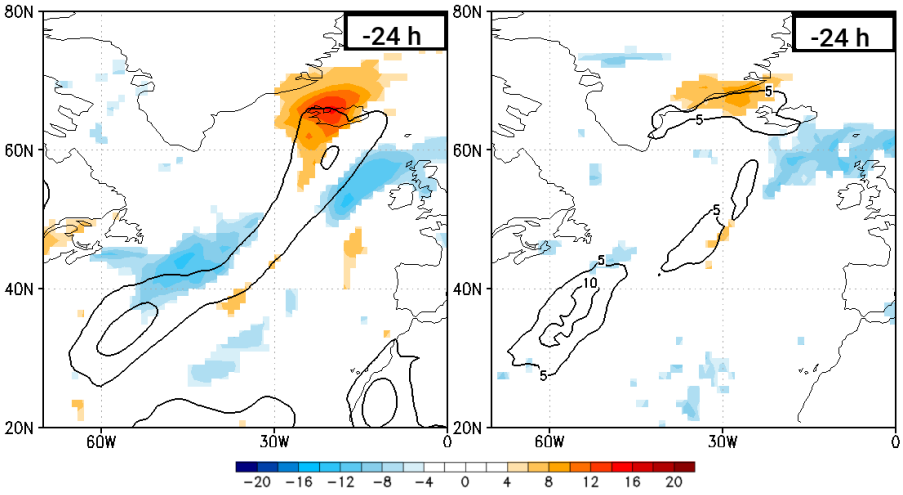

Fig. 3.27.: Statistically significant sensitivity (shading in gpm) of box mean in 500 hPa geopotential height (metric representing block's amplitude during the decay phase) at 1200 UTC 16 August 2010 (being the metric time) to (left) the vertically integrated water vapor transport (corresponding to AR) and to (right) the 12 hourly accumulated precipitation at -24 hours. Corresponding ensemble means in contours (for AR in kg m^{-1} s^{-1}, and for precipitation in mm.).

high predictability, in agreement with previous literature (Matsueda, 2011). However, the variability in the representation of the blocking anticyclone was still large enough to generate significant differences in surface conditions. Therefore, the extension of the heat affected area and the heat intensity varied between the development scenarios, in which the blocking system showed differences in its position, shape and amplitude. After blocking onset, the heat wave developed, resulting in an increase in temperature, heat intensity and wildfire potential. This could be quantified using two heat indices (HI and Humidex) and a fire potential index (LASI). From a dynamical viewpoint, the forecast variability of the block could be traced back to the forecast variability of a downstream as well as an upstream precursor block and of an AR over the Atlantic. The precursor blocks helped this Russian heat wave block to evolve by creating favorable flow conditions, such as the meridional transport of low PV air (Luo et al., 2001). The Atlantic AR led to precipitation at the southern coast of Greenland, leading to upper-level PV destruction due to latent heat release (Schwierz, 2001). The resulting negative upper-level PV anomaly contributed to the precursor block downstream.

Matsueda (2011) indicated that the predictability of the western flank of the Russian heat wave block was lower than the predictability of the eastern flank. This may be connected with the dynamics occurring in the vicinity of the western flank, which is often affected by synoptic-scale disturbances arriving from the west, whereas the eastern flank could be seen as the part of the system which is protected by the amplified ridge upstream from incoming disturbances. In our three forecast scenarios for the mature stage, the tilt and the amplitude of the western flank differed significantly, corroborating the findings of Matsueda (2011). We hypothesize that these differences had a strong impact on the intense precipitation

over Europe, since the precipitation fell mainly just ahead of the trough axis. In comparison to the first guess daily analysis, the precipitation areas in the ensemble members were in the wrong position and the amount of precipitation was overestimated. The poor precipitation forecast is a result of the forecast variability of the block's western flank. Webster et al. (2011) investigated the predictability of precipitation under the block's eastern flank in 15-day ECMWF ensemble forecasts. They found that the heavy rainfall in Pakistan in summer 2010 had a high predictability. With respect to our results, we assume that this may be connected to the smaller forecast variability of the block's eastern flank compared to its western flank. Moreover, we showed that the forecast variability of the western flank also influenced the surface heat distribution farther east, as the western side of the heat affected area below the block was more variable among the EPS members than the eastern side. The forecast variability of the western flank of the block was linked to the forecast variability of the block's amplitude, whereas CWB favored the block's amplification. Furthermore, the forecast variability of the western flank was also caused by the forecast variability of an Atlantic AR and the corresponding modification of the upper-level PV distribution.

The decay of a blocking system corresponds to the transition from meridional to zonal flow conditions. In the analyzed forecast, the decay of the blocking system over Russia in summer 2010 was only captured in one of three forecast scenarios. Thus, the flow was still meridional in two scenarios. However, the end of the heat wave was manifested by temperature drops in all scenarios, regardless of whether the blocking still existed. Without blocking, the upper level conditions are not suitable anymore to support the existence of the heat wave. In our case, the heat wave ended in the scenario with blocking because the blocking system was shifted, meaning that the anticyclonic anomaly and the temperature anomaly were not in phase anymore (Stefanon et al., 2012). The block's forecast variability during the decay phase was linked to the forecast variability of the TE feedback (meaning the release of momentum and energy from the TEs to the block as described by Shutts (1983)) and to diabatic forcing over the Atlantic (resulting in PV destruction at upper levels). The impact of TEs on the predictability of extratropical seasonal-mean predictability was discussed in the study of Kang et al. (2011). They found that better TE statistics in models can increase predictability in extratropics on a seasonal scale. In the study of Chen and Juang (1992) general circulation model experiments were carried out to investigate TE activity on blocks in the medium forecast range. They showed that the predictability of blocks depended on the forecast quality of TEs. If the TEs were represented well in the forecast or part of the initial conditions, the prediction of blocks was improved. These studies reinforce our result that the forecast variability of TEs influenced the forecast variability of the 2010 summer block.

In our case, the predictability of the block's decay was lower than that of the block's onset. During the mature stage, the block was forecast in all development scenarios. There was, however, a remarkable uncertainty in the representation of the block's western flank. These results agree with the study of Matsueda (2011), in which TIGGE ensemble forecasts were investigated also, however, including the EPS from the Japan Meteorological Agency and from the Canadian Meteorological Center. We hypothesize

that the forecast variability of the heat wave (as well as the precipitation over Europe during the mature stage) resulted from the forecast variability of the blocking system. We could show that slight differences in the representation of the block already had a strong influence on surface variables. Since we used 10-day forecasts, we assume in our case that other variables like soil moisture (being more important on longer time scales) were less responsible for the forecast uncertainty of the heat wave.

Heat intensity was investigated in terms of heat indices, which consider 2 m temperatures and surface moisture as well (being favorable as indicator for humid heat). For our case, the beginning and end of the heat wave could be identified with both heat indices. Thus, it seems to be a promising tool to use these indices with TIGGE data for heat warnings. The particular dates when a specific warning threshold was reached differed between forecast scenarios by up to six days. Such differences are highly relevant for the population that is affected by heat, since long-lasting heat periods can stress the metabolic system. Furthermore, our comparison for the onset and the decay phase of the block between a grid point forecast for Moscow and a forecast for a spatial mean (averaging area: 35°E-55°E and 50°N-60°N) showed that, as would be expected, the spread between the scenarios and the amplitude of the fluctuations (in e.g. maximum temperature) within one scenario were larger in the grid point forecast. In addition to the smoothing effect in averaged variables, this indicates the spatial limitations in forecast quality, and the challenge in issuing grid point-based warnings. For improving the forecasts near the grid point scale, a higher horizontal resolution may be beneficial (Hamill et al., 2000).

The ESA was suitable for the investigation of the dynamics which caused the forecast variability of the blocking system at the clustering times. Therefore, we could identify the relevant dynamical features for each phase of the block. However, the investigation with the ESA is limited by some factors. First, only linear relations can be investigated. However, previous studies showed that linear sensitivities have an impact on non-linear evolutions for periods within the medium range (Chang et al., 2013). Another point is the choice of a suitable forecast metric that can be a challenging task. In our case, the different metrics worked well. For the onset and the decay phase of the block, we used a metric which should reflect the block's amplitude (a peak value for the onset and a spatial mean for the decay). For the mature stage of the block, we created a wave breaking index, showing cyclonic or anticyclonic breaking of the block's western flank. However, the sensitivities were stronger with the metrics for the onset phase and the mature stage of the block. For the decay phase, we used a spatial mean as metric, with which we got weaker results, indicating that a spatial mean is not the best choice for a forecast metric. However, this is only an assumption, because the sensitivities for the decay phase of the 2010 heat wave block could be less intense in general. The study of Chang et al. (2013) also considered different forecast metrics. They investigated Pacific extratropical cyclones in medium-range forecasts and found that the leading PCs were more suitable as forecast metric than cyclone parameters. Additionally, ESA signals can be unclear and can have a more random appearance without linkage to synoptic patterns, making the interpretation difficult. A good indicator for reasonable ESA signals are consistency in time, consistency between different fields (for example between MSLP and geopotential), and that they are linked to syn-

optic features. Since this was the case in our study, we have confidence in our results from the ESA. Therefore, the ESA approach is not only suitable to investigate the impact of initial condition errors on the forecast (e.g. Torn and Hakim, 2008), but also to investigate dynamical processes (already shown in earlier studies). For example, Keller (2017) did sensitivity studies to investigate the amplification of the downstream wave guide during extratropical transition. Our study is the first that used the ESA approach to investigate forecast variability of atmospheric blocking.

Keller et al. (2011) investigated the forecast variability of synoptic patterns associated with extratropical transition in TIGGE and tried to specify the role of the ECMWF EPS within TIGGE. They found that TIGGE offered a broader range of possible scenarios in particular if ECMWF members were included in the multi-model ensemble. Regarding our investigations of the atmospheric blocking event, for the three investigation periods of the block, the ECMWF as well as the NCEP EPS contained members in all development scenarios. Since the ECMWF as well as the NCEP EPS captured the full range of development scenarios, the ECMWF did not have some kind of special status by providing additional scenarios as in the ET study of Keller et al. (2011). For the onset and the decay phase of the block, the UKMO ensemble missed one development scenario, respectively.

In conclusion, our results indicate that the low predictability of the 2010 summer block transferred to a low predictability of surface conditions relevant for human comfort. The forecast variability of the block during the onset phase was linked to the evolution of up- and downstream precursor blocks. During the mature stage, the shape and position of the block's western flank was related to the block's amplitude. During the decay phase, the TE feedback was of high relevance for the blocking system. Diabatic processes seemed to be important during the whole life-cycle of the block, by creating or at least supporting upper-level negative PV anomalies.

4. Subseasonal Forecasts

4.1. Introduction

In this chapter, we turn away from the medium forecast range and take ourselves to the "desert of predictability" (Vitart et al., 2016), meaning the subseasonal to seasonal forecast range. As before, the forecast variability of the blocking system over Russia in summer 2010 is investigated. Here, we address the following research questions. How is the blocking system represented in ensemble forecasts on the subseasonal range? Is there a limit of predictability? And which results arise from clustering with a reduced number of members and with such long forecast lead times?

The investigations were restricted to the onset and the decay phase of the block. Thus, we did not consider the mature stage of the block. We limited our analysis in this way, since our aim was to assess whether the block evolved and decayed or not at these long forecast ranges. The details discussed for the mature stage in the previous chapter are less meaningful for forecast lead times over 15 days, for which the ensemble spread is clearly larger than for lead times of 10 days and below.

The Subseasonal-to-Seasonal (S2S) project provides data for this forecast range. One of the S2S research priorities is to focus on some specific extreme event case studies as it is done in this study. We used ensemble forecasts from ECMWF, NCEP and UKMO as multi-model ensemble with lead times of 45 days. To investigate the forecast variability of the block in the subseasonal range and to address the third research question, we used the same methods as for the medium range. Thus, the variability patterns are discussed in terms of EOF 1 and EOF 2. With the fuzzy clustering, we extract the main development scenarios for each forecast. For these scenarios, blocking was examined with the help of the index of Tibaldi and Molteni (1990). Figure 4.1 offers a schematic overview of the used data and methods.

This chapter is structured as follows. First, the data is presented. After that the methods are introduced. The results of the investigations of the predictability for the onset and the decay phase of the block are then shown and discussed. The chapter is concluded with a section containing summary and conclusions.

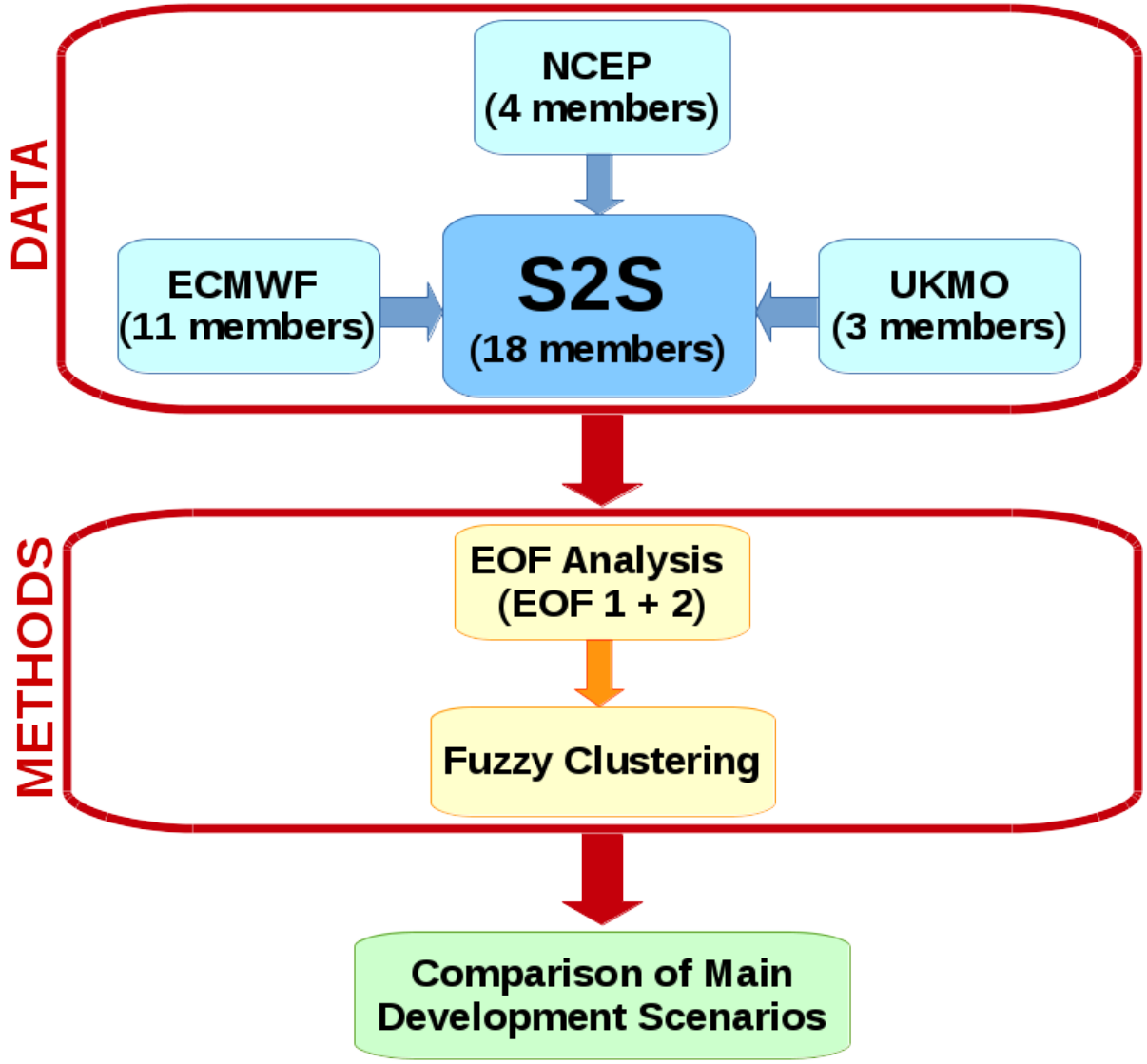

Fig. 4.1.: A schematic overview of data and methods used for the investigations of the predictability of the Russian summer block in 2010 in the subseasonal forecast range.

4.2. Data

In this section, the background information about S2S is taken from the S2S homepage [1] and the ECMWF homepage [2], unless specified differently.

To investigate the predictability of the 2010 Russian heat wave block in the subseasonal forecast range, we used the reforecasts from the Subseasonal to Seasonal Prediction (S2S) Project Database. S2S is an extended version of the TIGGE dataset, as the S2S products are available for lead times of 30 days and more (Vitart et al., 2014). The aims of the S2S Project are to build a bridge between weather and climate and to improve our understanding of predictability in the subseasonal to seasonal forecast range (Vitart et al., 2014). The idea of the S2S was first developed in 2009. Finally, in 2013, S2S was brought into being. Since 2015, ensemble forecasts have been calculated for the extended forecast range by the 11 contributing EPS. As for TIGGE, the S2S offers the opportunity to combine the ensemble forecast form the different EPS to do research with a multi-model ensemble.

Since the calculations started after 2010, real-time forecasts were not produced for this year. However, reforecasts, which are also known as hindcasts, are available. Hindcasts are defined as retrospective weather forecasts which are generated with a fixed numerical model (Hamill et al., 2006). They are used for studying predictability, for diagnosing model bias, or for statistically correcting weather forecasts (Hamill et al., 2006). There are two ways to generate hindcasts. The first method is called *fixed*, which means that the hindcasts for a specific period are calculated all at once with a certain model version. The second method is called *on the fly*. There, the hindcasts are calculated gradually at the same time as the real-time forecasts. When and how often per week the calculations are made, depends on the prediction center.

To remain consistent with the analysis of the medium forecast range, we chose the same three EPS, namely ECMWF, NCEP and UKMO. At NCEP, the hindcasts are calculated with a *fixed* model version from 1 March 2011, whereas ECMWF and UKMO are calculating the data *on the fly*. Whether the generation of hindcasts is *fixed* or *on the fly* does not make any difference for this case study, but would have an impact if studying a longer period in which model changes for ECMWF and UKMO can influence the dataset. The reforecasts are interpolated to a common grid of 1.5° x 1.5°. In addition, we used 24 h forecast intervals. The number of ensemble members is reduced in the reforecasts compared to the real-time forecasts. ECMWF provides 11 members, NCEP 4 members, and UKMO 3 members. Consequently, our multi-model ensemble forecasts consisted of only 18 members. Table 4.1 gives an overview over the features of the reforecasts corresponding to the EPS.

In contrast to the medium forecast range, we confined ourselves here to only one variable. We decided to use the geopotential height at 500 hPa for three reasons. First, it is available in the chosen EPS. Second, it is suitable to investigate atmospheric blocking. Third, it is sufficient to get an impression of the forecast

[1] `http://s2sprediction.net/`

[2] `http://www.ecmwf.int/en/research/projects/s2s`

Tab. 4.1.: Characteristics of S2S reforecasts from ECMWF, NCEP and UKMO.

EPS	System	ensemble size	reforecast frequency	grid
ECMWF	on the fly	11	Mon and Thu	1.5x1.5
NCEP	fixed	4	daily	1.5x1.5
UKMO	on the fly	3	1st, 9th, 17th, 25th of each month	1.5x1.5

variability of the heat wave, since the predictability of such an extreme event depends on the prediction of the anticyclonic flow pattern (Vitart et al., 2014).

4.3. Methods

4.3.1. Selection of Forecasts

The number of suitable forecasts was limited for different reasons. Since we wanted to investigate the predictability in the subseasonal range, the initialization of the forecasts had to be 10 days or more before the onset and the decay of the block, respectively. In addition, as the hindcasts are calculated differently by the EPS (*fixed* or *on the fly*), only a few initialization dates could be found which were available from all three EPS. Considering these points, we found three suitable forecasts for the block's onset (Table 4.2) and the decay (Table 4.3), respectively.

4.3.2. Selection of Main Development Scenarios

To extract the main development scenarios from the ensemble forecasts, we used the EOF and clustering methodology which was introduced in the medium-range part of this work. Therefor, we had to determine several clustering parameters:

- *Clustering variable*: Since we reduced our investigations for the subseasonal range to considerations of the 500 hPa geopotential height, we used this fields as clustering variable.

- *Clustering time*: For the medium range, we had tried to capture the full bandwidth of scenarios, so that we had used the time of the largest ensemble spread as clustering time. Here we wanted to know, whether the blocking event could be predicted at these extended time scales at all. This was why we focused on the actual occurrence of the event. Thus, for the onset phase, we used the analyzed onset date, namely 20 June 2010, as clustering time for all three forecasts. For the decay phase, the analyzed decay date of the block, namely 17 August 2010, was used.

Tab. 4.2.: Clustering parameters for the three forecasts for the onset phase of the block.

Initialization	0000 UTC 25 May 2010	0000 UTC 1 Jun 2010	0000 UTC 9 Jun 2010
Clustering time	0000 UTC 20 Jun 2010 + 26 days	0000 UTC 20 Jun 2010 + 19 days	0000 UTC 20 Jun 2010 + 11 days
EOF area	40-80°N, 40°W-120°E	40-80°N, 40°W-120°E	40-80°N, 40°W-120°E
No. of clusters	3	3	3
No. of members per cluster	6, 6, 4 (no cluster: 2)	6, 5, 6 (no cluster: 1)	2, 8, 5 (no cluster: 3)

Tab. 4.3.: Clustering parameters for the three forecasts for the decay phase of the block.

Initialization	0000 UTC 9 Jul 2010	0000 UTC 25 Jul 2010	0000 UTC 1 Aug 2010
Clustering time	0000 UTC 17 Aug 2010 + 39 days	0000 UTC 17 Aug 2010 + 23 days	0000 UTC 17 Aug 2010 + 16 days
EOF area	40-80°N, 40°W-120°E	40-80°N, 40°W-120°E	40-80°N, 40°W-120°E
No. of clusters	3	3	3
No. of members per cluster	6, 5, 5 (no cluster: 2)	7, 6, 4 (no cluster: 1)	4, 6, 4 (no cluster: 4)

- *Calculation Area*: For the calculation of the EOFs we used a similar area to that chosen for the medium-range investigations. However, the northern extension of the area was reduced to 80°N, because there was a lack of data close to the pole in the UKMO ensemble forecasts. Consequently, the calculation area extended from 40°N to 80°N and from 40°W to 120°E.

- *Number of clusters*: As for the medium range, we considered the stability criteria. In contrast to the medium range, we chose the same number of clusters for all six forecasts, namely the 3-cluster solution. The 3-cluster solution was stable for all forecasts. This consistency was helpful since we wanted to compare three forecasts for each life-cycle phase (for the medium range, we had only one forecast per phase).

An overview of the clustering parameters is given in Tables 4.2 and 4.3. As for the medium-range investigations, we defined the members closest to the cluster centers as representative for the different development scenarios.

4.3.3. Blocking Identification

For the identification of the block, we used the index of Tibaldi and Molteni (1990) which was already introduced in section 3.3.3. We confined ourselves to this index, since we only used the 500 hPa geopotential height for our investigations of forecast variability of the blocking system in the subseasonal range.

4.4. Results

This section deals with the results for the onset and the decay phase of the block. In the six forecasts, the date of the onset or decay was at different lead times. For the onset phase, the initialization times were 11 to 26 days before the analyzed onset date (20 June). For the decay phase, the forecasts were initialized 16 to 39 days before the analyzed decay (17 August).
The results are presented for each forecast in following order. First, the forecast variability is discussed in terms of EOF 1 and 2. After a description of the EOFs, the distribution of the members to the clusters is discussed. Then, the main development scenarios are presented. Afterwards, we compare the cluster composites to the corresponding representative members, to analyze how *representative* the chosen forecast members are. You have to keep in mind that the anomalies in the 500 hPa geopotential height field of the composites are always smaller than those of the representative members, because of the smoothing effect from the averaging. This becomes more and more dominant towards the end of the forecast. Finally, the main development scenarios are described. For this we only consider the flow structure of the representative members.

4.4.1. Forecast Variability during the Onset Phase of the Block

The first forecast was initialized on 25 May 2010, i.e., 26 days before the observed onset of the block. The ensemble spread was already large over the Atlantic before onset, with peak values of 120 gpm on 13 June (Fig. 4.2, top, left). Compared to the blocked longitude, the variability was increased in upstream and downstream regions. The second forecast was initialized on 1 June 2010, thus, 19 days before blocking onset. A strong signal of the averaged standard deviation over the Atlantic-European sector was visible quite before the block evolved (Fig. 4.2, top, right). Afterwards, the ensemble spread decreased over this sector, except for regions around 0°. The third forecast was initialized on 9 June, 11 days before onset, being at the longer end of the medium range. In this forecast, there was a large ensemble spread directly before the onset between 0° and 40°E (Fig. 4.2, bottom). At the blocked longitude, the ensemble spread was small between 21 June and 3 July, then it increased, since a signal in the 500 hPa geopotential height standard deviation (of 100 gpm) had entered from the west. This signal of high variability evolved at 80°W at the end of June.

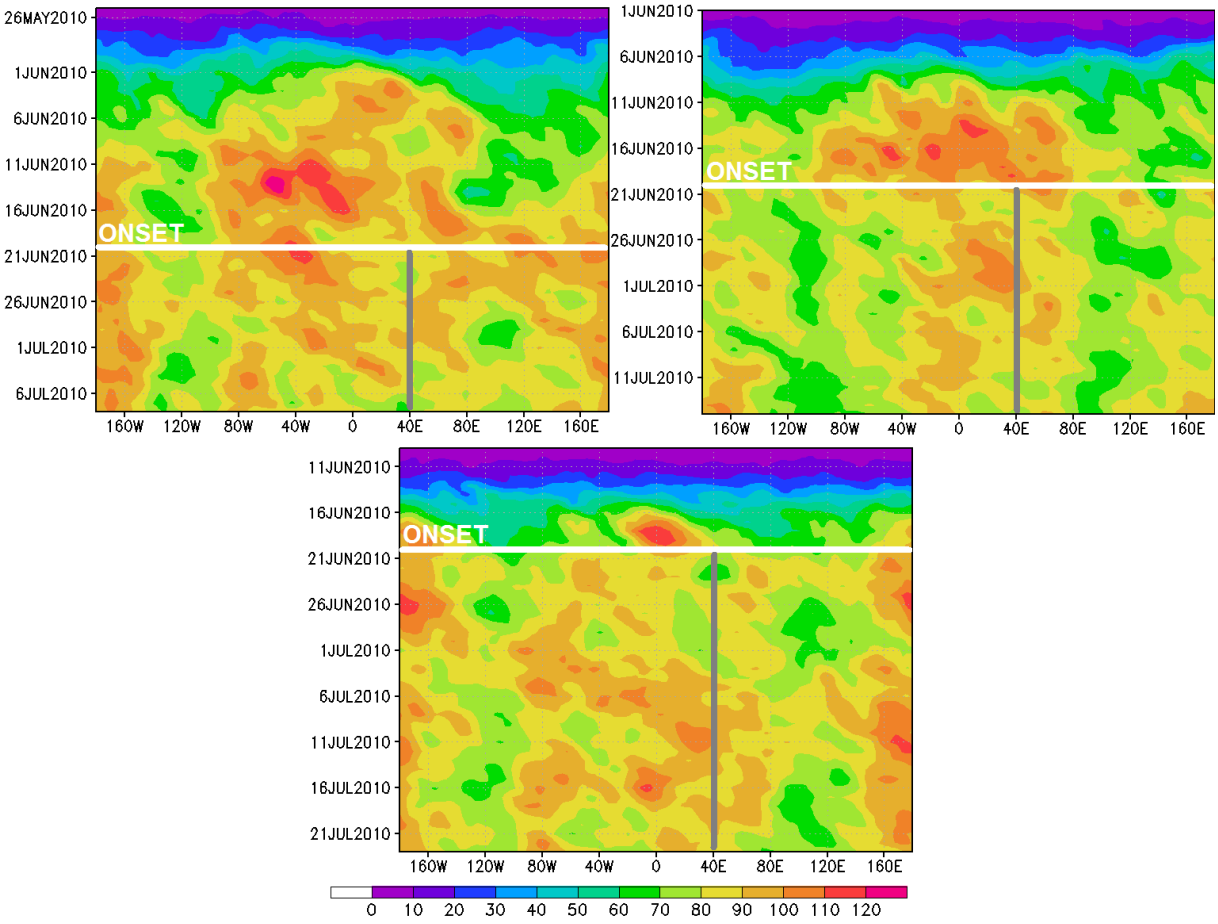

Fig. 4.2.: Hovmoeller diagrams for standard deviation of 500 hPa geopotential height (in gpm) in the S2S EPS 45-day forecasts, averaged between 40°N and 80°N. The white horizontal lines mark the clustering times and the gray vertical lines the blocked longitude. The forecasts are initialized at 0000 UTC 25 May 2010 (top, left), at 0000 UTC 1 June 2010 (top, right), and at 0000 UTC 9 June 2010 (bottom).

Characteristics of the Forecast initialized on 25 May 2010

EOF 1 and 2 represented over 34 % of the total variability, with EOF 1 capturing 28.8 %. A negative signal of EOF 1 spanned from 10°W to 80°E with peaks west and east of the blocked longitude (Fig. 4.3, left, top). Positive values of EOF 1 were visible around 100°E and along the 75th latitude. Positively contributing members had a stronger ridge at 80°E with a cut-off at 60°E and a deeper trough at 20°E. Negatively contributing members showed a double-ridge structure at 60°E and 20°E, with the latter more amplified. EOF 2 reflected 16.0 % of the variability and had a dominant negative signal at 40°E/70°N, which was adjacent to positive values of EOF 2 around 100°E (Fig. 4.3, left, bottom). A member that had a positive contribution to EOF 2 showed a less amplified ridge at 40°E, which could be interpreted as case without blocking. A member with negative contribution was related to a more amplified ridge, being representative for a case with blocking.

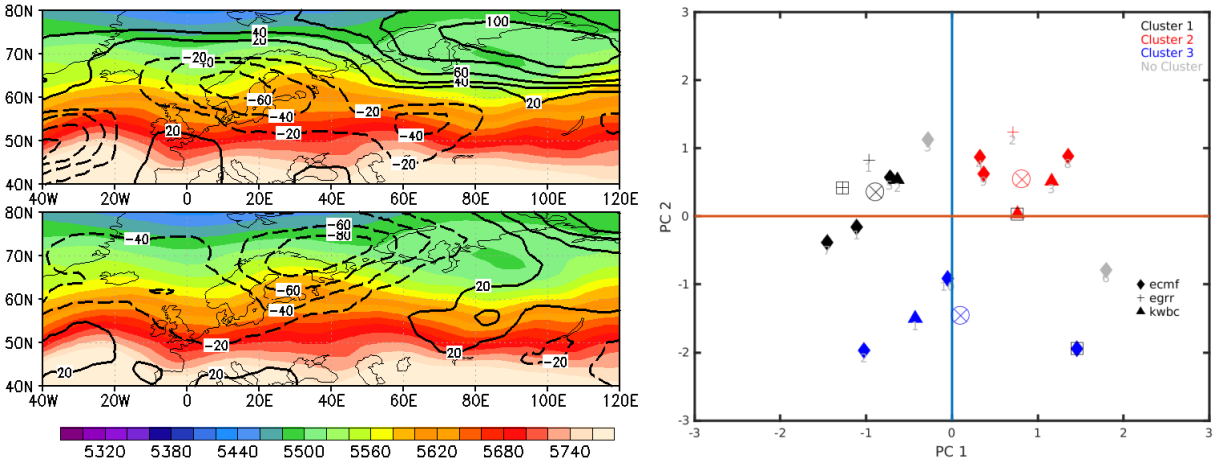

Fig. 4.3.: Left: Ensemble mean of the 500 hPa geopotential height (shaded, in gpm) and distribution of (top) EOF 1 and (bottom) EOF 2 (contours, in gpm) at +26 days (0000 UTC 20 June 2010) for the forecast initialized at 0000 UTC 25 May 2010. Right: The first and second principle component (PC) for the 3-cluster solution based on EOFs from S2S ensemble members (forecast initialized 0000 UTC 25 May 2010) at +26 days (0000 UTC 20 June 2010). Symbols show the EPS membership (rhombus for ECMWF, triangle for NCEP, and cross for UKMO) and colors the cluster membership. Cluster centers are defined by the circled cross.

The 3-cluster solution of the forecast initialized on 25 May 2010 had the following characteristics. 16 of the 18 members were involved in the clustering (Fig. 4.3, right). Cluster 1 and cluster 2 had each 6 members, and cluster 3 consisted of 4 members. Cluster 1 had a negative contribution to EOF 1, whereas it was more or less neutral to EOF 2. Members of cluster 2 contributed positively to EOF 1. In cluster 3, members had a negative contribution to EOF 2. Additionally, the spread between the members within cluster 3 was larger, compared to those in cluster 1 and 2.

The differences between the cluster composites and the representative members varied from cluster to cluster. The flow structure shown by the composite of cluster 1 was similar to that of the corresponding representative member, except with regards to the amplitude of the ridge at 20°E, which was larger in the composite (Fig. 4.4, top). The discrepancy between the representative member and the composite of cluster 2 was much larger (Fig. 4.4, middle). The ridges at 30°W and 60°E were more amplified in the representative member. Consequently, cluster 2 had members, which showed less amplified ridges or even troughs there. Despite these differences it was still clear that the representative member belonged to this cluster. For cluster 3, the composite and the representative member were quite similar.

Considering the representative members, the scenarios could be described as follows. Scenario 1 did not show a blocking ridge at 40°E on 20 June 2010 (Fig. 4.4, top). This could be validated with the index of Tibaldi and Molteni (1990), which did not reach the thresholds for blocking (not shown). The ridges over Europe between 0° and 90°E were even less amplified compared to the ridges upstream and downstream. In scenario 2, there was an amplified ridge over the eastern European-Russian sector (Fig. 4.4, middle).

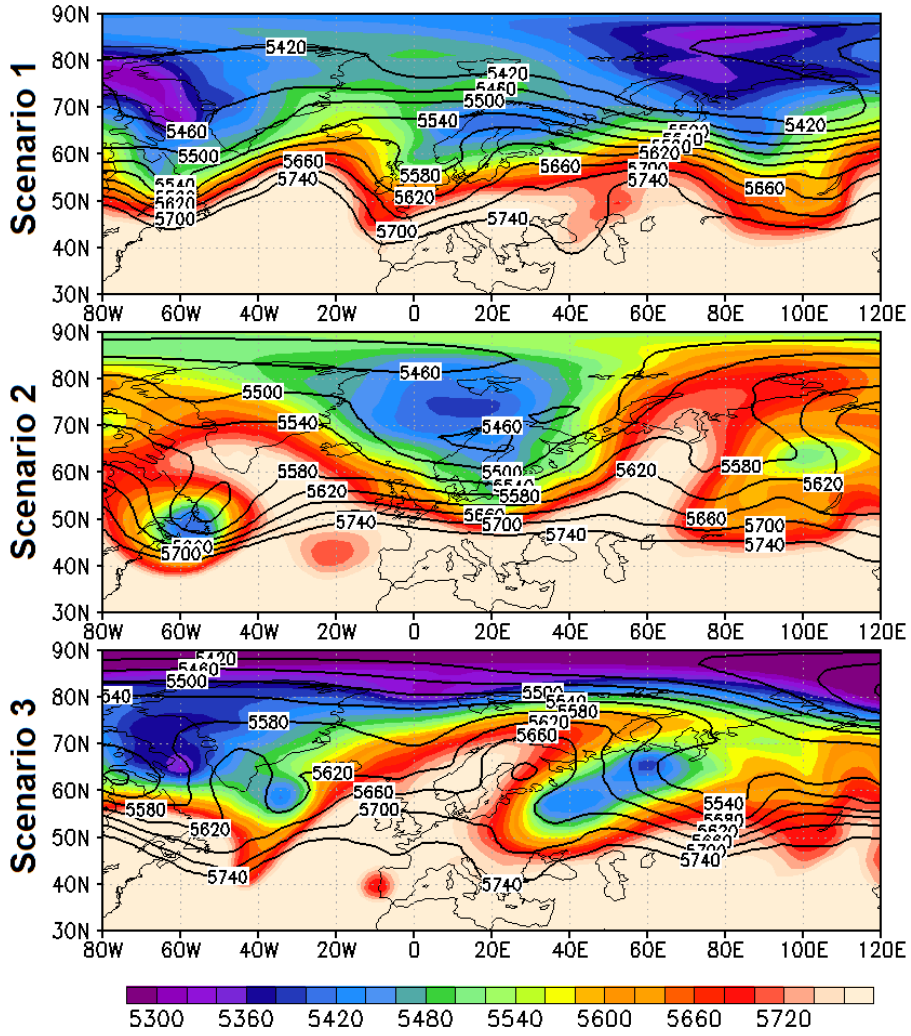

Fig. 4.4.: 500 hPa geopotential height (in gpm) for the three representative members (shading) as well as the corresponding cluster composites (contour) at +26 days (0000 UTC 20 June 2010) from the forecast initialized at 0000 UTC 25 May 2010.

This ridge had a blocking effect, which could be proven with the blocking index (not shown). After 20 June, the amplitude of the ridge first decreased, but subsequently the ridge merged with an upstream ridge (not shown). The resulting system kept its blocking character. A blocking ridge was also visible in scenario 3 (Fig. 4.4, bottom). Here, the block was located too far to the west, at around 0°. In addition, it decayed already after four days (not shown).

In summary, scenario 1 was a case without blocking. In scenario 2, there was a block, which was first located too far east. And scenario 3 also showed an amplified ridge with blocking character, however, this one did not become persistent and was located too far west.

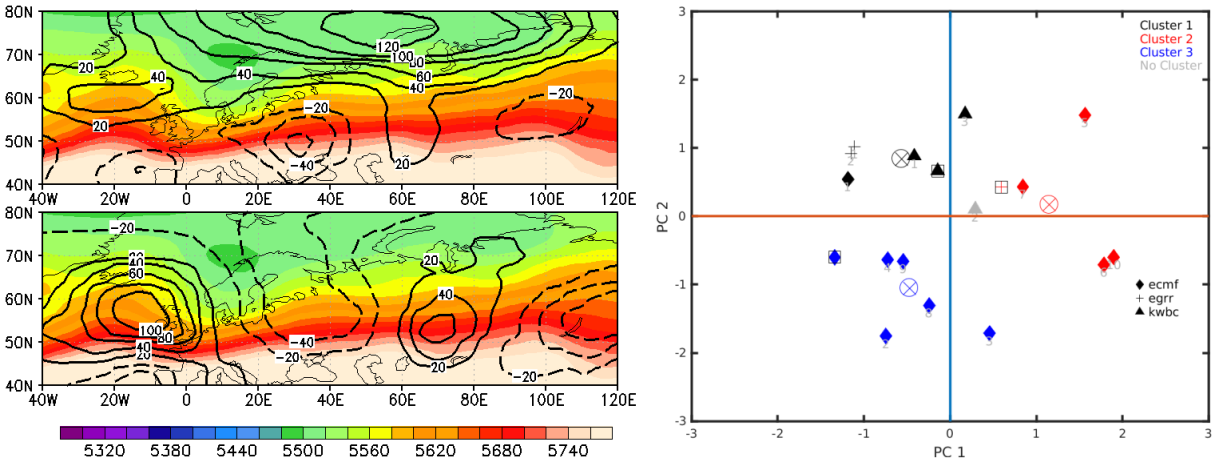

Fig. 4.5.: As in Fig. 4.3, but at +19 days (0000 UTC 20 June 2010) for the forecast initialized at 0000 UTC 1 June 2010.

Characteristics of the Forecast initialized on 1 June 2010

36.5 % of the total variability could be explained with EOF 1 and 2. 30.3 % of the variability was captured by EOF 1. There was a strong positive signal which dominated northern areas between 60°N and 80°N (Fig. 4.5, left, top). At 60°E, the positive signal reached farther south. Negative values of EOF 1 could be found around 50°N at 10°W, 30°E and 100°E. A member with a positive contribution to EOF 1 had an amplified ridge at 60°E and a member with a negative contribution had less amplified ridges of shorter wavelengths at 30°E and 100°E. Thus, EOF 1 could be interpreted as an amplitude pattern (Anwender et al., 2008). EOF 2, which captured 16.2 % of the variability, showed a pattern with zonally orientated alternating positive and negative values (Fig. 4.5, left, bottom). It was a mixture of shift and amplitude pattern (Anwender et al., 2008). A positively contributing member had ridges at 20°W and 70°E, whereas the former was more amplified. A member with negative contribution to EOF 2 had ridges at 30°E and 100°E.

The clusters had a different number of members. Cluster 1 and 3 had each 6 members (Fig. 4.5, right). Cluster 2 had 5 members. One member could not be classified with one of the clusters. Cluster 1 had a positive contribution to EOF 2, cluster 2 to EOF 1. Members of cluster 3 contributed negatively to EOF 2. Moreover, the spread between the members was smallest within cluster 1.

The representative members for the clusters agreed quite well with the cluster composites at clustering time (Fig. 4.6). However, the evolution in the forecast members was not consistent within cluster 3, so that there were members with and without blocking (not shown). Nevertheless, in the following, we will describe the development in all clusters with the help of their representative members, since it turned out to be a proven way to describe the main development scenarios (in the medium-range and in the other subseasonal forecasts).

Scenario 1 had an amplified ridge at 80°E at clustering time (Fig. 4.6, top). This ridge underwent anticy-

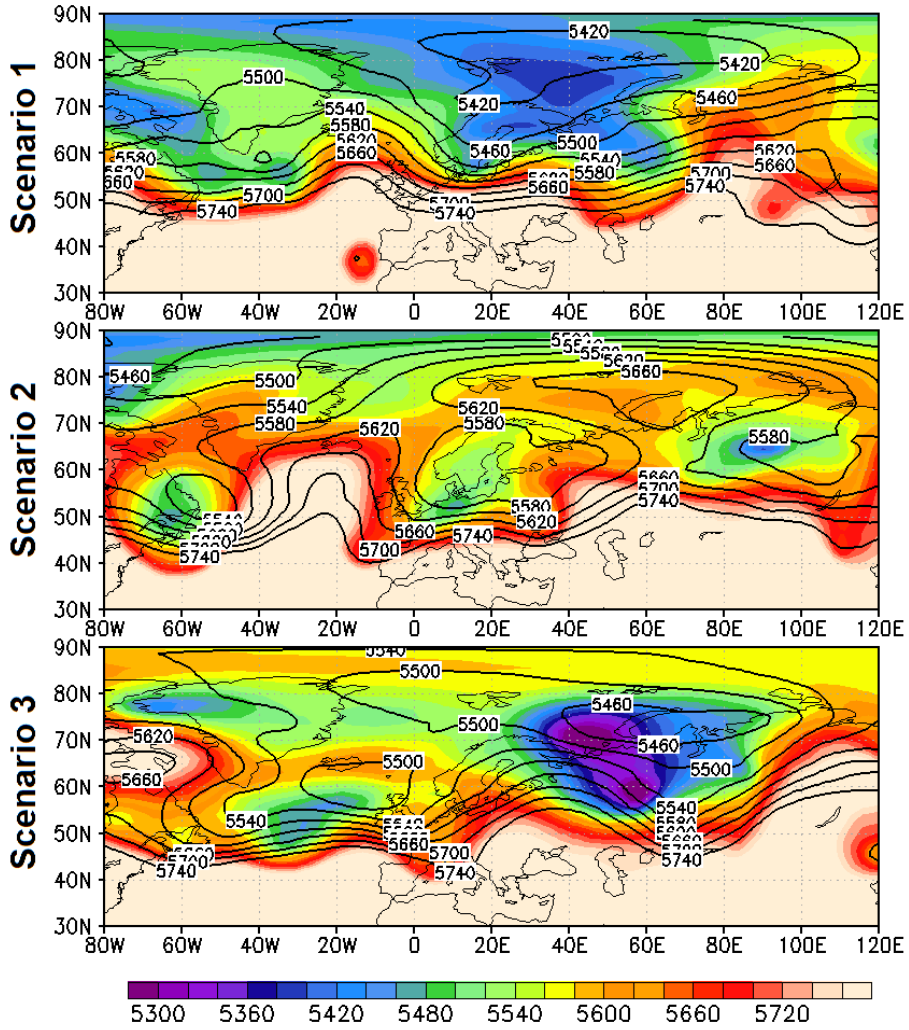

Fig. 4.6.: As in Fig. 4.4, but at +19 days (0000 UTC 20 June 2010) for the forecast initialized at 0000 UTC 1 June 2010.

clonic breaking within the next days (not shown). After another breaking event, the flow became more zonal over Europe. Consequently, no blocking event was identified by the blocking index (not shown). There was also no block in scenario 2 (Fig. 4.6, middle). A ridge over the Atlantic basin at 30°W was just amplifying. However, this system did not attain a blocking character either. In scenario 3, a ridge at 100°E, which had developed 2 days earlier, could be identified as block. It lasted for 5 days, thus, it was only a short-lived system and not comparable with the block that caused the Russian heat wave. In all scenarios, there was only a less amplified ridge at 40°E, where the Russian heat wave block was located in observations.

In conclusion, scenario 1 as well as 2 did not contain a block. In scenario 3, there was a short blocking event, which was shifted to the east in comparison to observations, where 40°E was identified as blocked longitude.

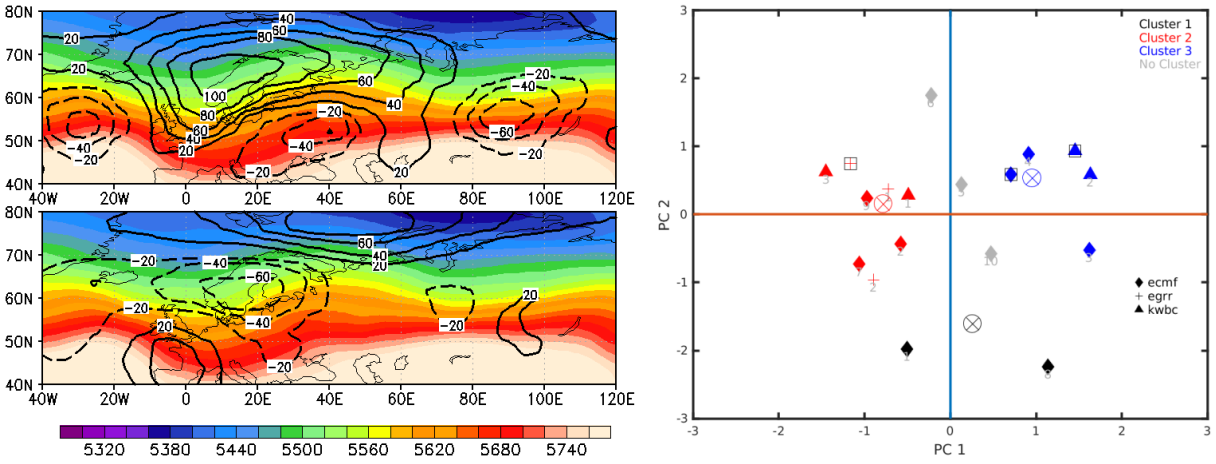

Fig. 4.7.: As in Fig. 4.3, but at +11 days (0000 UTC 20 June 2010) for the forecast initialized at 0000 UTC 9 June 2010.

Characteristics of the Forecast initialized on 9 June 2010

EOF 1 captured 26.3 % of the variability. It had one large-scale positive anomaly extending from 20°W to 80°E as well as three negative anomalies between 50°N and 60°N at 30°W, 30°E, and 90°E (Fig. 4.7, left, top). Positively contributing members showed a strong ridge between 0° and 60°E with a cut-off low at 40°E/50°N. Negatively contributing members showed a trough-ridge structure with smaller amplitudes. EOF 2, which represented 15.9 % of the variability, was distributed as follows. There was a positive-negative-positive signal extending from 5°W/45°N to 45°E/75°N (Fig. 4.7, left, bottom). A member with a positive contribution had an amplified ridge at 40°E and a trough at 20°E with a shortwave ridge at 0°. A member with negative contribution showed a ridge at 20°E and a cut-off low at 0°/45°N.

Cluster 1 had 2 members with a negative contribution to EOF 2 (Fig. 4.7, right). The spread between these two members was quite large. Most of the members were part of cluster 2. These members contributed negatively to EOF 1. 5 members, having a positive contribution to EOF 1, belonged to cluster 3. 3 members remained, which could not be clearly assigned to one of the clusters.

The wave structures shown in the representative members were very similar to those in the cluster composites (Fig. 4.8). The only notable deviation was in scenario 2. Here, a ridge positioned at 30°W in the composite was seen centered on 60°W in the representative member (Fig. 4.8, middle).

In scenario 1, a block developed on 20 June at 40°E (Fig. 4.8, top), in agreement with observations and analysis. However, the predicted block of scenario 1 decayed after 8 days. At this time, the ridge without blocking character was still at the same position, but less intense (not shown). A block formed at 40°E in scenario 2 also (Fig. 4.8, middle). This block was sustained by upstream wave breaking events; however, it decayed after a few days (not shown). At clustering time, there was also a ridge at the analyzed blocking longitude in scenario 3 (Fig. 4.8, bottom). This ridge did not block the flow. Four days later,

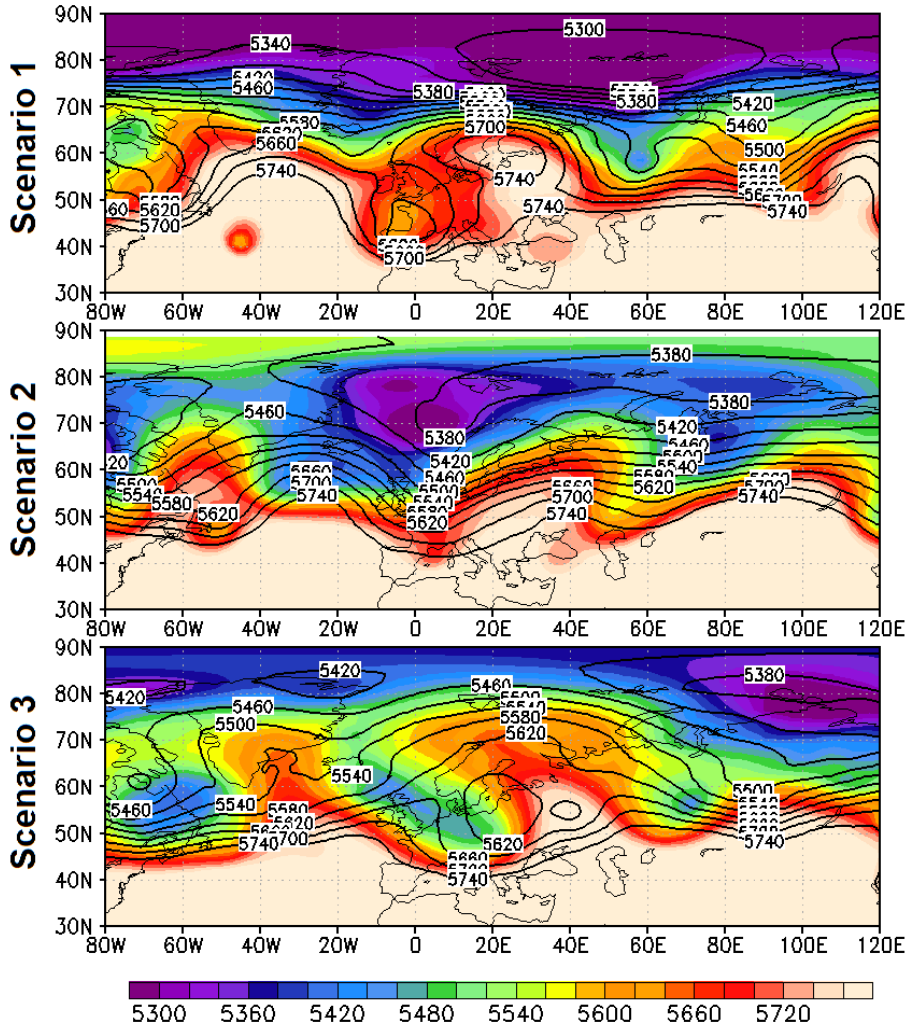

Fig. 4.8.: As in Fig. 4.4, but at +11 days (0000 UTC 20 June 2010) for the forecast initialized at 0000 UTC 9 June 2010.

the flow over Europe was more zonal (not shown).

In summary, in scenario 1 and 2, a blocking ridge developed. The position and the date for onset were in good agreement with the analysis. However, in both scenarios, the block decayed after a few days. Scenario 3 did not show a blocking system.

Discussion

All three forecasts exhibited a large ensemble spread upstream of the blocked longitude before the observed onset date of 20 June (Fig. 4.2). In all ensemble forecasts, there were members which were able to predict the block's onset. Differences were seen, however, in position, amplitude, the precise onset date and the duration of the block. These differences are discussed below.

In the forecast initialized on 25 May, 26 days before the observed onset time, a block was identified in

two of three scenarios (Fig. 4.4). In the two blocking scenarios, the position was predicted too far west or east. Furthermore, the block remained in only one of these two blocking scenarios. In the other blocking scenario, the block decayed after four days.
The second forecast, which was initialized 19 days before onset on 1 June, there was only one blocking scenario (Fig. 4.6, scenario 3). In two scenarios, no block evolved. And in the blocking scenario, the block decayed after five days. Moreover, the position of the block was 60° farther east than in the analysis.
The third forecast was initialized 11 days before onset on 9 June. In all scenarios, an amplified ridge developed at 40°E (Fig. 4.8). It had a blocking character in two out of three scenarios (scenarios 1 and 2). Even if the position and the precise onset date were predicted very well in the blocking scenarios, they failed to predict the observed duration, since the block decayed after a few days in the forecast.
Comparing the three forecasts, we found that an initialization time closer to the clustering time, did not lead to an overall improvement of the forecast quality. The block's position was captured better in the forecast with shorter lead times. However, the prediction of the correct duration of the block was still a problem for shorter lead times. The duration was even better predicted in the blocking scenario of the earliest forecasts. Thus, regarding the forecasts initialized at later times, there was only an improvement in the prediction of the precise onset date and the position.
To evaluate the methods used here, the EOF analysis as well as the clustering led to reasonable results. The EOF showed patterns (e.g. the shift pattern) which were already known from investigations in the medium range. With the clustering, we could find different development scenarios for each forecast. However, the spread within some clusters was quite large, which is attributed to the long lead times in the subseasonal range and also to the small number of members that were clustered. Nevertheless, since the results are physically consistent and consistent with the medium range, we conclude that the EOF and clustering methodology was useful for our investigations of the onset phase of the block in the subseasonal range. A larger ensemble size could increase the reliability of the results.

4.4.2. Forecast Variability during the Decay Phase of the Block

The first forecast was initialized on 9 July, 39 days before the analyzed decay of the blocking system. For this forecast, the ensemble spread was largest over the Pacific in late July and early August (Fig. 4.9, top, left). Around the blocked longitude, the ensemble spread increased at the end of July. In the second forecast with an initialization on 25 July (23 days before the decay) there was again a large ensemble spread over the Pacific (Fig. 4.9, top, right). In addition, the ensemble spread also increased over the Atlantic after 13 August. After the analyzed block's decay, the ensemble spread was quite large between 80°W and 80°E. The third forecast, initialized on 1 August (16 days before decay), showed a similar distribution to the second forecast (Fig. 4.9, bottom), with enhanced ensemble spread over the Pacific,

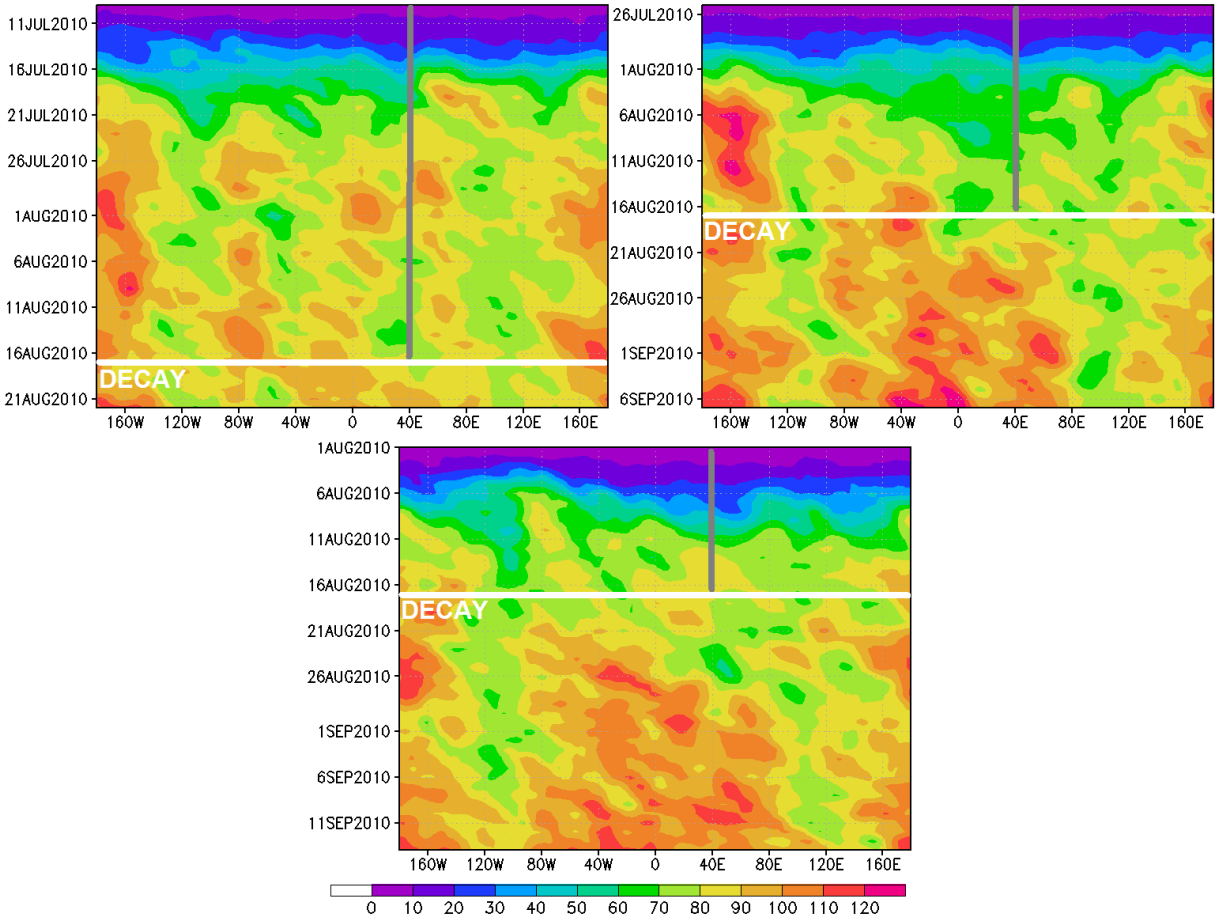

Fig. 4.9.: As in Fig. 4.2, but for the forecasts initialized at 0000 UTC 9 July 2010 (top, left), at 0000 UTC 25 July 2010 (top, right), and at 0000 UTC 1 August 2010 (bottom).

and after 21 August, also between 80°W and 80°E.

Characteristics of the Forecast initialized on 9 July 2010

EOF 1 and EOF 2 represented nearly 36 % of the total variability. EOF 1 captured 20.4 % and was distributed as follows. Positive values of EOF 1 dominated northern areas above 65°N (Fig. 4.10, left, top). Farther south, negative signals could be found at 20°E and 80°E, and a weaker positive signal at 40°E. A member with a positive contribution to EOF 1 showed a ridge at 40°E. In a member with negative contribution, the flow was more zonal. Thus, EOF 1 revealed an amplitude pattern (Anwender et al., 2008). EOF 2 (capturing 15.5 %) had a dipole around 0° (Fig. 4.10, left, bottom). Additionally, there was a negative signal at 100°E. Positively contributing members had a ridge-trough couplet around 0° and a trough at 100°E. The ridges and troughs were transposed for negatively contributing members. The dipole signal is characteristic for a shift pattern (Anwender et al., 2008).

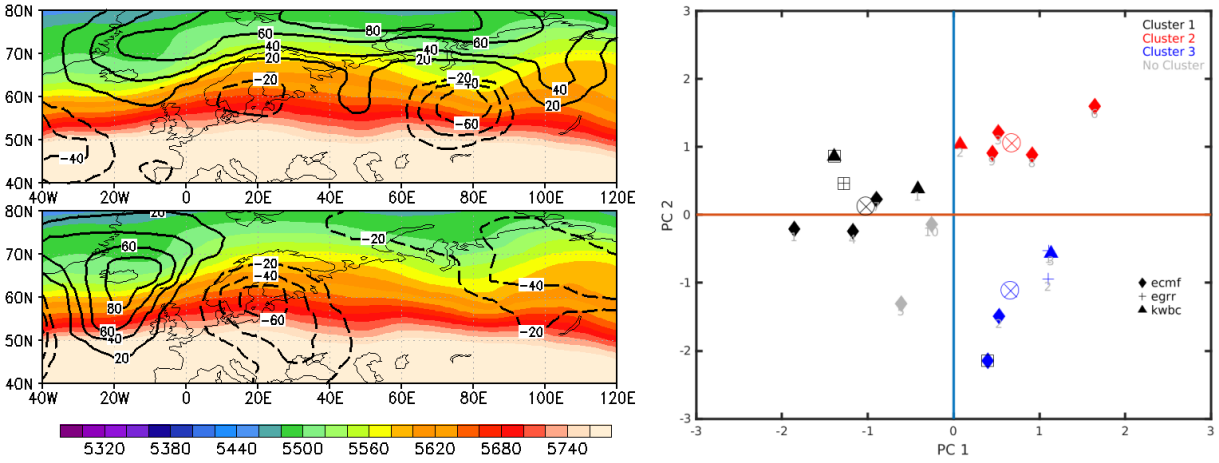

Fig. 4.10.: As in Fig. 4.2, but at +39 days (0000 UTC 17 August 2010) for the forecast initialized at 0000 UTC 9 July 2010.

Cluster 1 consisted of 6 ensemble members, which had a negative contribution to EOF 1 and were on average neutral to EOF 2 (Fig. 4.10, right). Cluster 2 and 3 had each 5 members. Members within cluster 2 had a positive contribution to EOF 2 and almost all had a positive contribution to EOF 1. Except for one member, the members of cluster 2 were close to the cluster center. Members which belonged to cluster 3 had a negative contribution to EOF 2 and a positive one to EOF 1.

The flow structure in the composite of cluster 1 was less amplified and more zonal compared to the representative member, which showed an overturning ridge at 30°E (Fig. 4.11, top). For cluster 2, the representative member and the composite showed a similar flow pattern, except for a ridge at 100°E, which was only visible in the cluster composite (Fig. 4.11, middle). In cluster 3, the wave pattern around 60°N was similar in the composite and the representative member (Fig. 4.11, bottom). At higher latitudes, there were more differences concerning the amplitude and position of the troughs and ridges. Even if details differed, the similarity between the composite and the representative member was still large enough to use the latter for the analysis of the synoptic development in cluster 3.

In scenario 1, there was no blocking ridge anymore on 17 August (Fig. 4.11, top). The decay of the block was forecast already on 18 July (not shown). There was also no block in scenario 2 (Fig. 4.11, middle). Around 20 July, there was a first weakening of the block, then it was again sustained by an amplified ridge propagating from the west. However, the system decayed in early August (not shown). The amplified ridge at 100°E in scenario 3 had nothing to do with the Russian heat wave block (Fig. 4.11, bottom). The block had already decayed on 3 August (not shown).

In summary, in all scenarios the decay of the blocking system was predicted. However, the block's decay always occurred too early. In scenario 1, the temporal discrepancy was about one month. In scenario 2 and 3, the block's decay was two weeks too early.

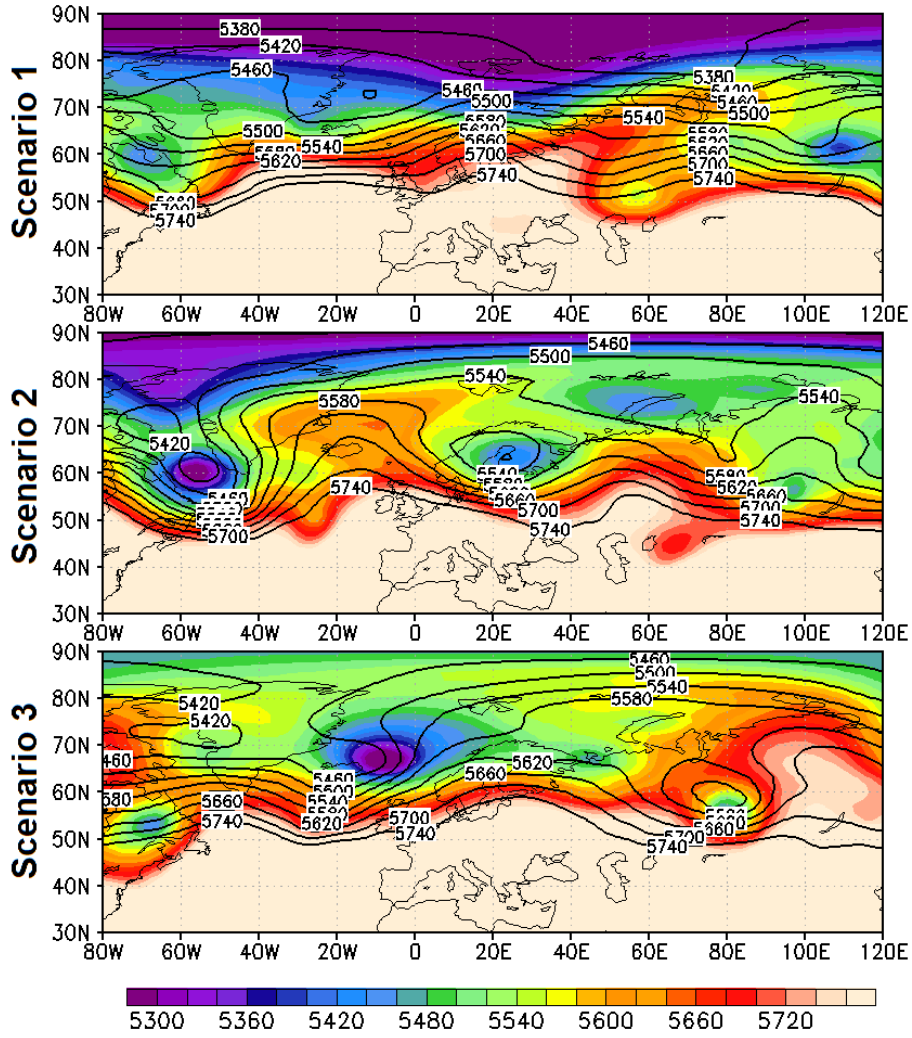

Fig. 4.11.: As in Fig. 4.3, but at +39 days (0000 UTC 17 August 2010) for the forecast initialized at 0000 UTC 9 July 2010.

Characteristics of the Forecast initialized on 25 July 2010

Nearly 43 % of the total variability was captured by EOF 1 and 2. 26.6 % alone was captured by EOF 1. EOF 1 had a dipole at 30°W with negative values to the south and positive values to the north (Fig. 4.12, left, top). Another negative signal extended from 0°/45°N to 120°E/80°N. In addition, a strong positive signal could be found between 50°E and 110°E around the 50th latitudes. This distribution corresponds to a mixture of amplitude and shift pattern (Anwender et al., 2008). Thus, in positively contributing members, a ridge over Europe was shifted to the east and flattened, and in negatively contributing members, it was shifted to the west and enhanced. EOF 2 captured 16.3 % of the variability and was again a mixture of amplitude and shift pattern (Anwender et al., 2008) (Fig. 4.12, left, bottom). At higher latitudes, positive values of EOF 2 were visible. Between 10°W and 40°W, this positive signal extended to lower latitudes. Negative values could be found over Europe around 55°N between 10°W and 120°E. A member with positive contribution to EOF 2 showed high 500 hPa geopotential height at high latitudes

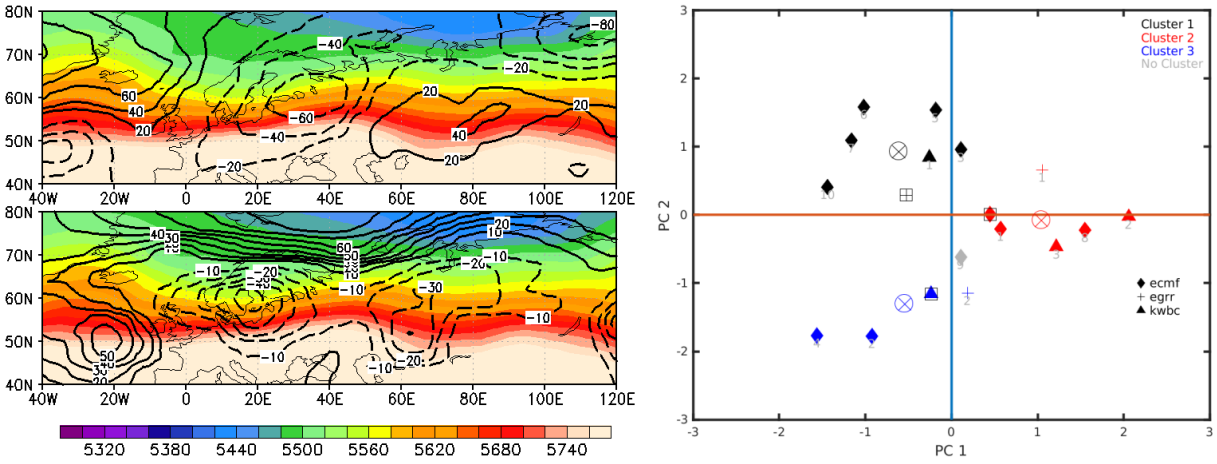

Fig. 4.12.: As in Fig. 4.2, but at +23 days (0000 UTC 17 August 2010) for the forecast initialized at 0000 UTC 25 July 2010.

and an amplified ridge between 10°W and 40°W. A member with negative contribution, had two weak ridges at 20°E and 60°E and a deep trough between 10°W and 40°W. High latitudes were dominated by low values of the geopotential height.

7 members belonged to cluster 1 (Fig. 4.12, right). They contributed positively to EOF 2, and almost all members exhibited a negative contribution to EOF 1. Cluster 2 had 6 members which had a positive contribution to EOF 1 and were more or less neutral to EOF 2. Cluster 3 consisted of 4 members contributing negatively to EOF 1 (except one member) and EOF 2. Only one member could not be assigned to a certain cluster.

The wave pattern in the cluster composites was similar to the corresponding representative members (Fig. 4.13). This means, that the clusters were represented well by the chosen forecast members.

The troughs and ridges in scenario 1 were less amplified (Fig. 4.13, top). The system which blocked the 40th longitude decayed already at the end of July (not shown). In scenario 2, there was a blocking dipole with a southern cyclonic cut-off and northern high geopotential over the Atlantic (Fig. 4.13, middle). Over Europe the flow was zonal and dominated by low 500 hPa geopotential height at high latitudes. The blocking system over the Russian-European sector decayed after 1 August (not shown). In scenario 3, two less amplified ridges were visible at 20°E and 80°E (Fig. 4.13, bottom). The block related to the Russian heat wave lost its intensity already on 1 August (not shown).

In conclusion, there were remarkable differences between the scenarios. However, the Russian heat wave block decayed in all scenarios in early August, that is more than two weeks earlier than observed in the analysis.

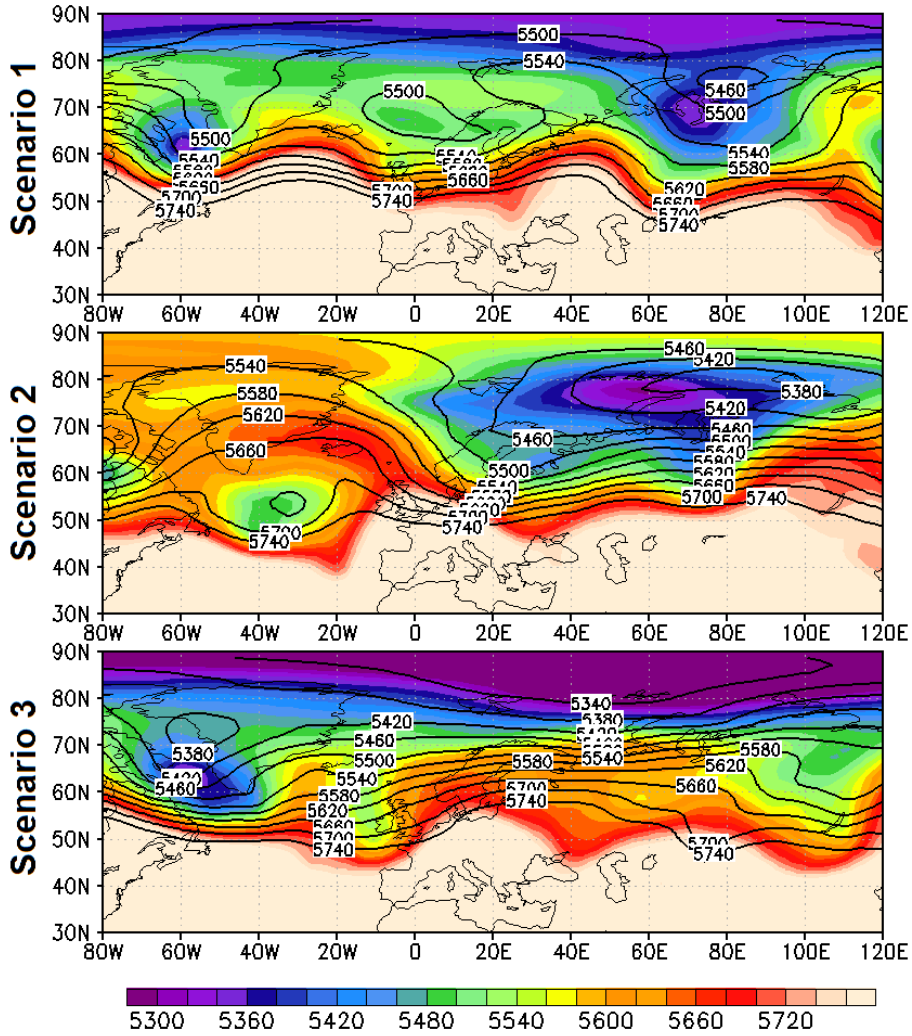

Fig. 4.13.: As in Fig. 4.3, but at +23 days (0000 UTC 17 August 2010) for the forecast initialized at 0000 UTC 25 July 2010.

Characteristics of the Forecast initialized on 1 August 2010

EOF 1 and EOF 2 captured 42 % of the total forecast variability. EOF 1 alone reflected 27.9 % of the variability and was characterized by a dipole along a ridge at 40°E, which corresponded to our blocking event (Fig. 4.14, left, top). As EOF 1 can be interpreted as a shift pattern (Anwender et al., 2008), a positively (negatively) contributing member showed the ridge farther west (east). EOF 2 captured 14.1 % of the variability. A strong negative signal was located at 40°E/60°N (Fig. 4.14, left, bottom). This signal was surrounded by positive values of EOF 2. The distribution of EOF 2 reflected an amplitude pattern (Anwender et al., 2008). At 40°E, a member with positive contribution to EOF 2 had a trough, whereas a member with negative contribution showed a ridge there.

Cluster 1 had 4 members, which had a negative contribution to EOF 1 and a positive one to EOF 2 (Fig. 4.14, right). Cluster 2 consisted of 6 members. They had a negative contribution to EOF 2. Except one member, they were neutral to EOF 1. Cluster 3 had 4 members, which had a positive contribution to

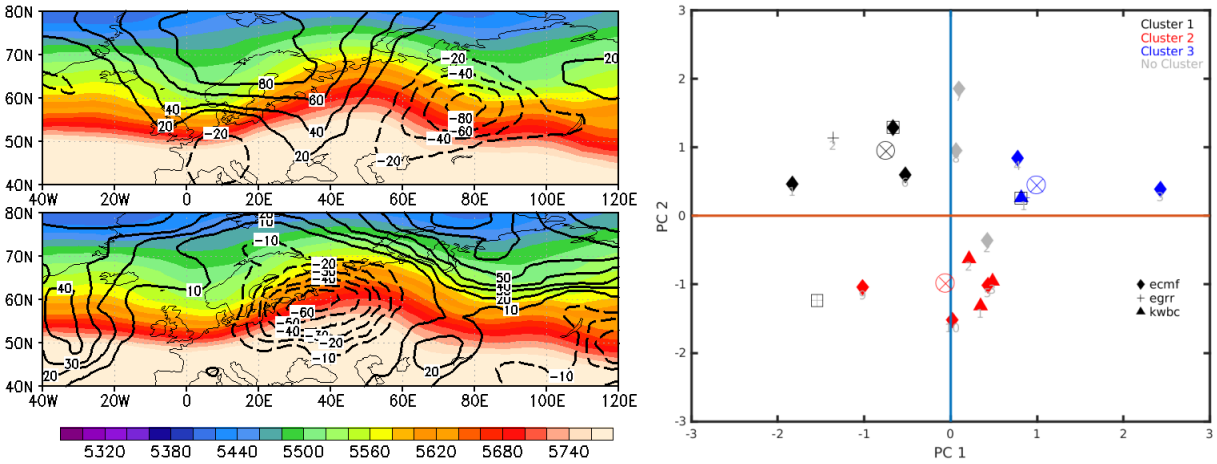

Fig. 4.14.: As in Fig. 4.2, but at +16 days (0000 UTC 17 August 2010) for the forecast initialized at 0000 UTC 1 August 2010.

EOF 2. These members contributed also positively to EOF 1, however, differently in amount. From the 18 members, 4 members could not be assigned to any cluster.

The representative members of cluster 1 and 2 showed flow patterns which were similar to the corresponding cluster composites (Fig. 4.15). The wave pattern of cluster 3 looked different in the composite and the representative member at 50°E and farther east. There was a slight shift of a trough which was farther east in the composite.

In scenario 1, there was a ridge at 70°E without blocking character (Fig. 4.15, top). The Russian heat wave block decayed on 10 August (not shown). In scenario 2, the ridge at 40°E was the residual of the blocking system (Fig. 4.15, middle). At clustering time, the ridge had already lost its blocking characteristics. With the index of Tibaldi and Molteni (1990) the decay of the block was found to be on 10 August (not shown). In scenario 3, the high geopotential at 30°E/70°N remained after poleward wave breaking of the blocking system (Fig. 4.15, bottom). The decay of the block occurred already on 10 August.

In summary, there was agreement in all scenarios that the blocking system decayed on 10 August, one week before it decayed in the analysis.

Discussion

Two of the three forecasts (initialization times were 25 July and 1 August) showed a large ensemble spread at the blocked longitude (40°E) as well as in upstream regions after the analyzed decay (17 August). The other forecast (initialization time was 9 July) did not have a remarkable ensemble spread in vicinity of 40°E.

For all scenarios of all forecasts we found that the block decayed. However, the precise date for the decay varied from forecast to forecast. In the first forecast, initialized on 9 July, the decay of the block was two

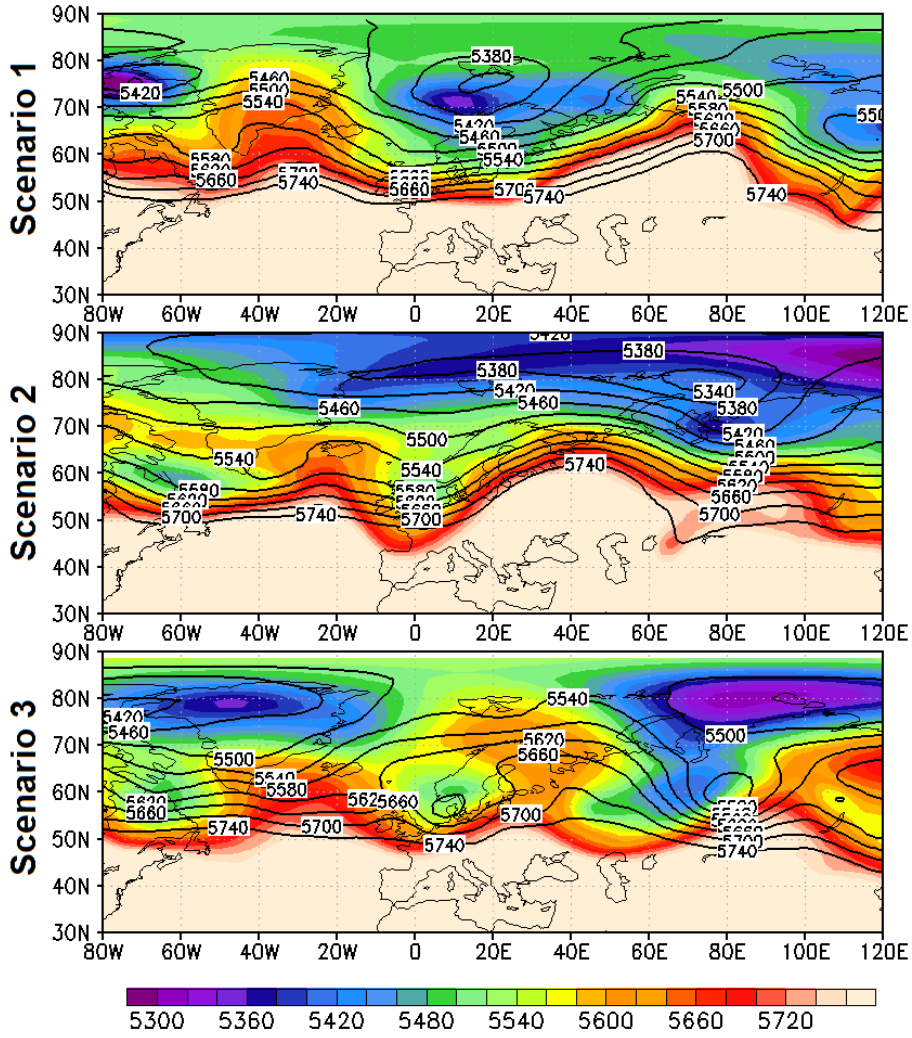

Fig. 4.15.: As in Fig. 4.3, but at +16 days (0000 UTC 17 August 2010) for the forecast initialized at 0000 UTC 1 August 2010.

weeks too early in two scenarios. In the remaining scenario, the block decayed already one month before the analyzed decay date. In the second forecast, initialized on 25 July, the block decayed 2 weeks too early. And in the third forecast, initialized on 1 August, the temporal discrepancy between the predicted and the analyzed decay was about one week in all development scenarios.

In all forecasts, it seemed to be certain that the block will decay. Thus, the major variability at clustering time was not related to the uncertainty as to whether the block will decay or not, but rather to uncertainties in its position and its shape (especially of its flanks). Thus, the block was shown differently in the forecast scenarios. However, its decay occurred regardless of these differences. In the two forecasts whose initialization times were closer to the analyzed decay date there were no differences between the scenarios regarding the decay time. In the forecast whose initialization time was in early July the scenarios did not show a consistent result for the decay of the blocking system. The precise date of the block's decay was captured better for later initialization times. However, there was still a discrepancy of one

week for the forecast initialized on 1 August.
As before for the forecasts which contained the onset of the blocking system, the EOF and clustering methodology produced reasonable results. The EOFs showed patterns consistent with the results of our medium-range analysis and the clustering provided distinct development scenarios.

4.5. Summary and Conclusions

In this chapter, we investigated the forecast variability of the 2010 Euro-Russian summer block in the subseasonal range. For the onset phase and for the decay phase of the block we compared the main development scenarios extracted from three S2S reforecasts for each phase with lead times of up to 45 days. The main scenarios were found using the EOF/clustering methodology, as for the medium range.
For the onset phase, we found that the forecast of the position of the block and its onset date were improved for initialization times closer to the analyzed onset. But the duration of the block was underestimated in most cases. Nevertheless, the evolution of a persistent blocking pattern was predicted over the European-Russian sector in some scenarios taken from forecasts initialized weeks before the analyzed onset. For the forecasts with which we investigated the decay phase of the block we found that their variability was not related to the decay of the blocking system. The blocking system decayed in all scenarios of all forecasts. However, the closer the initialization time was to the analyzed decay time, the better the precise date for the decay was captured.
With respect to the impact on the surface, an underestimated blocking duration leads to an underestimate of the 2 m temperature (Vitart et al., 2014). Since the blocking system was related to a mega heat wave, the results show that the heat wave duration was not captured by most of the scenarios from the 45-day reforecasts. This means that the predictability of the heat wave as well as the predictability of the blocking anticyclone itself were - as expected and already known from the medium range - limited in the subseasonal forecast range. However, it is promising that there were indeed forecast members which predicted the onset of the block more or less correctly, even for these long lead times.
A further aim of our study was to find out if the EOF/clustering methodology can be used with a reduced number of members and with such long lead times. We found that the EOF analysis showed variability patterns which were already familiar from investigations in the medium range, namely the amplitude and the shift pattern (Anwender et al., 2008). The clustering offered development scenarios, which showed large differences. Thus, the diversity of scenarios could be reflected with the clustering. One problem of the method was the spread within some clusters, which was a consequence of the long lead times that were used as clustering times. Since the ensemble spread increases over time, it also increases within the clusters with growing lead times. Regarding the number of members, which was here 18, it was reduced compared to our investigations of the medium range, where we had 96 ensemble members. Since the EOF/clustering routine led to reasonable results, we conclude that the method is suitable for ensemble

(re)forecasts in the subseasonal range. However, more members would give more confidence in the extracted development scenarios.

5. Comparison between both Approaches

We investigated the forecast variability of the 2010 Russian heat wave block in the medium, as well as in the subseasonal range. Since we applied the EOF and clustering analysis to both forecast ranges, we will compare the two approaches. With respect to future studies, we give an outlook on how surface impacts and dynamical features could be investigated in subseasonal forecasts.

For the medium range, we used TIGGE ensemble forecasts consisting of 96 members from three EPS (ECMWF, NCEP, and UKMO, Table 5.1). For the subseasonal range, S2S ensemble reforecasts were used with an ensemble size of only 18 members (Table 5.1). We used reforecasts, since S2S ensemble forecasts having an extended ensemble size are not available for 2010. The S2S reforecasts were taken from the same three EPS as those for the medium range. The different ensemble size is of relevance, since it has an impact on ensemble prediction (Buizza and Palmer, 1998). Depending on the verification method and the types of weather events, an increase of ensemble size can lead to improvements in the EPS performance (Buizza and Palmer, 1998). Consequently, an improved forecast quality of the medium-range forecasts comparing to the subseasonal forecasts could be partly the result of different ensemble sizes. The ensemble size is also of relevance for the validity of the EOF/cluster analysis. More members give more confidence in the results from this analysis.

To investigate the ensemble spread and to extract the main development scenarios from the ensemble, we used an EOF and clustering procedure for both datasets. The first and second EOF showed similar patterns for both forecast ranges, linked to the amplitude and/or shift (Anwender et al., 2008) of the blocking anticyclone or the accompanying troughs. With the clustering methodology, we grouped ensemble members with similar flow configurations, also for both forecast ranges. The resulting representative members of the clusters showed different synoptic situations, revealing that the clustering method worked well to identify the main development scenarios in the ensemble forecasts. For the onset phase for the block, there were scenarios with and without blocking in both ranges. However, for the decay phase of the block in the subseasonal reforecasts used here we found that the major forecast variability was not related to the decay of block itself. The block's extension, amplitude and decay date were indeed different in the scenarios of the subseasonal reforecasts. There was, however, agreement between the ensemble members that the decay would happen in some way. Due to longer lead times, the ensemble spread at clustering time was larger for the subseasonal range, also within the clusters.

Tab. 5.1.: Contrasting juxtaposition of used medium-range and subseasonal forecasts, plus used methods for both forecast ranges.

	medium range	subseasonal range
dataset	TIGGE	S2S
forecast type	forecasts	hindcasts
forecast length	10 days	45 days
time intervals	12 hours	1 day
ensemble size	96 members	18 members
methods	EOF, clustering, ESA, impact indices	EOF, clustering

Considering blockings in the subseasonal forecast range has the advantage that one forecast could contain the whole life-cycle of a block. Medium-range forecasts with lead times of 10 days are only able to predict parts of a block's life-cycle. For short-living blocks with lifetimes around 10 days, the medium range is sufficient. Even if the subseasonal consideration promises that the block's evolution might be fully captured, the problem remains that the onset and the decay phases of the block are challenging for weather prediction models, since they are connected to a change of the flow regime (Tibaldi and Molteni, 1990; Frederiksen et al., 2004). The onset is linked to a change from zonal to meridional flow conditions, while this is reversed during the decay phase of the block (e.g. Arakawa, 1952). If the genesis or lysis of the block is already part of the initial conditions, predictability is typically increased. Regarding only this argument, the extension of the forecast range from the medium range to the subseasonal range does not have an added value. Another point is that some long-living blocks even outlast the subseasonal time scale. We used reforecasts of 45 days, however, the Russian heat wave block lasted nearly 2 months. Thus, the subseasonal reforecasts used here were not long enough to capture the whole life-cycle of the block.

There are, however, other points which make it clear that both ranges can improve our understanding about atmospheric blocking and its predictability. The reason for this is that the two forecast ranges benefit from and are determined by different dynamical interactions. The medium range deals with synoptic systems such as extratropical cyclones (Palmer, 2000). The predictability of the subseasonal range is determined by large-scale interseasonal oscillations, like the NAO or the Madden-Julian Oscillation (Vitart et al., 2016). Atmospheric blocks are an example for the interactions of time and spatial scales. For example, a negative NAO phase provides favorable flow conditions for the evolution of a block (Benedict et al., 2004; Croci-Maspoli et al., 2007b; Woollings et al., 2008). But additional features at a smaller spatial and time scale than the NAO, like diabatic forcing or TE feedback, are necessary for the maintenance of the block. Relevant dynamical features in the medium range were part of this study. One of our results was that Atlantic ARs, which were forced to ascent at the southern coast of Greenland,

provided water for precipitation that led via latent heat release to an upper-level PV anomaly. For the onset phase, this PV anomaly supported an Atlantic precursor block, which changed the flow in such a way that it was favorable for the onset of the Russian heat wave block. Our results were in accordance with previous work (e.g. Shutts, 1983; Schwierz, 2001). Thus, the medium as well as the subseasonal range are important to understand atmospheric blocking and its predictability as a whole.
The need for subseasonal predictions of atmospheric blocking exists also, since blocks might be linked to high impact weather events, such as heat waves, cold spells or flooding (e.g. Green, 1977; Hoskins and Sardeshmukh, 1987; Hong et al., 2011). These events can lead to a large amount of fatalities and to enormous economic losses. For the general public, the government, and especially for emergency managers, it is beneficial and sometimes even lifesaving to know as early as possible if a high impact weather event will happen or not. Thus, a skillful subseasonal forecast of a blocking could help to take precautions early enough to prevent catastrophic conditions or at least to minimize losses. The impact of medium-range blocking variability on the surface conditions was also part of this study. With common heat indices, temperature threshold, and an index for fire potential, we could identify the beginning of the heat wave in connection to the block's onset. In scenarios with blocking, the surface temperatures, heat intensity and fire potential increased. Without blocking, this increase could not be observed. For the decay phase of the block, the heat and fire indices, as well as the temperature thresholds showed the end of the heat wave. There was a forecast scenario in which the block did not decay. Even here the heat wave ended, since the geopotential height anomaly was not in phase with the temperature anomaly anymore, corresponding to a shift of the blocking system.

Most of the studies in which the predictability of atmospheric blocking is investigated used medium-range forecasts or hindcasts. Hamill and Kiladis (2014) used an extensive time series (from 1985 to 2012) of medium-range ensemble reforecasts from NCEP to investigate the skill of northern hemisphere winter blocks. They found that the blocking frequency, as well as the blocking skill vary more or less strongly from year to year. Another key result was that the blocking frequency is underestimated for the Euro-Atlantic sector. Moreover, they found that the onset and decay are characterized by low predictability, in accordance with earlier studies (e.g. Tibaldi and Molteni, 1990). The study of Hamill and Kiladis (2014) is quite different to our study, since they regarded a time series of medium-range forecasts, including a great many blocking events. For lead times longer than a week, Bengtsson (1981) found that improvements in data, parametrization and numerical resolution increase the predictability of blocking systems. Other examples of medium-range predictability studies were those of Pelly and Hoskins (2003a), as well as Matsueda (2009, 2011). Since the S2S dataset has only been established recently, only few studies are available. The S2S dataset was introduced in Brunet et al. (2010) and Vitart et al. (2014, 2016). Vitart et al. (2014) discussed the monthly heat wave prediction in terms of surface feedbacks and large-scale flow conditions. They showed that the skill of monthly forecasts for heat waves is increased if the soil moisture and the upper-level controlling anticyclone are predicted correctly. Thus, it is most

favorable if the block and the soil moisture pattern are included in the initial conditions. An earlier study of Ratcliffe and Murray (1970) showed the potential of monthly forecasts of large-scale circulation patterns by considering sea surface temperature (SST) anomalies, since they found that persistent cold SSTs south of Newfoundland can create favorable conditions for blockings over Europe. Hence, blocking predictability was investigated in the medium as well as in the subseasonal range before. By including both forecast ranges, we presented a new perspective on blocking predictability with this study.

Without a focus on atmospheric blocking, other studies considered more than one forecast range. Palmer (1988) investigated the predictability and stability of the Pacific/North American (PNA) mode in the medium as well as in the extended range. The PNA describes mid-tropospheric geopotential height anomalies and is related to ENSO. For both forecast ranges, he found that the predictive skill depends on fluctuations in the PNA mode. A study of Branstator et al. (1993) also considered the medium and the extended range. They identified predictable and less predictable large-scale flow elements in the extratropics with help of an EOF analysis. Ferranti et al. (1990) discussed the fact that tropical-extratropical interactions have a remarkable effect on medium-range as well as extended range predictions. Consequently, the consideration of both the medium and the subseasonal (or extended) forecast range, within one study was did before, however, without focusing on atmospheric blocking as we did in this study.

In summary, the medium and the subseasonal range are beneficial for investigating the predictability of atmospheric blocking. Since both ranges benefit from different dynamical flow features, both are relevant to understand the evolution of a block as a whole, and are relevant for forecasting purposes. Predictability of blocks was investigated in other studies before (e.g. Pelly and Hoskins, 2003a). In this study, we provide a new perspective on blocking predictability since we compared different forecast ranges directly, and in addition investigated surface impacts and dynamical features of atmospheric blocking.

In future studies, the additional investigations which were only made for the medium range, could be done also for the subseasonal range. The investigation of surface impact can be done with the same indices (for example Humidex), since the input variables are available in the S2S dataset. The ESA was firstly used for investigations in the short forecast range, for example in Torn (2010a). Studies of Chang et al. (2013) showed that it is also suitable for the medium range, corresponding with our study. One could ask if the ESA approach can be also used for subseasonal predictions? Since a time range of 6 days yields consistent results, it is worth considering whether the ESA can help to understand the forecast uncertainties in the subseasonal range, in which large-scale patterns like the NAO also play a role. The most critical issue with ESA for longer ranges is the linearity assumption, which is even less likely to hold at the extended range than in the medium range. In addition, in some of the subseasonal reforecasts, which were discussed in this study, the blocking evolution was represented similarly in all ensemble members. Since a sufficient ensemble spread (regarding the object of study) is required for an ESA, it would not

have worked with those reforecasts. In addition, an ensemble of only 18 members could be too small to get significant results. For further studies, instead of calculating sensitivities for S2S ensembles, it could be examined if the dynamical processes, which we found to be relevant in the medium range, also could be at least partly responsible for the forecast variability in the subseasonal range.

6. Conclusions and Outlook

Atmospheric blocking is an important topic of research, since its predictability is low and it is often linked to high impact weather events. In this study, we addressed blocking predictability by comparing different development scenarios and by investigating surface impacts and relevant dynamical processes. We focused on the Russian heat wave block in summer 2010, since it is a prime example for long-lasting atmospheric blockings and their ability to trigger high impact weather events.

The forecast variability of the summer block over the European-Russian sector in 2010 was investigated in the medium and in the subseasonal forecast range. For the medium range, 10-day TIGGE ensemble forecasts were used. For the subseasonal range, 45-day reforecasts from the S2S database were analyzed. The investigations of the ensemble variability and the extraction of the main development scenarios was done with the help of an EOF analysis and clustering approach. For the medium range, the impact on surface conditions and the responsible dynamical processes and features were investigated also. The surface impacts were discussed in terms of common heat indices, an index for fire risk, and precipitation. The study of dynamics was done with an ensemble sensitivity analysis.

For the medium forecast range, the following conclusions can be made:

- Our investigations for this 2010 blocking event showed that the predictability of the block's decay was lower than that of the block's onset. During the mature stage, the block was forecast in all development scenarios. However, there was a remarkable uncertainty in the representation of the block's western flank.

- The heat and fire risk indices (for example Humidex) computed from surface variables were suitable to investigate the evolution of the heat wave in the ensemble forecasts. The onset (decay) of the heat wave was connected to an increase (decrease) in the impact indices.

- The low predictability of the blocking system transferred to a low predictability of surface variables (2 m temperature and precipitation). Thus, there were remarkable differences in the surface variables between the forecast scenarios.

- In the grid point forecasts, the forecast uncertainty was higher than in the forecasts of the spatial means of the heat indices. This shows the challenge for weather prediction near the grid point scale.

- The ESA approach turned out to be suitable to investigate dynamical processes in medium-range TIGGE forecasts, since the sensitivities were consistent for different variables (for example, geopotential height at 500 hPa, MSLP, and PV at 320 K)

- Different dynamical features dominated the development during the several phases of the block. For the onset of the Russian heat wave block, the evolution of precursor blocks was favorable. During the mature stage and the decay phase of the block, the transient eddy feedback became relevant. In all phases, diabatic forcing over the North Atlantic was important. At upper levels, a negative PV anomaly (corresponding to the blocking system) was created or at least supported by diabatic heating.

For the subseasonal range, we concluded the following:

- It was possible to predict the onset of the blocking system. However, it was difficult to predict the exact date, the right position and duration of the block.

- For shorter lead times, the predictability of the block's onset increased, since the position and the date were captured better.

- The forecast scenarios agreed that the block will decay. However, there were differences in the representation of the block, especially of its flanks. The forecast variability was also determined by other flow features in areas upstream and downstream of the block (such as an Atlantic ridge).

- The EOF and clustering methodology is suitable for investigations in the subseasonal range, since the EOF patterns were similar as for the medium-range forecasts, and the extracted scenarios showed different developments.

In the light of the current predictable range, it could make sense to combine both approaches. Medium-range as well as subseasonal forecasts are necessary to improve our understanding of the relevant dynamical processes which influence blocking genesis, maintenance and lysis. In both ranges, the predictability is low during the onset and the decay phase of the block. If a blocking system is already captured in the initial conditions, the subseasonal range provides a better opportunity to show the whole life-cycle of the system. However, for short-lived blocks, the medium range can be long enough.

We presented a complete picture of the predictability of the 2010 Russian heat wave block in the medium forecast range in terms of the forecast variability of the blocking system itself, the impact of the block's variability on surface variables, and the dynamics that caused the variability. Since this is a case study, our findings are not necessarily applicable to all other blocking events. Some of the results could indicate aspects which are generally valid for blocks. Further studies could build on our results of the forecast variability in the subseasonal range, since there are still open questions regarding the surface impacts of

the forecast variability and the responsible dynamics.

The subseasonal forecast range is an underexplored area, since the S2S dataset is new. Our investigations of the forecast variability of the 2010 Russian heat wave block scratches only the surface of blocking predictability in the subseasonal range. Therefore, further studies could address the dynamical processes which caused the forecast variability of the block or the impact on predictability of surface variables. Moreover, independent of the forecast range, the concept which was presented in this study for the 2010 Russian heat wave block could be used for investigations of other blocking events. This is not just limited to case studies. Indeed, a statistical analysis of many blocking events could help to find more generally valid coherences between forecast variability, surface impacts, and dynamics of blocking systems.

A. List of Symbols

a	growth rate
B	surface heat flux
c_p	specific heat capacity
D	transient eddy flux
e	vapor pressure
$\vec{e}$	eigenvector
E	latent heat flux
$[E]$	eigenvector matrix
η	vertical component of absolute vorticity
$\vec{F}$	friction
g	gravity acceleration
H	sensible heat flux
$K\downarrow$	global radiation
$K\uparrow$	reflected shortwave radiation
$L\downarrow$	counterradiation
$L\uparrow$	emitted longwave radiation
ω	vertical velocity in pressure coordinates
p	pressure
Φ	latitude
Ψ	stream function
PV	potential vorticity
q	relative humidity
Q	radiation balance
R	gas constant
RH	specific humidity
ρ	density
σ	standard deviation
t	time
T	temperature
τ	dew point
θ	potential temperature

u	zonal wind component
$\vec{u}$	data vector
v	meridional wind component
$\vec{v}$	wind vector
ε	root mean square average forecast
ϑ	temperature
$\vec{x}'$	anomaly vector
Z	geopotential height
ζ	relative vorticity

B. List of Abbreviations

AR	Atmospheric River
AWB	Anticyclonic Wave Breaking
CBL	Central Blocking Latitude
CWB	Cyclonic Wave Breaking
DWD	Deutscher Wetterdienst
EC	Environment Canada
ECMWF	European Centre for Medium-Range Weather Forecasts
EOF	Empirical Orthogonal Function
EPS	Ensemble Prediction System
ERA	ECMWF Re-Analysis
ESA	Ensemble Sensitivity Analysis
ESWD	European Severe Weather Database
GPCC	Global Precipitation Climatology Centre
HI	Heat Index
LASI	Lower Atmospheric Stability Index
LC1	Anticyclonic equatorward RWB
LC2	Cyclonic equatorward RWB
MSLP	Mean Sea Level Pressure
NAO	North Atlantic Oscillation
NCEP	National Centers for Environmental Prediction
P1	Cyclonic poleward RWB
P2	Anticyclonic poleward RWB
PC	Principle Component
PCA	Principle Component Analysis
PNA	Pacific/North American
PV	Potential Vorticity
PVU	Potential Vorticity Unit
ROC	Relative Operating Characteristic
RWB	Rossby Wave Breaking
S2S	Subseasonal to Seasonal
SAM	Selective Absorption Mechanism

SST	Sea Surface Temperature
TE	Transient Eddy
TIGGE	THORPEX Interactive Grand Global Ensemble
UKMO	Met Office
UTC	Coordinated Universal Time
WCB	Warm Conveyor Belt
WMO	World Meteorological Organization

C. Bibliography

Anwender, D., P. A. Harr, and S. C. Jones, 2008: Predictability associated with the downstream impacts of the extratropical transition of tropical cyclones: Case studies. *Monthly Weather Review*, **136 (9)**, 3226–3247.

Arakawa, H., 1952: Kinematics of Meandering and Blocking Action of the Westerlies. *Papers in Meteorology and Geophysics*, **3 (1)**, 12–18.

Athanasopoulou, E., D. Rieger, C. Walter, H. Vogel, A. Karali, M. Hatzaki, E. Gerasopoulos, B. Vogel, C. Giannakopoulos, M. Gratsea, et al., 2014: Fire risk, atmospheric chemistry and radiative forcing assessment of wildfires in eastern Mediterranean. *Atmospheric Environment*, **95**, 113–125.

Barnes, E. A., J. Slingo, and T. Woollings, 2012: A methodology for the comparison of blocking climatologies across indices, models and climate scenarios. *Climate dynamics*, **38 (11-12)**, 2467–2481.

Barriopedro, D., E. M. Fischer, J. Luterbacher, R. M. Trigo, and R. García-Herrera, 2011: The hot summer of 2010: redrawing the temperature record map of Europe. *Science*, **332 (6026)**, 220–224.

Benedict, J. J., S. Lee, and S. B. Feldstein, 2004: Synoptic view of the North Atlantic oscillation. *Journal of the atmospheric sciences*, **61 (2)**, 121–144.

Bengtsson, L., 1981: Numerical prediction of atmospheric blocking—A case study. *Tellus*, **33 (1)**, 19–42.

Berggren, R., B. Bolin, and C.-G. Rossby, 1949: An Aerological Study of Zonal Motion, its Perturbations and Break-down. *Tellus*, **1 (2)**, 14–37.

Björnsson, H. and S. Venegas, 1997: A manual for EOF and SVD analyses of climatic data. *CCGCR Report*, **97 (1)**, 112–134.

Black, E., M. Blackburn, G. Harrison, B. Hoskins, and J. Methven, 2004: Factors contributing to the summer 2003 European heatwave. *Weather*, **59 (8)**, 217–223.

Bougeault, P., Z. Toth, C. Bishop, B. Brown, D. Burridge, D. H. Chen, B. Ebert, M. Fuentes, T. M. Hamill, K. Mylne, et al., 2010: The THORPEX interactive grand global ensemble. *Bulletin of the American Meteorological Society*, **91 (8)**, 1059–1072.

Bowler, N. E. and K. R. Mylne, 2009: Ensemble transform Kalman filter perturbations for a regional ensemble prediction system. *Quarterly Journal of the Royal Meteorological Society*, **135 (640)**, 757–766.

Branstator, G., A. Mai, and D. Baumhefner, 1993: Identification of highly predictable flow elements for spatial filtering of medium- and extended-range numerical forecasts. *Monthly weather review*, **121 (6)**, 1786–1802.

Brotak, E. A., 1991: Low-level temperature, moisture and wind profiles preceding major wildland fires. *Proceedings Eleventh Conference on Fire and Forest Meteorology April*, 16–19.

Brunet, G., M. Shapiro, B. Hoskins, M. Moncrieff, R. Dole, G. N. Kiladis, B. Kirtman, A. Lorenc, B. Mills, R. Morss, et al., 2010: Collaboration of the weather and climate communities to advance subseasonal-to-seasonal prediction. *Bulletin of the American Meteorological Society*, **91 (10)**, 1397–1406.

Buehler, T., C. C. Raible, and T. F. Stocker, 2011: The relationship of winter season North Atlantic blocking frequencies to extreme cold or dry spells in the ERA-40. *Tellus A*, **63 (2)**, 212–222.

Buizza, R. and T. N. Palmer, 1998: Impact of ensemble size on ensemble prediction. *Monthly Weather Review*, **126 (9)**, 2503–2518.

Cattiaux, J., R. Vautard, C. Cassou, P. Yiou, V. Masson-Delmotte, and F. Codron, 2010: Winter 2010 in Europe: a cold extreme in a warming climate. *Geophysical Research Letters*, **37 (20)**.

Chang, E. K., M. Zheng, and K. Raeder, 2013: Medium-range ensemble sensitivity analysis of two extreme Pacific extratropical cyclones. *Monthly Weather Review*, **141 (1)**, 211–231.

Charney, J. G. and J. G. DeVore, 1979: Multiple flow equilibria in the atmosphere and blocking. *Journal of the atmospheric sciences*, **36 (7)**, 1205–1216.

Chen, W. Y. and H.-m. H. Juang, 1992: Effects of transient eddies on blocking flows: General circulation model experiments. *Monthly weather review*, **120 (5)**, 787–801.

Choi, G., J. Kim, and M. Won, 2006: Spatial patterns and temporal variability of the Haines index related to the wildland fire growth potential over the Korean Peninsula. *Journal of the Korean Geographical Society*, **41 (2)**, 168–187.

Croci-Maspoli, M., C. Schwierz, and H. Davies, 2007a: A multifaceted climatology of atmospheric blocking and its recent linear trend. *Journal of climate*, **20 (4)**, 633–649.

Croci-Maspoli, M., C. Schwierz, and H. C. Davies, 2007b: Atmospheric blocking: space-time links to the NAO and PNA. *Climate dynamics*, **29 (7-8)**, 713–725.

Crum, F. X. and D. F. Stevens, 1988: A case study of atmospheric blocking using isentropic analysis. *Monthly weather review*, **116 (1)**, 223–241.

D'Andrea, F., S. Tibaldi, M. Blackburn, G. Boer, M. Déqué, M. Dix, B. Dugas, L. Ferranti, T. Iwasaki, A. Kitoh, et al., 1998: Northern hemisphere atmospheric blocking as simulated by 15 atmospheric general circulation models in the period 1979–1988. *Climate Dynamics*, **14 (6)**, 385–407.

Davis, R. E., D. Knight, D. Hondula, and P. C. Knappenberger, 2006: A comparison of biometeorological comfort indices and human mortality during heat waves in the United States. *17th Conference on Biometeorology and Aerobiology*.

DelSole, T., 2004: Predictability and information theory. Part I: Measures of predictability. *Journal of the atmospheric sciences*, **61 (20)**, 2425–2440.

Diaconescu, E. P. and R. Laprise, 2012: Singular vectors in atmospheric sciences: A review. *Earth-Science Reviews*, **113 (3)**, 161–175.

Dole, R., M. Hoerling, J. Perlwitz, J. Eischeid, P. Pegion, T. Zhang, X.-W. Quan, T. Xu, and D. Murray, 2011: Was there a basis for anticipating the 2010 Russian heat wave? *Geophysical Research Letters*, **38 (6)**.

Dotzek, N., P. Groenemeijer, B. Feuerstein, and A. M. Holzer, 2009: Overview of ESSL's severe convective storms research using the European Severe Weather Database ESWD. *Atmospheric research*, **93 (1)**, 575–586.

Eckhardt, S., A. Stohl, H. Wernli, P. James, C. Forster, and N. Spichtinger, 2004: A 15-year climatology of warm conveyor belts. *Journal of climate*, **17 (1)**, 218–237.

Egger, J., 1978: Dynamics of blocking highs. *Journal of the Atmospheric Sciences*, **35 (10)**, 1788–1801.

Ertel, H., 1942: Ein neuer hydrodynamischer Wirbelsatz. *Meteorol. Z.*, **59**, 277–281.

Ferranti, L., T. Palmer, F. Molteni, and E. Klinker, 1990: Tropical-extratropical interaction associated with the 30–60 day oscillation and its impact on medium and extended range prediction. *Journal of the Atmospheric Sciences*, **47 (18)**, 2177–2199.

Fink, A. H., T. Brücher, A. Krüger, G. C. Leckebusch, J. G. Pinto, and U. Ulbrich, 2004: The 2003 European summer heatwaves and drought–synoptic diagnosis and impacts. *Weather*, **59 (8)**, 209–216.

Frederiksen, J. S., M. A. Collier, and A. B. Watkins, 2004: Ensemble prediction of blocking regime transitions. *Tellus A*, **56 (5)**, 485–500.

Gabriel, A. and D. Peters, 2008: A diagnostic study of different types of Rossby wave breaking events in the northern extratropics. *Journal of the Meteorological Society of Japan*, **86 (5)**, 613–631.

Gasparrini, A., Y. Guo, M. Hashizume, E. Lavigne, A. Zanobetti, J. Schwartz, A. Tobias, S. Tong, J. Rocklöv, B. Forsberg, et al., 2015: Mortality risk attributable to high and low ambient temperature: a multicountry observational study. *The Lancet*, **386 (9991)**, 369–375.

Grams, C. M., H. Binder, S. Pfahl, N. Piaget, and H. Wernli, 2014: Atmospheric processes triggering the central European floods in June 2013. *Natural Hazards and Earth System Sciences*, **14 (7)**, 1691–1702.

Green, J., 1977: The weather during July 1976: Some dynamical considerations of the drought. *Weather*, **32 (4)**, 120–126.

Grumm, R. H., 2011: The central European and Russian heat event of July-August 2010. *Bulletin of the American Meteorological Society*, **92 (10)**, 1285.

Haines, D. A., 1988: A lower atmosphere severity index for wildlife fires. *Nat. Weather Dig.*, **13 (2)**, 23–27.

Hamill, T. M. and G. N. Kiladis, 2014: Skill of the MJO and Northern Hemisphere blocking in GEFS medium-range reforecasts. *Monthly Weather Review*, **142 (2)**, 868–885.

Hamill, T. M., S. L. Mullen, C. Snyder, D. P. Baumhefner, and Z. Toth, 2000: Ensemble forecasting in the short to medium range: Report from a workshop. *Bulletin of the American Meteorological Society*, **81 (11)**, 2653–2664.

Hamill, T. M., J. S. Whitaker, and S. L. Mullen, 2006: Reforecasts: An important dataset for improving weather predictions. *Bulletin of the American Meteorological Society*, **87 (1)**, 33–46.

Harr, P. A., D. Anwender, and S. C. Jones, 2008: Predictability associated with the downstream impacts of the extratropical transition of tropical cyclones: Methodology and a case study of Typhoon Nabi (2005). *Monthly Weather Review*, **136 (9)**, 3205–3225.

Hong, C.-C., H.-H. Hsu, N.-H. Lin, and H. Chiu, 2011: Roles of European blocking and tropical-extratropical interaction in the 2010 Pakistan flooding. *Geophysical Research Letters*, **38 (13)**.

Hoskins, B. J., M. McIntyre, and A. W. Robertson, 1985: On the use and significance of isentropic potential vorticity maps. *Quarterly Journal of the Royal Meteorological Society*, **111 (470)**, 877–946.

Hoskins, B. J. and P. D. Sardeshmukh, 1987: A Diagnostic Study of the Dynamics of the Northern Hemisphere Winter of 1985-86. *Quarterly Journal of the Royal Meteorological Society*, **113 (477)**, 759–778.

Houze Jr, R., K. Rasmussen, S. Medina, S. Brodzik, and U. Romatschke, 2011: Anomalous atmospheric events leading to the summer 2010 floods in Pakistan. *Bulletin of the American Meteorological Society*, **92 (3)**, 291.

James, I. N., 1995: *Introduction to circulating atmospheres*. Cambridge University Press.

Kalnay, E., 2003: *Atmospheric Modeling, Data Assimilation and Predictability*. Cambridge University Press, URL `https://books.google.de/books?id=Uqc7zC7NULMC`.

Kang, I.-S., J.-S. Kug, M.-J. Lim, and D.-H. Choi, 2011: Impact of transient eddies on extratropical seasonal-mean predictability in DEMETER models. *Climate dynamics*, **37 (3-4)**, 509–519.

Keller, J., S. Jones, J. Evans, and P. Harr, 2011: Characteristics of the TIGGE multimodel ensemble prediction system in representing forecast variability associated with extratropical transition. *Geophysical Research Letters*, **38 (12)**.

Keller, J. H., 2017: Amplification of the Downstream Wave Train during Extratropical Transition: Sensitivity Studies. *Monthly Weather Review*, **(2017)**.

Kikuchi, Y., 1971: Influence of mountains and land-sea distribution on blocking action. *Journal of the Meteorological Society of Japan. Ser. II*, **49**, 564–572.

Koppe, C., S. Kovats, G. Jendritzky, B. Menne, et al., 2004: Heat-waves: risks and responses. Health and Global Environmental Change Series, no. 2. *World Health Organization*.

Kraus, H., 2004: *Die Atmosphäre der Erde*. Springer Berlin Heidelberg.

———, 2008: *Grundlagen der Grenzschicht-Meteorologie*. Springer Berlin Heidelberg.

Kunkel, K. E., R. A. Pielke Jr, and S. A. Changnon, 1999: Temporal fluctuations in weather and climate extremes that cause economic and human health impacts: A review. *Bulletin of the American Meteorological Society*, **80 (6)**, 1077–1098.

Kuo, H.-L., 1953: On the production of mean zonal currents in the atmosphere by large disturbances. *Tellus*, **5 (4)**, 475–493.

Lau, N.-C., 1979: The observed structure of tropospheric stationary waves and the local balances of vorticity and heat. *Journal of the Atmospheric Sciences*, **36 (6)**, 996–1016.

Lau, W. K. and K.-M. Kim, 2012: The 2010 Pakistan flood and Russian heat wave: Teleconnection of hydrometeorological extremes. *Journal of Hydrometeorology*, **13 (1)**, 392–403.

Lavers, D. A. and G. Villarini, 2013: The nexus between atmospheric rivers and extreme precipitation across Europe. *Geophysical Research Letters*, **40 (12)**, 3259–3264.

Lavers, D. A., G. Villarini, R. P. Allan, E. F. Wood, and A. J. Wade, 2012: The detection of atmospheric rivers in atmospheric reanalyses and their links to British winter floods and the large-scale climatic circulation. *Journal of Geophysical Research: Atmospheres*, **117 (D20)**.

Lejenäs, H. and H. Økland, 1983: Characteristics of Northern Hemisphere blocking as determined from a long time series of observational data. *Tellus A: Dynamic Meteorology and Oceanography*, **35 (5)**, 350–362.

Leutbecher, M. and T. N. Palmer, 2008: Ensemble forecasting. *Journal of Computational Physics*, **227 (7)**, 3515–3539.

Liu, Q., 1994: On the definition and persistence of blocking. *Tellus A*, **46 (3)**.

Lorenz, E. N., 1963: Deterministic nonperiodic flow. *Journal of the atmospheric sciences*, **20 (2)**, 130–141.

———, 1965: A study of the predictability of a 28-variable atmospheric model. *Tellus*, **17 (3)**, 321–333.

———, 1969: The predictability of a flow which possesses many scales of motion. *Tellus*, **21 (3)**, 289–307.

Luo, D., F. Huang, and Y. Diao, 2001: Interaction between antecedent planetary-scale envelope soliton blocking anticyclone and synoptic-scale eddies: Observations and theory. *Journal of Geophysical Research: Atmospheres*, **106 (D23)**, 31 795–31 815.

Lynch, P., 2008: The origins of computer weather prediction and climate modeling. *Journal of Computational Physics*, **227 (7)**, 3431–3444.

Madonna, E., H. Wernli, H. Joos, and O. Martius, 2014: Warm conveyor belts in the ERA-interim dataset (1979–2010). Part I: Climatology and potential vorticity evolution. *Journal of Climate*, **27 (1)**, 3–26.

Magnusson, L., M. Leutbecher, and E. Källén, 2008: Comparison between singular vectors and breeding vectors as initial perturbations for the ECMWF ensemble prediction system. *Monthly Weather Review*, **136 (11)**, 4092–4104.

Mahlman, J., 1979: Structure and interpretation of blocking anticyclones as simulated in a GFDL general circulation model. *Proceedings of the Thirteenth Stanstead Seminar, Publication in Meteorology N*, 70–76.

Martius, O., H. Sodemann, H. Joos, S. Pfahl, A. Winschall, M. Croci-Maspoli, M. Graf, E. Madonna, B. Mueller, S. Schemm, et al., 2013: The role of upper-level dynamics and surface processes for the Pakistan flood of July 2010. *Quarterly Journal of the Royal Meteorological Society*, **139 (676)**, 1780–1797.

Masato, G., B. Hoskins, and T. J. Woollings, 2012: Wave-breaking characteristics of midlatitude blocking. *Quarterly Journal of the Royal Meteorological Society*, **138 (666)**, 1285–1296.

Masato, G., B. J. Hoskins, and T. Woollings, 2013: Wave-breaking characteristics of Northern Hemisphere winter blocking: A two-dimensional approach. *Journal of Climate*, **26 (13)**, 4535–4549.

Masih, I., S. Maskey, F. Mussá, and P. Trambauer, 2014: A review of droughts on the African continent: a geospatial and long-term perspective. *Hydrology and Earth System Sciences*, **18 (9)**, 3635.

Masterton, J. and F. Richardson, 1979: *Humidex: a method of quantifying human discomfort due to excessive heat and humidity*. Canada. Service de l'environnement atmosphérique, Downsview, Ont.: Atmospheric Environment.

Matsueda, M., 2009: Blocking predictability in operational medium-range ensemble forecasts. *Sola*, **5**, 113–116.

———, 2011: Predictability of Euro-Russian blocking in summer of 2010. *Geophysical Research Letters*, **38 (6)**.

McCaw, L., P. Marchetti, G. Elliott, and G. Reader, 2007: Bushfire weather climatology of the Haines index in southwestern Australia. *Australian Meteorological Magazine*, **56 (2)**.

McIntyre, M. E. and T. Palmer, 1983: Breaking planetary waves in the stratosphere. *Nature*, **305 (5935)**, 593–600.

McWilliams, J. C., 1980: An application of equivalent modons to atmospheric blocking. *Dynamics of Atmospheres and Oceans*, **5 (1)**, 43–66.

Mori, M., M. Watanabe, H. Shiogama, J. Inoue, and M. Kimoto, 2014: Robust Arctic sea-ice influence on the frequent Eurasian cold winters in past decades. *Nature Geoscience*, **7 (12)**, 869–873.

Mullen, S. L., 1987: Transient eddy forcing of blocking flows. *Journal of the atmospheric sciences*, **44 (1)**, 3–22.

Murphy, J., 1988: The impact of ensemble forecasts on predictability. *Quarterly Journal of the Royal Meteorological Society*, **114 (480)**, 463–493.

Nakamura, H. and J. M. Wallace, 1993: Synoptic behavior of baroclinic eddies during the blocking onset. *Monthly weather review*, **121 (7)**, 1892–1903.

Neiman, P. J., F. M. Ralph, G. A. Wick, J. D. Lundquist, and M. D. Dettinger, 2008: Meteorological characteristics and overland precipitation impacts of atmospheric rivers affecting the West Coast of North America based on eight years of SSM/I satellite observations. *Journal of Hydrometeorology*, **9 (1)**, 22–47.

Otto, F. E., N. Massey, G. Oldenborgh, R. Jones, and M. Allen, 2012: Reconciling two approaches to attribution of the 2010 Russian heat wave. *Geophysical Research Letters*, **39 (4)**.

Palmer, T., 1988: Medium and extended range predictability and stability of the Pacific/North American mode. *Quarterly Journal of the Royal Meteorological Society*, **114 (481)**, 691–713.

Palmer, T. N., 2000: Predicting uncertainty in forecasts of weather and climate. *Reports on Progress in Physics*, **63 (2)**, 71.

Park, Y.-Y., R. Buizza, and M. Leutbecher, 2008: TIGGE: Preliminary results on comparing and combining ensembles. *Quarterly Journal of the Royal Meteorological Society*, **134 (637)**, 2029–2050.

Pelly, J. L. and B. J. Hoskins, 2003a: How well does the ECMWF Ensemble Prediction System predict blocking? *Quarterly Journal of the Royal Meteorological Society*, **129 (590)**, 1683–1702.

———, 2003b: A new perspective on blocking. *Journal of the atmospheric sciences*, **60 (5)**, 743–755.

Péré, J., B. Bessagnet, M. Mallet, F. Waquet, I. Chiapello, F. Minvielle, V. Pont, and L. Menut, 2014: Direct radiative effect of the Russian wildfires and its impact on air temperature and atmospheric dynamics during August 2010. *Atmospheric Chemistry and Physics*, **14 (4)**, 1999–2013.

Pfahl, S., C. Schwierz, M. Croci-Maspoli, C. M. Grams, and H. Wernli, 2015: Importance of latent heat release in ascending air streams for atmospheric blocking. *Nature Geoscience*, **8 (8)**, 610–614.

Potter, B. E., J. A. Winkler, D. F. Wilhelm, R. P. Shadbolt, and X. Bian, 2008: Computing the low-elevation variant of the Haines index for fire weather forecasts. *Weather and Forecasting*, **23 (1)**, 159–167.

Quandt, L.-A., J. H. Keller, O. Martius, and S. C. Jones, 2017: Forecast Variability of the Blocking System over Russia in Summer 2010 and Its Impact on Surface Conditions. *Weather and Forecasting*, **32 (1)**, 61–82.

Rahmstorf, S. and D. Coumou, 2011: Increase of extreme events in a warming world. *Proceedings of the National Academy of Sciences*, **108 (44)**, 17 905–17 909.

Ralph, F. and M. Dettinger, 2011: Storms, floods, and the science of atmospheric rivers. *Eos*, **92 (32)**, 265–266.

Rand, W. M., 1971: Objective criteria for the evaluation of clustering methods. *Journal of the American Statistical association*, **66 (336)**, 846–850.

Ratcliffe, R. and R. Murray, 1970: New lag associations between North Atlantic sea temperature and European pressure applied to long-range weather forecasting. *Quarterly Journal of the Royal Meteorological Society*, **96 (408)**, 226–246.

Rex, D. F., 1950: Blocking action in the middle troposphere and its effect upon regional climate. *Tellus*, **2 (4)**, 275–301.

Riviere, G. and I. Orlanski, 2007: Characteristics of the Atlantic storm-track eddy activity and its relation with the North Atlantic Oscillation. *Journal of the Atmospheric Sciences*, **64 (2)**, 241–266.

Robine, J.-M., S. L. K. Cheung, S. Le Roy, H. Van Oyen, C. Griffiths, J.-P. Michel, and F. R. Herrmann, 2008: Death toll exceeded 70,000 in Europe during the summer of 2003. *Comptes rendus biologies*, **331 (2)**, 171–178.

Robinson, P. J., 2001: On the definition of a heat wave. *Journal of applied Meteorology*, **40 (4)**, 762–775.

Rodwell, M. J. and F. J. Doblas-Reyes, 2006: Medium-range, monthly, and seasonal prediction for Europe and the use of forecast information. *Journal of Climate*, **19 (23)**, 6025–6046.

Scaife, A. A., T. Woollings, J. Knight, G. Martin, and T. Hinton, 2010: Atmospheric blocking and mean biases in climate models. *Journal of Climate*, **23 (23)**, 6143–6152.

Schamm, K., M. Ziese, A. Becker, P. Finger, A. Meyer-Christoffer, B. Rudolf, and U. Schneider, 2013: First Guess Daily Product at 1.0 deg.: Near Real-Time First Guess daily Land-Surface Precipitation from Rain-Gauges based on SYNOP Data.

Schneidereit, A., S. Schubert, P. Vargin, F. Lunkeit, X. Zhu, D. H. Peters, and K. Fraedrich, 2012: Large-scale flow and the long-lasting blocking high over Russia: summer 2010. *Monthly Weather Review*, **140 (9)**, 2967–2981.

Schwierz, C., M. Croci-Maspoli, and H. Davies, 2004: Perspicacious indicators of atmospheric blocking. *Geophysical research letters*, **31 (6)**.

Schwierz, C. B., 2001: Interactions of Greenland-scale orography and extra-tropical synoptic-scale flow. Ph.D. thesis, ETH Zürich.

Shutts, G., 1983: The propagation of eddies in diffluent jetstreams: Eddy vorticity forcing of 'blocking' flow fields. *Quarterly Journal of the Royal Meteorological Society*, **109 (462)**, 737–761.

Sillmann, J., M. Croci-Maspoli, M. Kallache, and R. W. Katz, 2011: Extreme cold winter temperatures in Europe under the influence of North Atlantic atmospheric blocking. *Journal of Climate*, **24 (22)**, 5899–5913.

Simmons, A. J. and A. Hollingsworth, 2002: Some aspects of the improvement in skill of numerical weather prediction. *Quarterly Journal of the Royal Meteorological Society*, **128 (580)**, 647–677.

Slingo, J., S. Belcher, A. Scaife, M. McCarthy, A. Saulter, K. McBeath, A. Jenkins, C. Huntingford, T. Marsh, J. Hannaford, et al., 2014: The recent storms and floods in the UK.

Sodemann, H. and A. Stohl, 2013: Moisture origin and meridional transport in atmospheric rivers and their association with multiple cyclones. *Monthly Weather Review*, **141 (8)**, 2850–2868.

Steadman, R. G., 1979: The assessment of sultriness. Part I: A temperature-humidity index based on human physiology and clothing science. *Journal of Applied Meteorology*, **18 (7)**, 861–873.

Stefanon, M., F. D'Andrea, and P. Drobinski, 2012: Heatwave classification over Europe and the Mediterranean region. *Environmental Research Letters*, **7 (1)**, 014 023.

Stensrud, D. J., H. E. Brooks, J. Du, M. S. Tracton, and E. Rogers, 1999: Using ensembles for short-range forecasting. *Monthly Weather Review*, **127 (4)**, 433–446.

Strong, C. and G. Magnusdottir, 2008: Tropospheric Rossby wave breaking and the NAO/NAM. *Journal of the atmospheric sciences*, **65 (9)**, 2861–2876.

Sumner, E., 1954: A study of blocking in the Atlantic-European of the northern hemisphere. *Quarterly Journal of the Royal Meteorological Society*, **80 (345)**, 402–416.

Swinbank, R., M. Kyouda, P. Buchanan, L. Froude, T. M. Hamill, T. D. Hewson, J. H. Keller, M. Matsueda, J. Methven, F. Pappenberger, et al., 2016: The TIGGE project and its achievements. *Bulletin of the American Meteorological Society*, **97 (1)**, 49–67.

Thorncroft, C., B. Hoskins, and M. McIntyre, 1993: Two paradigms of baroclinic-wave life-cycle behaviour. *Quarterly Journal of the Royal Meteorological Society*, **119 (509)**, 17–55.

Thorne, C., 2014: Geographies of UK flooding in 2013/4. *The Geographical Journal*, **180 (4)**, 297–309.

Tibaldi, S. and F. Molteni, 1990: On the operational predictability of blocking. *Tellus A*, **42 (3)**, 343–365.

Torn, R. D., 2010a: Diagnosis of the downstream ridging associated with extratropical transition using short-term ensemble forecasts. *Journal of the Atmospheric Sciences*, **67 (3)**, 817–833.

———, 2010b: Ensemble-based sensitivity analysis applied to African easterly waves. *Weather and Forecasting*, **25 (1)**, 61–78.

Torn, R. D. and G. J. Hakim, 2008: Ensemble-based sensitivity analysis. *Monthly Weather Review*, **136 (2)**, 663–677.

Trenberth, K. E., 1986: An assessment of the impact of transient eddies on the zonal flow during a blocking episode using localized Eliassen-Palm flux diagnostics. *Journal of the atmospheric sciences*, **43 (19)**, 2070–2087.

Trenberth, K. E. and J. T. Fasullo, 2012: Climate extremes and climate change: The Russian heat wave and other climate extremes of 2010. *Journal of Geophysical Research: Atmospheres*, **117 (D17)**.

Tyrlis, E. and B. Hoskins, 2015: Aspects of a northern hemisphere atmospheric blocking climatology. *Journal of the atmospheric sciences*, **72 (9)**.

Vitart, F., C. Ardilouze, A. Bonet, A. Brookshaw, M. Chen, C. Codorean, M. Déqué, L. Ferranti, E. Fucile, M. Fuentes, et al., 2016: The sub-seasonal to seasonal prediction (S2S) project database. *Bulletin of the American Meteorological Society*, **(2016)**.

Vitart, F., G. Balsamo, R. Buizza, L. Ferranti, S. Keeley, L. Magnusson, F. Molteni, and A. Weisheimer, 2014: Sub-seasonal predictions. *ECMWF Research Department Technical Memorandum*, **(734)**, 47.

Warner, T., 2010: *Numerical Weather and Climate Prediction*. Cambridge University Press, URL `https://books.google.de/books?id=6RQ3dnjE8lgC`.

Webster, P., V. E. Toma, and H.-M. Kim, 2011: Were the 2010 Pakistan floods predictable? *Geophysical research letters*, **38 (4)**.

Weijenborg, C., H. de Vries, and R. J. Haarsma, 2012: On the direction of Rossby wave breaking in blocking. *Climate dynamics*, **39 (12)**, 2823–2831.

White, W. and N. Clark, 1975: On the development of blocking ridge activity over the central North Pacific. *Journal of the Atmospheric Sciences*, **32 (3)**, 489–502.

Wilks, D., 2011: *Statistical Methods in the Atmospheric Sciences*. Academic Press, Academic Press.

Witte, J., A. Douglass, A. d. Silva, O. Torres, R. Levy, and B. Duncan, 2011: NASA A-Train and Terra observations of the 2010 Russian wildfires. *Atmospheric Chemistry and Physics*, **11 (17)**, 9287–9301.

Woollings, T., B. Hoskins, M. Blackburn, and P. Berrisford, 2008: A new Rossby wave–breaking interpretation of the North Atlantic Oscillation. *Journal of the Atmospheric Sciences*, **65 (2)**, 609–626.

Yamazaki, A. and H. Itoh, 2013: Vortex–vortex interactions for the maintenance of blocking. Part I: The selective absorption mechanism and a case study. *Journal of the Atmospheric Sciences*, **70 (3)**, 725–742.

Zheng, M., E. K. Chang, and B. A. Colle, 2013: Ensemble sensitivity tools for assessing extratropical cyclone intensity and track predictability. *Weather and Forecasting*, **28 (5)**, 1133–1156.

Zhu, Y., 2005: Ensemble forecast: A new approach to uncertainty and predictability. *Advances in atmospheric sciences*, **22 (6)**, 781–788.

Zwolsman, J. and A. Van Bokhoven, 2007: Impact of summer droughts on water quality of the Rhine River - a preview of climate change? *Water Science and Technology*, **56 (4)**, 45–55.

D. Acknowledgment

Zunächst geht mein Dank an meine Betreuerin Prof. Sarah Jones. Ich konnte viel von dir lernen und du hast mich stets in meiner Entwicklung als Wissenschaftlerin gefördert. Besprechungen mit dir haben mich immer weiter gebracht, denn ich wusste, dass ich deinem Urteilsvermögen vertrauen konnte. Wenn du mit etwas einverstanden warst, konnte ich mir sicher sein, dass es gut war. Wegen deiner fachlichen Kompetenz und deiner Aufrichtigkeit habe ich es immer als Privileg gesehen, dich als Betreuerin zu haben!

Prof. Olivia Martius möchte ich für die Betreuung und die Übernahme des Korreferats danken. Liebe Olivia, durch deine herzliche Art und dein unglaubliches Fachwissen warst du mir eine super Betreuerin. Insbesondere möchte ich mich noch für den einmonatigen Forschungsaufenthalt bei dir am Geographischen Institut der Universität Bern bedanken. Hier sei auch den Mitgliedern deiner Arbeitsgruppe "Climate Impact" gedankt. Ich danke euch für die guten Gespräche und dafür, dass ihr mir beigebracht habt, was ein *Apero* ist. Es war toll bei euch! Aber wenn ich mich in ein Tier verwandeln müsste, wäre es sicher kein "Lobster".

Es lässt sich schwer in Worte fassen, welchen Dank Dr. Julia Keller von mir verdient. Julia, du begleitest mich nun schon so lange. Schlussendlich war es dein Vortrag im Hauptseminar zur Theoretischen Meteorologie, der mich von der Relevanz meiner Masterarbeit und meiner Doktorarbeit überzeugt hat. Wie sehr hast du mir all die Jahre geholfen. Fragen zu meteorologischen Zusammenhängen, Fragen zum wissenschaftlichen Schreiben, Fragen zu Programmen, Daten und und und. Mit dir konnte ich immer alles besprechen. Es ist wirklich beneidenswert, wie verständlich du dich ausdrücken kannst. Egal wie sehr mich manche Dinge verwirrt haben, ein Gespräch mit dir hat ausgereicht, um den Nebel zu lichten. "Faszinierend".

Ich danke auch meiner Arbeitsgruppe. Wir hatten teilweise nur noch kurzzeitig das Vergnügen, aber dennoch war es schön für mich, euch kennen zu lernen. Hilke, wir beide haben es zusammen bis ans Ende geschafft! Mit deinem freundlichen Wesen hast du immer gute Laune verbreitet! Dank je wel! Ich danke auch den anderen Mitarbeitern des Instituts. Ihr habt tatsächlich drei Jahre mit mir auf einem Stockwerk überstanden. Ich danke euch, dass ihr meinen provokanten Aussagen und Neckereien stets mit Humor begegnet seid. Insbesondere möchte ich auch meinen Bürokollegen herzlich danken. Ich habe immer gerne mit euch über fachliche Themen diskutiert. Aber genauso gerne auch über alles andere. Wenn

ich am “späten” Morgen ins Büro kam, hatte ich das Gefühl, dass ich nicht einfach zur Arbeit komme, sondern mich auch mit meinen Freunden treffe. Ich saß wirklich mit euch allen sehr gerne in einem Zimmer und ich hoffe, dass es ohne mich nicht zu ruhig wird!

I am also very grateful to Prof. Peter Knippertz and his working group, as I had the possibility to join their group meetings.

A special thank goes to my colleagues which had the courage to do functional training with me during a lot of lunch breaks in summer 2016. It was so much fun and I hope that all of you will go on with training. Never forget Sally!

Many thanks go also to the members of ECMWF. In April 2015, I was invited to come to Reading, where I had the possibility to present and discuss results of my thesis.

Ich danke auch den Trainern der Kampfsportschule Mach 1. Das abendliche Training war für mich der ideale Ausgleich zur Arbeit. So konnte ich stets am nächsten Morgen mit einem klaren Kopf zur Arbeit gehen, wenn auch manchmal mit einem fiesen Muskelkater.

Meine Eltern, Petra und Siegfried Quandt, und meine Schwestern, Jasmin und Sara Quandt, haben mir stets das Gefühl gegeben, mit meinen Problemen nicht allein zu sein. Ich danke euch, dass ihr immer ein offenes Ohr für mich habt und hoffe, dass ich euch stolz mache. Jeder von euch ist auf seine eigene Art und Weise ein Vorbild für mich.

Zuletzt danke ich meinem Freund Valentin Kautz. Nicht nur für deine fachliche Hilfe bei Programmierfragen danke ich dir, sondern auch dafür, dass du immer die richtigen Worte fandest, um mich aufzubauen, wenn ich mal den Glauben an mich selbst verlor. Danke, dass du immer für mich da bist!
4F 69 6E 6B 20 4F 69 6E 6B 20 3A 2A